Durham E-Theses

Mars - the analysis of the mars data and the absolute rate of energy loss of muons in iron

Wells, S. C.

How to cite:

Wells, S. C. (1972) *Mars - the analysis of the mars data and the absolute rate of energy loss of muons in iron*, Durham theses, Durham University. Available at Durham E-Theses Online: http://etheses.dur.ac.uk/8668/

Use policy

The full-text may be used and/or reproduced, and given to third parties in any format or medium, without prior permission or charge, for personal research or study, educational, or not-for-profit purposes provided that:

- a full bibliographic reference is made to the original source
- a link is made to the metadata record in Durham E-Theses
- the full-text is not changed in any way

The full-text must not be sold in any format or medium without the formal permission of the copyright holders.

Please consult the full Durham E-Theses policy for further details.

MARS - The Analysis of the MARS Data and the

Absolute Rate of Energy Loss of Muons in Iron

by

S.C. Wells, B.Sc.

A Thesis submitted to the

University of Durham for the

Degree of Doctor of Philosophy

October, 1972.

ABSTRACT

The method by which the data from the new Durham cosmic ray muon spectrograph, MARS, are analysed by the on-line computer is described in detail. Particular reference is made to a new computer technique which has been developed for the analysis of flash-tube data and an attempt has been made to reconcile experiment and theory. It is concluded that the technique correctly interprets the flash-tube data, especially with regard to extraneously discharged and inefficient tubes, and that its accuracy is sufficient to enable the cosmic ray muon momentum spectrum to be determined by MARS to beyond 5000 GeV/c.

Details of a preliminary measurement of the vertical muon momentum spectrum and charge ratio for the momentum range of 10 - 500 GeV/c are given. Satisfactory agreement is found between these results and those of previous workers.

An experiment is described by which a direct measurement of the absolute rate of energy loss of muons in iron for the momentum range 5 - 40 GeV/c has been made. Agreement is found with the predictions of Sternheimer and Peierls for ionisation loss (together with values for other losses) to within the experimental uncertainties. As such, this experiment is a measurement of the rate of energy loss in a momentum range not previously studied by a direct technique.

PREFACE

The work presented in this thesis was undertaken during the period 1968-71 whilst the author was a research student under the supervision of Dr. M.G. Thompson in the MARS Cosmic Ray Research Group in the Physics Department of Durham University. The author was employed as a Research Assistant in the same department during the following year.

The spectrograph was designed and constructed by the members of the MARS Group; the author having special responsibility for the core store and its circuitry and the on-line computing system. The computer technique by which the flash-tube data are analysed was the conception of the author, as was the method by which the data from the spectrograph as a whole are analysed. The data used for the measurement of the muon momentum spectrum and charge ratio and that for the measurement of the absolute rate of energy loss of muons in iron were obtained with the help of the author's colleagues, but the processing of the data and the interpretation of the results were the responsibility of the author alone.

The data analysis technique has been reported by Thompson and Wells (1972). The preliminary measurement of the muon spectrum and charge ratio and the absolute rate of energy loss of muons in iron have been reported by Ayre et al. (1971a) and (1971b) respectively.

PLATE I

MARS – The Muon Automated
Research Spectrograph
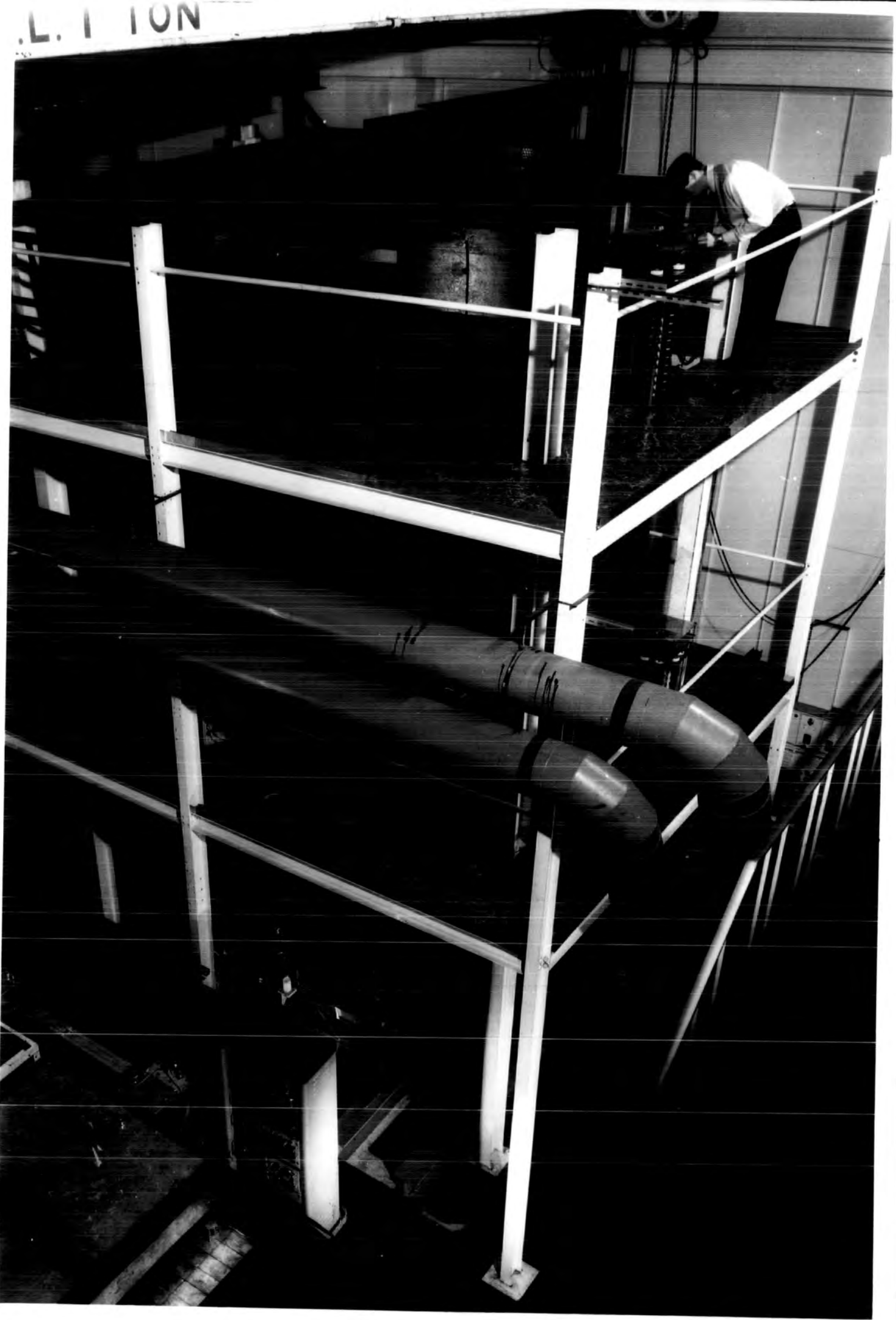
CONTENTS

CHAPTER 1

Introduction

1.1 The Significance of Cosmic Ray Studies

The study of cosmic rays has now been a well founded science for over 50 years. The interest of cosmic rays to the physicist lies in their astrophysical significance and in the nuclear physics of their interactions with the earth's atmosphere. The wide range of their energy spectrum, from an arbitary value of about 1 MeV up to energies of about 1 joule, and the total energy carried by them, which is almost equal to that of starlight, have posed many problems for the theoretical astronomer. In particular, mechanisms by which cosmic rays are generated and accelerated have had to be found and astronomical objects such as supernovae and quasars are currently cited as possible candidates for these processes.

For many years, cosmic rays have provided the nuclear physicist with a beam of very energetic particles and the properties of the primary and the secondary particles, the latter originating in interactions of the primaries in the atmosphere, have long been the subject of intensive study. With the advent of particle accelerators, controlled experiments with high particle densities have become possible and the considerable knowledge gained from cosmic rays studies has been greatly extended. However, even the latest generation of accelerating machines will only enable nuclear interactions to be studied up to laboratory energies of 3×10^{11} eV and cosmic rays are expected to remain an important field of study for some years to come.

1.2 The Primary Radiation

The primary radiation arriving at the earth appears to be isotropic at energies above about 20 GeV. Below this energy, the magnetic field of the earth imposes an asymmetry in the arrival directions of these predominantly positively

charged radiations. An integral primary spectrum has been deduced from the

results of many workers by Greisen (1965) and it is summarised in table 1.1.

Table 1.1

The Integral Primary Cosmic Ray Energy Spectrum

(After Greisen 1965)

Energy Range (eV)	Intensity $(m^{-2}.sec^{-1}. sterad^{-1})$
$10^{10} - \sim 3 \times 10^{15}$	$10^{-4} (10^{14}/E)^{1.6}$
$\sim 3 \times 10^{15} - 10^{18}$	$2 \times 10^{-10}(10^{17}/E)^{2.2}$
$\geq 10^{18}$	$4 \times 10^{-16} (10^{20}/E)^{1.6}$

Two features of this spectrum are immediately obvious and they are the

increase in spectral slope at $\sim 3 \times 10^{15}$ eV, from -1.6 to -2.2, followed by a

reduction in slope back to -1.6 at $\sim 10^{18}$ eV. The increase in slope is generally

accepted to be due to the increasing inability of the galactic magnetic field to

contain primaries with energies above $\sim 3 \times 10^{15}$ eV and the region between

$\sim 3 \times 10^{15}$ and 10^{18} eV represents a gradual loss of the lighter elements by

the galaxy as their individual magnetic rigidities are exceeded (Linsley, 1962).

The reduction in spectral slope at above 10^{18} eV was initially attributed to

extra-galactic sources of radiation but more recently, a re-analysis of the data

in this region, which comes exclusively from air shower measurements, has raised

doubts as to the existence of this 'kink' in the spectrum. (See the review by

Wolfendale, 1972).

The discovery of the $2.7^{o}K$ isotropic black-body radiation in the Universe

(e.g. Roll and Wilkinson, 1967) has increased the interest in the primary

radiation at energies in excess of 10^{18} eV. If these primaries are of extra

galactic origin, then the spectrum (which is expected to be entirely composed of

protons at these energies because of fragmentation) is expected to terminate

abruptly at $\sim 10^{20}$ eV because of the onset of photomeson interactions $(p + \gamma \rightarrow p + \pi\text{'S})$ between the protons and the microwave background (Greisen, 1966). At present, confirmation or otherwise of such a discontinuity in the spectrum has to await the availability of more data.

Table 1.2

The Mass Composition of Primary Cosmic Rays at 10^{10} eV

(After Wolfendale, 1972)

Nucleus	Intensity $(m^{-2}.sec^{-1}.sterad^{-1} \; (MeV/nucleon)^{-1})$	Abundance by Number
P	8.0×10^{-1}	88.2%
He^4	1.0×10^{-1}	11.0%
Li,Be,B	1×10^{-3}	0.1%
C,N,O	5×10^{-3}	0.6%
Z > 16	$\sim 6 \times 10^{-4}$	$\sim 0.1\%$

The composition of the primary radiation has been measured with fair accuracy in the region of 10^{10}eV by satellite techniques and it is summarised in table 1.2 (Wolfendale, 1972). A comparison between this composition and that of the Universe shows that there is a considerable excess of Li, Be and B nuclei in the primary radiation. This can be explained if these elements are the result of the fragmentation of heavier nuclei in penetrating the ~ 3gm.cm^{-2} of matter on their way to earth. This would infer that possible sources of cosmic rays are supernovae where heavier elements are in abundance.

The composition of the primary radiation up to energies of 10^{15} ev is believed to be similar to that at 10^{10} eV, but above 10^{15} eV the situation is not clear except that there is expected to be an increase in the proportion of protons because of the fragmentation of the heavier nuclei (Wolfendale, 1972).

1.3 The Propagation of Cosmic Rays through the Atmosphere

The primary cosmic radiation which enters the earth's atmosphere suffers multiple nuclear interactions with air nuclei and the resulting cascade of particles is known as an extensive air shower. As was described in the previous section, the primary radiation is mainly composed of protons, the interaction length for protons being approximately 80 gm.cm^{-2} at high energies. The thickness of the earth's atmosphere is 1030 gm.cm^{-2} and consequently the majority of the protons interact at a mean height of 18km above the surface of the earth. The inelasticity of these interactions is about 0.5 and hence the protons lose about half of their energy in each interaction. The majority of the energy which is lost manifests itself as pions, but a small proportion (which probably increases with primary energy) appears in the form of kaons and hyperons. The total number of secondaries, N_s, is dependent upon the primary energy, E_p, and to a good approximation the empirical relationship is $N_s = 2.1 \ E_p^{\frac{1}{4}}$ (Wolfendale, 1972).

The three charge states of the pion are produced in almost equal quantities and it is the difference between the decay modes of the charged and uncharged pions which produces some of the characteristics of an air shower. The π^0 component, with a mean life time of 10^{-16} secs, decays into two γ rays and these initiate an electron-photon cascade by way of pair production and bremsstrahlung. There is also a small proportion of photomeson production and pair production of muons. The growth of these cascades is approximately exponential (Heitler, 1948) until a point is reached when the average electron energy falls below the critical energy for air (84 MeV). When this occurs, absorption of the electrons by the atmosphere begins to dominate and the shower size decreases. Those

cascades which originate from a primary proton with an energy greater than 5×10^{13}eV are not completely absorbed by the atmosphere and can be observed at sea level by arrays of particle detectors.

Charged pions have a mean life time of 2.6×10^{-8} secs and the mean interaction length for them is 120gm. cm^{-2}. These pions either undergo further nuclear interactions or they decay into muons and neutrinos. The inelasticity for the former process is 1.0 but more pions are produced as a result of these interactions. Again there will be a proportion of neutral pions produced and consequently some of the energy of the initially charged pions is gradually lost to the electron-photon cascade. The mean life time of muons is 2.2×10^{-6} secs and because they are weakly interacting, muons with energies above a few GeV will easily reach the surface of the earth before decaying.

The probability of a charged pion either interacting or decaying depends upon the density of the atmosphere and the relativistic life time of the pion. In the vertical direction where there is a rapid increase in the density of the atmosphere, interactions are more probable, but at larger zenith angles, the pion spends comparitively more of its time in a rarefied atmosphere and decay into high energy muons becomes more important. As a consequence, the intensity of muons above an energy of about 100 GeV increases with the secant of the zenith angle of their trajectories and this is known as the 'sec θ' enhancement.

1.4 Cosmic Ray Muons at Sea Level

1.4.1 Introduction

Cosmic ray muons are the result of meson decays in the upper atmosphere and the comparatively long life time of the muon means that there is a considerable flux of them arriving at sea level. The properties of these muons reflect the characteristics of the nuclear interactions from which their parent mesons came. Consequently, it is possible to infer parameters of nuclear interactions at energies well beyond those attainable by machines although the initial

interaction is not directly observed. Two properties of cosmic ray muons which can be observed are their momentum spectrum and their charge excess (there being more positive than negative muons). From these, it is possible to deduce the nature of the secondary particles of the interactions and also their multiplicity.

The muon momentum spectrum and charge ratio are discussed below together with an interesting result reported by Bergeson et al. (1968) from Utah who did not observe the expected sec θ enhancement, discussed in section 1.3, at energies above 500 GeV.

1.4.2   The Cosmic Ray Muon Momentum Spectrum

The cosmic ray muon momentum spectrum has been measured by many observers and the integral spectrum of Osborne et al. (1964) is shown in figure 1.1. This spectrum was derived from sea level and underground measurements of the muon intensity and it was normalised to the integral intensity above 1 GeV as given by Rossi (1948). More recently, Allkofer et al. (1971) have reported the results of three experiments to measure the cosmic ray muon momentum spectrum and they are at variance with the absolute intensity of Rossi and with the spectra of other workers. Figure 1.2 shows the relative difference between the spectra of other workers and that of Allkofer et al. It is evident that there is considerable disagreement not only between the absolute intensities but also in spectral shape.

It is concluded by Allkofer et al. that the intensities of absolute spectra were underestimated by 20% by many investigators. Evidence of a higher intensity than that given by Rossi have been provided by Ayre (1971) whose absolute intensity measurements are in closer agreement with those of Allkofer. However, there are still discrepancies as to the precise shape of the spectrum.

1.4.3.   The Charge Ratio of Cosmic Ray Muons

There is an excess of positively charged muons in the muon flux at sea level and figure 1.3 is a survey of the muon charge ratio as measured by several workers.
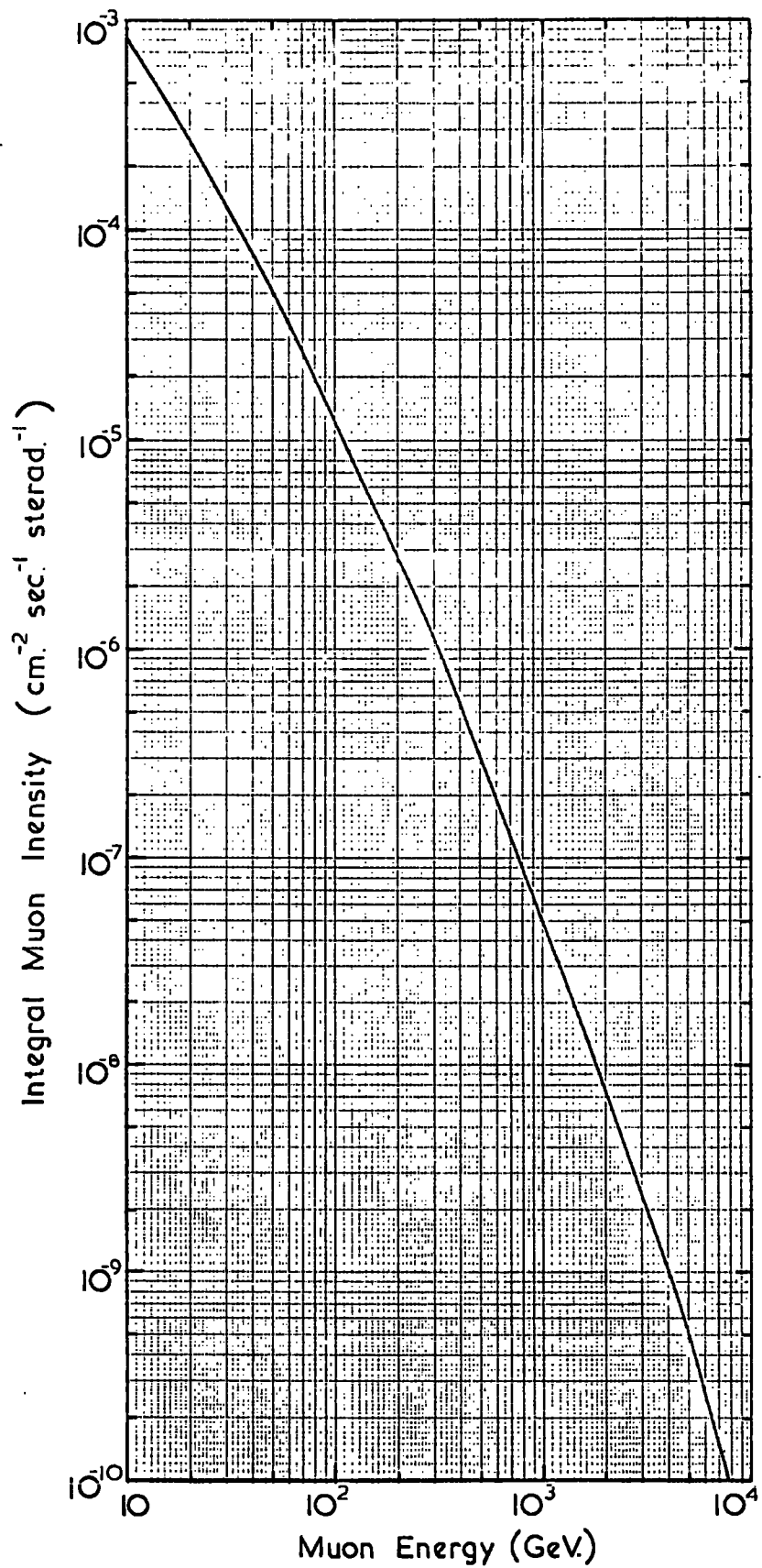
Figure 1.1   The Vertical Muon Energy Spectrum of
Osborne et al. (1964)

(%)

Relative Difference from
Differential Intensity of Allkofer

+40

+20

0

-20

-40

— — HW (1962)
—·—·— OWP (1964)
—··—··— Menon (1967)
△ Cottrell (1970)
○ Wolfendale (1971)

+40

Relative Difference
from Integral Intensity
of Allkofer

+20

Error
band

0

-20

-40

10^{-1} 10^0 10^1 10^2 10^3

Momentum (GeV/c)
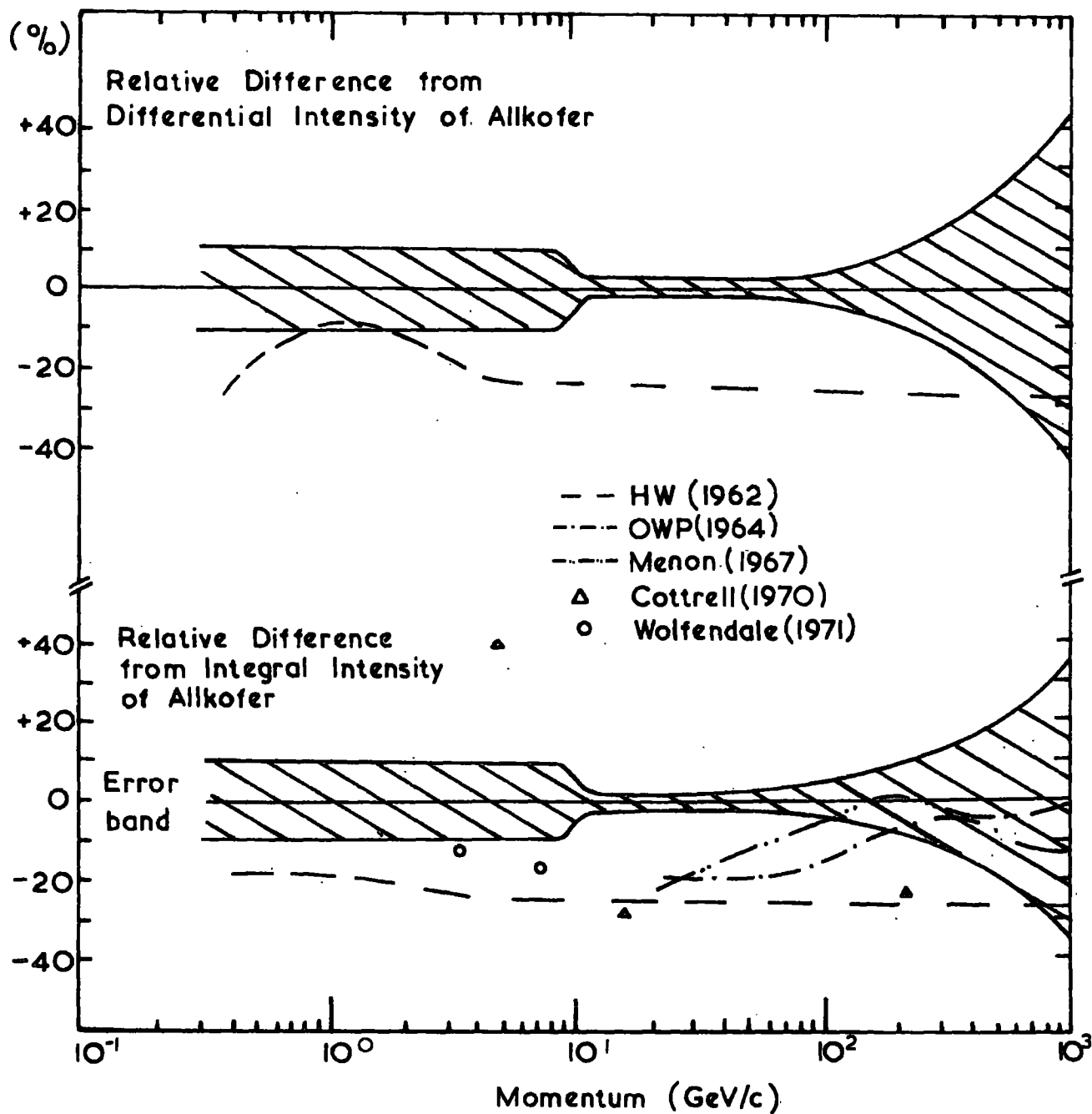
Figure I.2   A Comparison of Cosmic Ray Muon Spectra
(after Allkofer et al. 1971)

Figure 1.3 A Survey of Charge Ratio Measurements in the

Vertical Direction.

Key

⊖   Caro et al. (1950)

◈   Owen and Wilson (1951)

X   Filosofo et al. (1951)

☐   Pine et al. (1959)

△   Holmes et al. (1961)

○   Hayman and Wolfendale (1962)

▽   Aurela et al. (1966)

◇   Allkofer et al. (1969)

⦶   Allkofer et al. (1971)

◩   Appleton et al. (1971)

▽   Nandi and Sinha (1972)

Muon Momentum (GeV/c)

Charge Ratio (N_μ^+/N_μ^-)
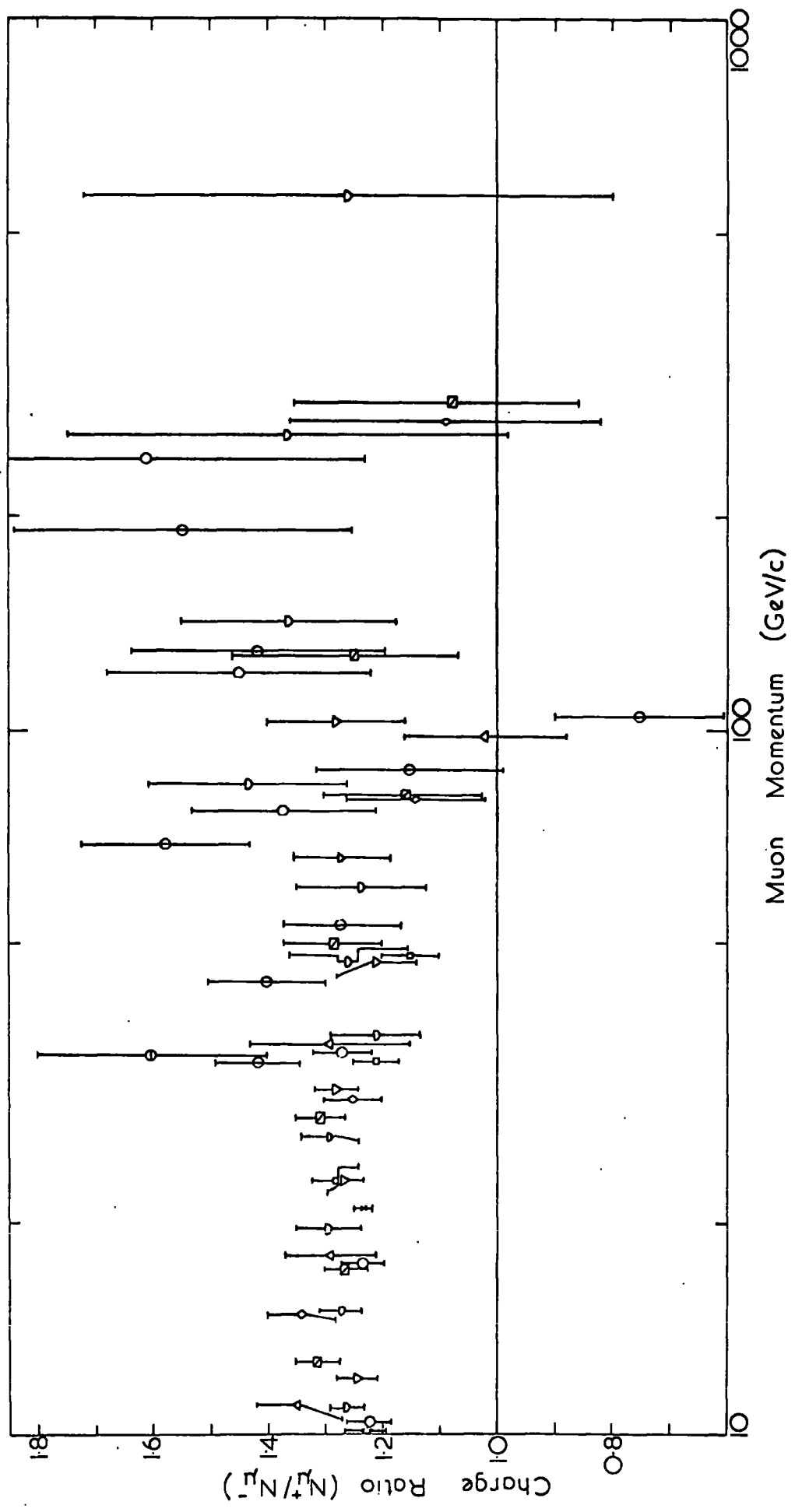
One explanation for this phenomenum is that the primary radiation is predominently positive in charge. However, the effects of this should only be evident at high energies where the parents of the muons originated in the initial interaction. At lower energies, the parents are produced in secondary interactions and the effect of the charge of the primary radiation is diluted. The explanation of the charge ratio of low energy muons is that a proportion of the parents of the muons are kaons rather than pions. The energy threshold for negative kaon production is much higher than that for positive kaons for stangeness conservation reasons and the ratio of the number of positive to negative kaons is about 4. A contribution of about 20% kaons to the parents of the muons is able to explain the charge ratio of muons at low energies.

It is evident from figure 1.3 that there is again considerable disagreement between the values for the charge ratio as a function of momentum given by different workers, but measurements at high energies are severely hampered by poor statistics. Any fine structure in the charge ratio would reflect a change in the nuclear processes which create the parent mesons and evidence to this effect is continually being sought. For example, Allkofer et al. (1971a) reported a minimum in the charge ratio in the region of 100 GeV in the vertical direction, but as can be seen from figure 1.3, this has not been substantiated by other workers.

1.4.4 The Utah Effect

The propagation of muons through the atmosphere has been described in section 1.3 and the explanation of the enhancement of the intensity of muons with the secant of the zenith angle of their tracks was given. This explanation is valid under the condition that the muons are the progeny of pions and kaons, because it is the increase in the probability of them decaying (as opposed to interacting) at large zenith angles which produces this enhancement. Bergeson et al. (1968) measured the intensity of muons with zenith angle with apparatus

designed to study neutrino interactions. The apparatus is situated in the base of a mountain in Utah at a depth of 1850 feet. The expected sec θ enhancement was not observed in their results at energies above 500 GeV and this lead them to postulate the direct production of mesons or the X - process.

These workers found that their results could be explained if muons with energies above 500 GeV were not produced as the result of pion or kaon decays but rather that they were produced directly and isotropically by some process. It has been suggested that the intermediate vector boson could be responsible for this effect and many muon production models have been investigated (e.g. Carlson et al., 1971). One of the consequences of the theory of direct production is that the vertical muon spectrum should be somewhat flatter and higher at energies above 500 GeV than had been previously observed. The discrepancy between the experimental results was resolved when further studies by the Utah group lead to the discovery of experimental biases (notably with respect to the rock densities) and as a consequence, the divergence from the sec θ enhancement was not evident at energies less than 1000 GeV.

The lack of data in this energy region makes a comparison with other workers impossible but further evidence for the Utah effect has been provided by the same group after the observance of 2×10^5 muons through their detector (Bergeson et al., 1971). However, more recently, Cassidy (1972, private communication) has reported that data from a new measurement of the muon intensity underground with the same apparatus (the analysis of which is as yet incomplete) appear to behave in a manner not inconsistent with the sec θ enhancement and that evidence for the Utah effect is not so pronounced.

An experiment performed in the Kolar-Gold Mines in India by Krishnaswamy et al. (1969) studied the angular distribution of atmospheric muons at various depths underground. These workers failed to observe the Utah effect and their results are consistent with the model that muons with energies up to several thousand GeV are produced wholly through the decays of pions and kaons. If

the Utah effect is found to be true, then it is of fundamental importance to elementary particle physics but confirmation or otherwise of the effect will have to await the availability of data from other experiments.

1.5 Conclusions and the Present Work

It is evident from the discussion presented in this chapter that the position regarding a precise knowledge of the cosmic ray muon spectrum and charge ratio at energies above ~ 100 GeV is most unsatisfactory and a new measurement is required. The results presented by the Utah group have only increased the urgency for such a measurement. It is important that such a measurement should be made at sea level rather than underground so that uncertainties in rock densities and the rate of energy loss are not present. It is for these reasons that the new spectrograph MARS (Muon Automated Research Spectrograph) has been designed and built at sea level in Durham.

MARS will enable a precise determination of the muon momentum spectrum and charge ratio to be made to momenta beyond 5000 GeV/c. It is first intended to operate the spectrograph in the vertical direction and then at some future time to reconstruct the spectrograph in the near horizontal. In the latter position it will be possible to use the spectrograph as a source of high energy muons and to study the interactions of these muons in apparatus placed in the particle beam of the spectrograph.

The characteristics of MARS are described in Chapter 2 of this thesis and Chapters 3 and 4 are devoted to a description of the analysis technique used by the on-line computer to analyse the data. Particular reference is made to a new computer technique to locate the tracks of muons in flash-tube trays. A detailed investigation of the properties of this technique and of the data analysis programme as a whole is given in Chapter 5 and an attempt is made to reconcile experimental results with theoretical predictions. A preliminary measurement of the differential muon momentum spectrum and charge ratio made

with MARS for the momentum range of 10 - 1000 GeV/c is described in Chapter 6 and Chapter 7 reports an experiment to measure the absolute rate of energy loss of muons in the iron of MARS. The momentum range of the latter experiment is 5 - 40 GeV/c and as such is the only direct measurement of the energy loss to have been made in this range.

CHAPTER 2

MARS - The Instrument

2.1 Introduction

Before it is possible to design an instrument to measure the sea level cosmic ray muon spectrum to beyond a momentum of 5000 GeV/c, due consideration must be given to several aspects of the properties of muons, the properties of their spectrum and the requirements of the experiment, namely

1) The instrument must be sufficiently sensitive to resolve the muons with the highest momentum.

2) The rate of muons at the highest momenta must be sufficiently large so as to make the number recorded over a reasonable period of time (1 - 2 years) statistically significant.

3) The interference of electron cascades (generated by interactions of muons in the detecting apparatus) on the resolution of the trajectories of the muons must be minimised.

4) The steepness of the muon spectrum implies that the muons with the highest energies must be extracted from the very much larger flux of low energy muons.

The choice of instrument available to the experimentalist is many and varied but, over the past few years, one particular type of instrument has dominated muon spectrum studies and this being the magnetic spectrograph. The measurement of momentum with this instrument is absolute, as opposed to those techniques, such as energy loss and ionisation where normalisation is required to relate the momentum to some measured quantity. In addition, the magnetic spectrograph is the only instrument with which the required momentum resolution can be obtained. It is for these reasons that a magnetic spectrograph was adopted for the MARS project and the design considerations will now be discussed.

2.2 Design considerations

The principle of operation of a magnetic spectrograph is that the deflection suffered by a charged particle in a magnetic field is observed and this deflection is then related to the momentum of the particle. As a consequence, the design of such an instrument can be divided into several distinct parts and each is discussed in detail below.

2.2.1 The Design of the Magnet

When a particle of mass m and charge e traverses a magnetic field of flux density B at a velocity v, then it experiences the Lorentz force, F, whose magnitude and direction is given by

$$\underline{F} = e \, \underline{v} \times \underline{B}$$

This force is always perpendicular to the velocity of the particle and hence the trajectory of the particle describes an arc of a circle. If the radius of curvature is r, then the equation of motion is $F = mv^2/r = Bev$. Expressing r in terms of the momentum of the particle, p, we have

$$r = p/Be \tag{2.1}$$

If the particle moves a distance dl along the arc of the circle, then the angular deflection, $d\theta$, suffered by the particle is $d\theta = dl/r$, and the total angular deflection, θ, is

$$\theta = \frac{e}{p} \int B.dl \tag{2.2}$$

Expressing p in GeV/c, B in kilogauss and l in metres we have

$$\theta = \frac{0.03}{p} \text{ radians } . \text{ m}^{-1} . \text{ kgauss}^{-1} \tag{2.3}$$

The maximum magnetic path length available to MARS in the vertical direction is about 5m and, assuming it is possible to determine θ to within 5×10^{-4} radians, it is necessary to have a magnetic flux density of about 15 kilogauss in order to resolve a momentum of 5000 GeV/c. The only method for maintaining steady, uniform magnetic fields of this magnitude over a distance of 5m is to use solid iron magnets, where the field is totally enclosed and where the magnetic

deflection occurs in the iron itself. This is the type of magnet adopted for the MARS project.

2.2.2 Interactions of the Muons in the Magnet

Unfortunately, solid iron magnets have two disadvantages. Firstly, the muons lose energy in the iron by electromagnetic interactions (amounting to about 1.4 GeV/m of iron) and secondly, the muons undergo Coulomb scattering in the iron.

The total energy lost by muons through MARS is about 7.5 GeV and consequently, this is only of importance at energies below 50 GeV when the loss is a considerable proportion of the total energy of the muon. At higher momenta, the accompaniment of the muons by electron-photon cascades from electromagnetic interactions is of greater importance. When such a cascade accompanies the muon through one of the particle locating levels of the spectrograph, then the information from this level may be rendered useless as far as accurate trajectory location is concerned. These cascades are the result of interaction processes, namely, pair production, bremsstrahlung and nuclear interactions, and the cross-sections for these processes increase rapidly with muon energy. The probability of a cascade accompanying a muon out of a magnet block has been given by Said (1966) and his results are shown in figure 2.1. It is evident that a crucial design consideration of a spectrograph for the study of high energy muons is that the interference of these cascades with the location of the trajectory of the muon must be minimised. This has been achieved in MARS by dividing the magnet into four blocks and interspersing and surrounding them with layers of particle detectors. Consequently, a maximum of two cascades at different locating levels in the spectrograph can be tolerated.

An examination of the Coulomb scattering process by Rossi and Greisen (1941) shows that the relation between the r.m.s. angle of scatter, $<\theta_s>$, for a muon with momentum $p(\text{GeV}/c)$ and the thickness, l, of the medium traversed, is

$$<\theta_s> = \frac{21}{p\beta} \sqrt{\left(\frac{l}{X_0}\right)} \qquad (2.4)$$
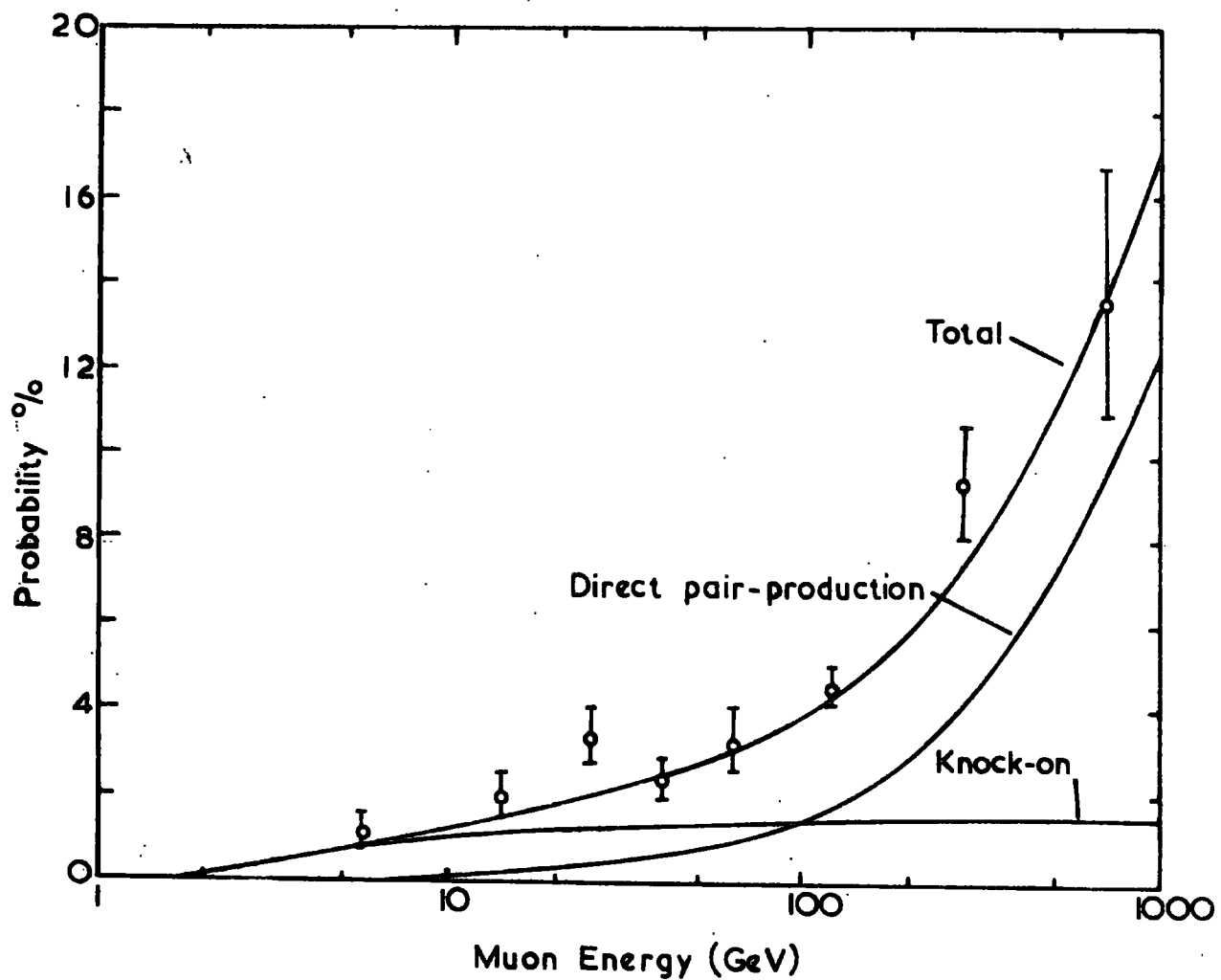
Figure 2.1   Probability of an Electron Cascade Accompanying
a Muon out of a Magnet Block. (After Said, 1966)

where X_o is the radiation length of the medium. From equation 2.2, the magnetic

angular deflection can be written as θ_m = Bel/p, and hence the ratio of the

r.m.s. angle of scatter to the magnetic angular deflection for muons with $\beta = 1$.

is

$$\frac{<\theta_s>}{\theta_m} = \frac{21}{Be\sqrt{X_o}} \frac{1}{\sqrt{l}} \cdot \qquad (2.5)$$

It can be seen that this ratio is independent of the momentum of the muon and,

for a particular magnet material, it is only dependent upon the length of the

magnet.

The consequence of scattering is that the measured magnetic deflection is

always uncertain by the amount given by the above ratio. In practice, this means

that a low momentum muon may be assigned a much larger momentum and, in the case

of the muon spectrum where the slope of the spectrum increases with momentum, the

measured spectrum is distorted at high momenta by an excess of particles. If this

distortion is too severe, it will prevent the determination of the true spectrum,

and therefore, it is necessary to make the effects of scattering as small as

possible by minimising equation 2.5.

2.2.3 The Intensity of Cosmic Ray Muons

The vertical, cosmic ray muon, integral spectrum, at sea level has been given

by Osborne, Palmer and Wolfendale (1964) and their results are shown in figure 1.1.

If a precise determination of this spectrum is to be made beyond a momentum of

1000 GeV/c, then the rate of muons with momenta above this value must be large

enough to ensure that a statistically significant quantity of them is collected

during the running time of the experiment. For every muon with a momentum greater

than 1000 GeV/c, there are 3×10^4 muons with momenta greater than 7 GeV/c, all of

which have to be analysed.

Previous experiments have not processed the data automatically. This has

imposed a serious limitation on the quantity of data which could be handled and

therefore reduced the upper momentum limit to which the spectrum could be determined.

With the advent of modern electronic techniques and computers, it is now possible to construct digital systems which automatically and continually analyse the data whilst the experiment is running. Such a system has been designed for the MARS experiment and, because it is capable of handling one muon every two seconds, no problems arising from the large amounts of data are envisaged.

2.2.4 The Location of the Trajectories of the Muons

An essential feature of an automated spectrograph is that the trajectory of the muons be located by detectors which are digitised. The information contained in these detectors can then be used by an automatic system to calculate the momenta of the muons. There are many particle detectors capable of being digitised but for the MARS experiment it was decided to use Conversi or neon flash-tubes (Conversi and Gozzini, 1955).

A flash tube consists of a glass tube filled with neon. After the passage of an ionising particle through a tube, the gas is caused to discharge by the application of a high voltage pulse across the tube. Unfortunately, the trajectory resolution of a single tube is poor, but when tubes are combined together into several layers to form a hodoscope, resolutions of a fraction of a millimetre can be obtained.

A digitisation technique for neon flash tubes has been described by Ayre and Thompson (1969,1970). A metal probe is placed adjacent to the window of a tube and a voltage pulse is developed upon it whenever the tube discharges. This pulse is of sufficient magnitude (a few volts) to be used by integrated logic circuitry for digitisation purposes. It is therefore possible to construct hodoscopes of these digitised tubes and use them to automatically locate the trajectories of the muons.

2.3 MARS - The Physical Characteristics

2.3.1 Description

Plate 1 is a photograph of MARS and figures 2.2 and 2.3 show the physical dimensions and the sitings of the various detectors.
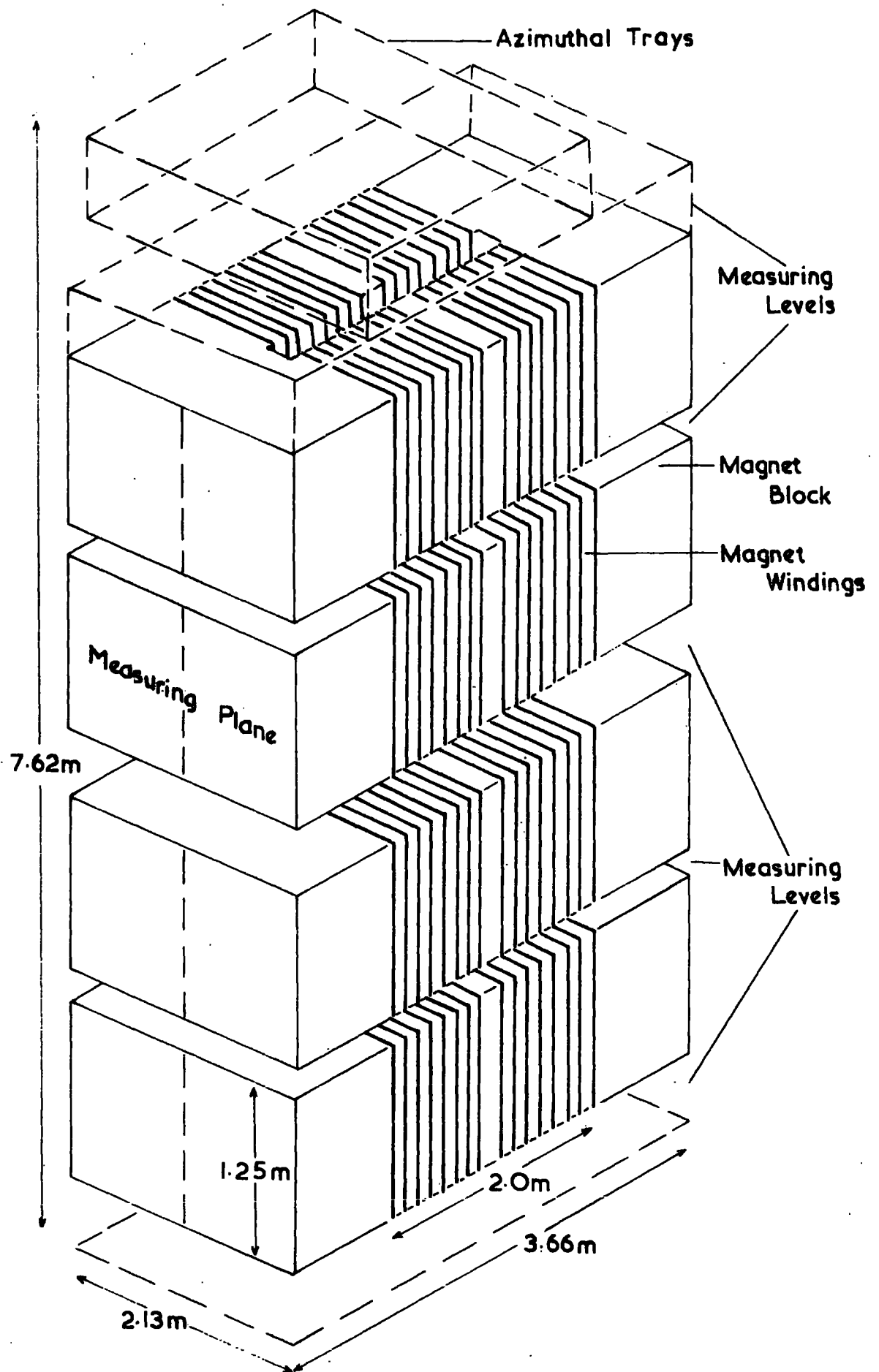
Figure 2.2   The General Features of MARS.

411·00	Level 7	Azimuth Tray
365·15	Level 6	Azimuth Tray
347·74		Momentum Selector Tray
333·08	Level 5	Scintillator
317·65		Measuring Tray
	Magnet · · Block	
173·50	Level 4	Measuring Tray
	Magnet · · Block	
28·29		Momentum Selector Tray
13·81	Level 3	Scintillator
0·0		Measuring Tray
9·37	Magnet · · Block	
142·10	Level 2	Measuring Tray
	Magnet · · Block	
285·88		Momentum Selector Tray
298·86	Level I	Measuring Tray
316·48		Scintillator
(cms)		

Figure 2.3   The Relative Positions of the Various Detectors in MARS.

MARS is basically a multilayer spectropgraph consisting of four toroidal magnet blocks, interspersed and surrounded by particle detectors. This particular configuration was chosen so that the interference of electron cascades, emanating from the magnet blocks and causing ambiguities in trajectory location, would be minimised. In addition, lead absorber may be placed on the top of the spectrograph to absorb the electrons from any air shower accompaniment of the muons. This is particularly important at the highest energies where the muons are likely to be situated near the axis of an air shower, where particle densities are high.

Each magnet block is 3.66m long, 2.13m wide and 1.25m high. There is a slot 2m long down the centre of each block parallel to the longer side, which facilitated the winding of the energising coils onto the blocks to form a toroid, and which divides the spectrograph into two symmetric halves. The magnetic field is in opposite senses along either side of the spectrograph. Each block weighs 71 tons, there being 284 tons of magnet in all, and the overall height is 7.62m of which 5m is iron.

The various detection levels of MARS have been designated a number as shown in figure 2.3. The lowest level is known as level 1 and the highest, level 5. The azimuthal trays are known as levels 6 and 7.

2.3.2 The Magnetic Field

The magnet blocks were specifically designed to be toroids so as to ensure a maximum magnetic flux density. The magnet consumes 10kW of power supplied at 100V and 100A, and the mean internal flux density is 16.3 $\pm$ 0.1 kilogauss. The flux density is uniform to within 2% over the magnetic volumes adjacent to the slot and this is the region of the magnet through which the muons under observation pass.

The total magnetic path length is 5m and hence, equation 2.3 becomes

$$p\theta = 2.445 \text{ (GeV/c). radians.}$$

Converting this equation into a lateral deflection, Δ , as defined in figure

2.5, and making a small correction for the effect of the air gaps between the

magnet blocks, we have, at high momenta,

$$p\Delta = 390 \text{ GeV/c. cm.}$$

2.3.3 Coulomb Scattering

Substituting the radiation length of iron (13.8 gm.cm^{-2}) into equation

2.5 and again making a small correction for the effects of the gaps between

the magnet blocks, the ratio of the r.m.s. angle of scatter to the magnetic

deflection is 12%. Preliminary calculations have shown that this should in

no way prevent the precise determination of the muon spectrum to beyond 5000 GeV/c.

2.4 The Detection and Location of the Muons

2.4.1 The Scintillation Counters

The muon is initially detected by the three scintillation counters on

either side of the magnet. Each counter comprises of a sheet of NE102a

scintillation material of size 1.77m x 0.75m x 0.05m, which is viewed by four

photomultipliers, two at either end of the phosphor. The pulse heights derived

from opposite pairs of photomultipliers are electronically added together and

the resultant pulse, after discrimination and shaping, is taken in coincidence

with the equivalent pulse from the other pair of photomultipliers. In this way

a pulse is generated every time a muon passes through a scintillator. These

pulses, from the three scintillation counters of one side of the spectrograph,

are taken in coincidence together to generate a trigger pulse for the remainder

of the detecting equipment every time a muon passes within the acceptance of

that side of the spectrograph.

2.4.2 The Flash Tube Trays

The trajectories of the muons are located in the plane perpendicular to

the magnetic field by means of digitised neon flash-tubes. Two sizes of tubes

are used. The larger tubes are 2m long and have a mean external diameter of

1.9 cm. They are stacked together in a tube tray, which comprises four layers

of tubes, there being 39 tubes in each layer. The layers are seperated by sheets of aluminium, which form the electrodes. Every time a muon traverses a particular side of the instrument, a high voltage pulse of amplitude 4.5kV and duration $3\mu s$ is applied to the electrodes of these trays of that side. There are three such large tube trays on either side of the magnet and they are positioned at the same detection levels as the scintillators.

The smaller flash-tubes are again 2m long but these have a mean external diameter of only 0.8cm. Eight layers of tubes are used in each of the small-tube trays and there are 89 tubes in each layer. The high voltage pulse applied to the aluminium electrodes, which seperate the layers, is of amplitude 6kV and of duration $1.5\mu s$. There are five such trays situated in each side of the spectrograph. The large-tube trays are termed the momentum trays and the small-tube trays the measuring trays.

The tubes pass through precision drilled brass plates at each end of the trays which locate the tubes at these points to within 0.025mm. The axes of the tubes run parallel to the magnetic field. The tubes are digitised by means of metal probes adjacent to the front windows of the tubes and the pulse developed on a probe, when a tube discharges, passes into electronic circuits which complete the digitisation circuitry.

Across the top of the spectrograph, perpendicular to the magnetic field, are two trays each containing four layers of the large diameter flash-tubes; there are 119 tubes in each layer. These are used to define the angle of the trajectories of the muons parallel to the magnetic field and they are known as the azimuthal trays. These trays are common to both sides of the spectrograph and are operated by a coincidence pulse from either side of the spectrograph.

2.5 General Properties of MARS

2.5.1 The Acceptance

In the absence of a magnetic field and neglecting scattering, the outer most scintillators define the acceptance for muons. When a magnetic field is present, muons with low momentum are deflected out of the magnet and as a result, the acceptance is lower for these particles. The scintillation counters have an area of 177.0cm x 75.0cm and the outer most two are seperated by 649.6cm. Hence, the acceptance of one side of the spectrograph, for muons with infinite momentum, is $(408 \pm 1)cm^2$. sterad. and for such muons the opening angle in the plane perpendicular to the magnetic field is $\pm 6.8^o$ and it is $\pm 15.5^o$ in the parallel plane. The acceptance of one side of the spectrograph has been calculated as a function of momentum for a magnetic field of 16.3 kgauss and with the rate of energy loss for muons in iron determined from the theory of Sternheimer and Peierls (1971), details of which are given in Chapter 7. The results are shown in figure 2.4 where the acceptance for the scintillators alone, and for the scintillators and measuring trays together, are given as a function of momentum.

2.5.2 The Expected rate of muons

The total thickness of absorber through which a muon must pass before it is detected is equivalent to $3970gm.cm^{-2}$ for vertical muons and is correspondingly larger for trajectories inclined to the vertical. Consequently, from the energy loss theory of Sternheimer and Peierls (1971, given in Chapter 7) there is a low momentum cut off at 6.9 GeV/c to the observed spectrum. The contributions of the various elements of the spectrograph to the total absorber thickness are summarized in table 7.2.

With a knowledge of the total absorber thickness and the acceptance of the spectrograph, it is possible to calculate the expected rates of muons above certain momenta from the OPW integral spectrum and these are given in table 2.1.
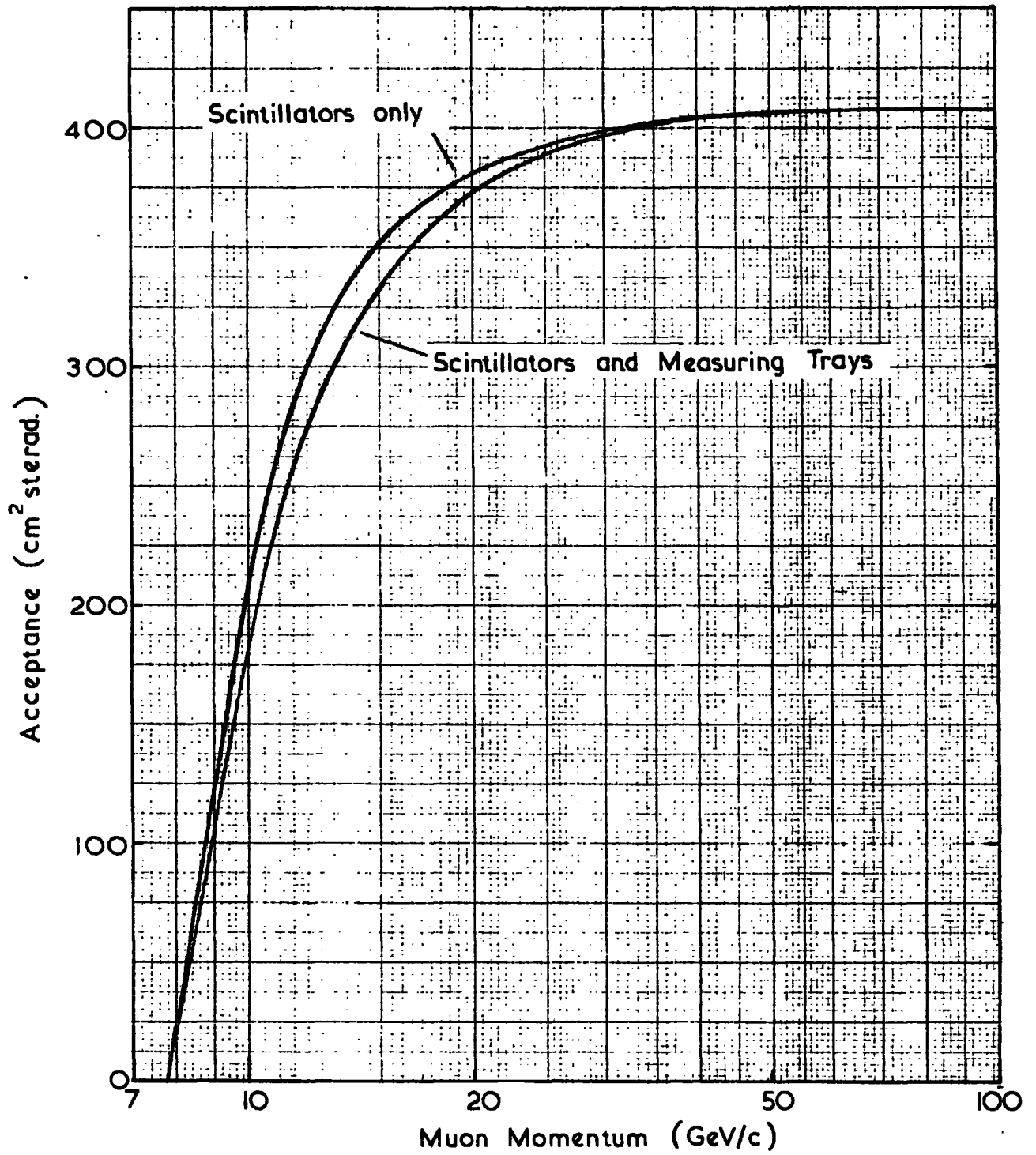
Figure 2.4   The Acceptance Function for One Side of MARS.

The measured rates of muons down each side of the spectrograph, with and without a magnetic field, are 18 ± 1 min^{-1} and 29 ± 1 min^{-1} respectively.

Table 2.1

The Expected Rates of Muons through MARS

Momentum (GeV/c)	Integral Rate
> 6.9	36 min^{-1}
> 50	2.3 min^{-1}
> 100	35 h^{-1}
> 200	7.9 h^{-1}
> 500	20 day^{-1}
> 1000	3.2 day^{-1}
> 2000	3.6 week^{-1}
> 5000	12.3 year^{-1}

2.5.3 The Maximum Detectable Momentum

The maximum detectable momentum will be discussed in detail in Chapter 5, because its value depends upon the method of analysis of the data. It is sufficient to state here that the maximum detectable momentum is 5427 GeV/c and with an expected rate (based upon the OPW spectrum) of about 10 muons per year above this momentum, it will be possible to determine the muon momentum spectrum and charge ratio up to this momentum.

2.6 Principle of Operation

A muon is detected as traversing the spectrograph by a three fold coincidence from the scintillators of one side of the instrument and high voltage pulses are then applied to the flash-tube trays of that side and to the azimuthal trays. The flash-tubes, through which the muon passed, discharge

and the digitisation pulses developed on their probes are recorded in flip-flop memory circuits situated near the ends of the tubes.

The memories of the momentum trays are then analysed by a device known as the momentum selector. This is capable of deciding within 80μs if the lateral magnetic deflection was less than ± 1.0cm. If this was the case, then the information contained in the memories of the measuring trays is passed, via a buffer memory (a ferrite core store), to an on-line IBM 1130 computer, where the information is stored for a further, more detailed, analysis.

For every event, a device known as RUDI (Restricted Use Digital Instrument) automatically calculates the magnetic deflection of the muon from the information contained in the momentum trays. This deflection is used to generate an address for one of the memories of a PHA (Pulse Height Analyser), the contents of which are incremented by one, and consequently the deflection spectrum is continuously recorded. Details of the individual devices are given below.

Thus, MARS is able to measure and record continually the deflection spectrum for all muons detected by the instrument and it is able to extract those events, which are of interest because of their high momentum, from the large flux of low momentum events. These latter events are made available for a more thorough and detailed analysis by computer.

2.7 The Individual Elements of MARS

2.7.1 The Momentum Trays

The momentum trays are sited at the top, middle and bottom of the spectrograph, as shown in figure 2.3. The electronics attached to each tray examine the configuration of the discharged tubes produced by the muon and assign the trajectory to one of the 152 x 5mm cells which form the digitised output for a tray. The trajectory is thus located at three points along its path and, from this information, it is possible to calculate the deflection of the muon in the magnetic field.

2.7.2 The Momentum Selector

The momentum selector contains three shift registers termed registers A, B and C and they correspond to momentum trays 5, 3 and 1 respectively. Each register contains 152 elements which are in a one to one correspondence with the cells of the momentum trays. The contents of the trays are strobed into the shift registers and the elements corresponding to the activated cells are set to a logical 1. Figure 2.6 is a schematic diagram of the momentum selector with one element of each register set to a logical 1.

A series of clock pulses are applied to the shift registers and, when the activated element of tray B reaches either element 76 or 152, the positions of the cells in A and C are examined to see if they form a 'straight line' with B. (Registers A and C are extended by 76 cells to allow for none vertical muons). A 'straight line' is defined as any trajectory with a deflection of less than two cells. If this is the case, the event is classified as a high momentum event and the core store circuitry and the on-line system are initiallised.

An electron cascade through a momentum tray will activate several cells of the momentum selector and, if any cell forms a straight line combination with the other two trays, the event is classified as a high momentum event. Consequently, there is no loss of high momenta muons because of electron accompaniment and in fact, there is a gain of some muons with lower momenta.

The efficiency of the classification of high momentum events is a function of momentum because the widths of the cells in the momentum trays permit muons of different momenta to activate the same cell configurations. The efficiency of classification is unity for momenta above about 560 GeV/c and falls to zero at about 220 GeV/c.

2.7.3 RUDI

Figure 2.5 shows the trajectory of a muon through the cells of the momentum trays A, B and C; the activated cells are a, b and c respectively. By simple geometry, it can be seen that the deflection, Δ , in units of momentum tray cells,
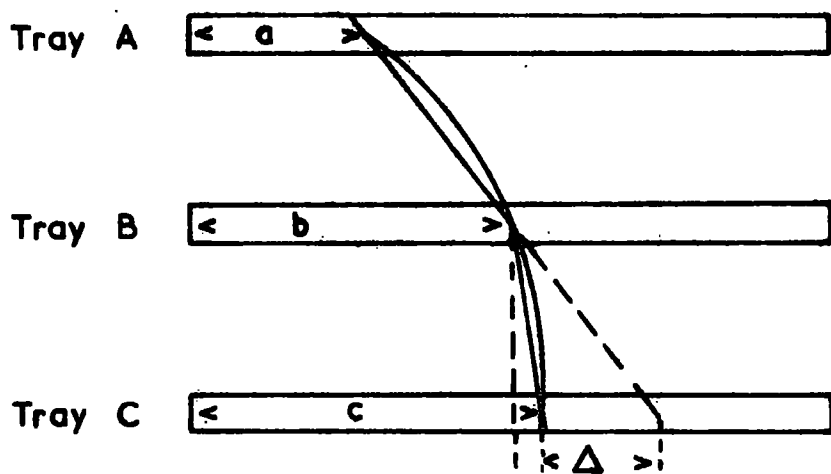
Figure 2.5   The Trajectory of a Muon through the Momentum Trays.
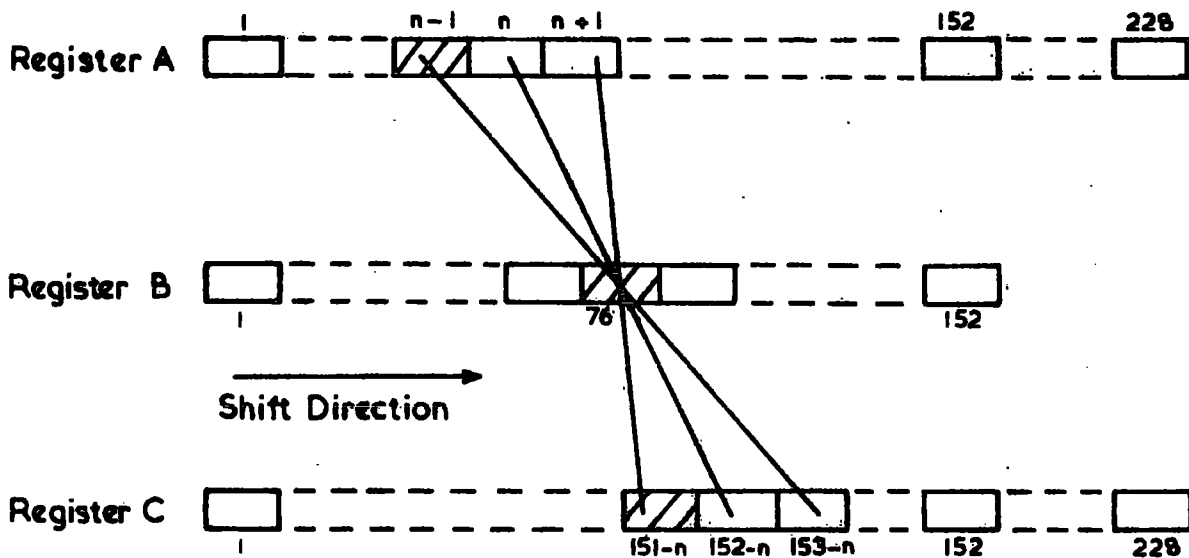
Figure 2.6   The Trajectory of a Muon in the Momentum Selector.

is given by

$$\Delta = (a - b) + (c - b) \qquad (2.6)$$

Whilst the shift registers are being clocked, RUDI counts the clock pulses and observes the arrival of the activated elements of each shift register at element 152. Consequently, it is able to ascertain the values of $(a - b)$ and $(c - b)$. RUDI then attributes a deflection and a sign to the charge of the muon by means of equation 2.6 and a knowledge of the direction of the magnetic field. An address of one of the memories of a P.H.A. is generated and the contents of this memory are incremented by one. The muon deflection spectrum and charge ratio are thus continually produced for the muons and they are recorded in the P.H.A.

2.7.4 The Measuring and Azimuthal Trays

There are five measuring trays in each side of the spectrograph, as shown in figure 2.3. Each tray consists of 89 columns of 8 tubes and the columns are assigned a number in the range 2 - 90. Because the azimuthal trays only consist of four layers of the large tubes, two adjacent columns are taken together to form an eight tube combination.

Column 1 and columns 91 - 96 of each tray are dummy. They are built into the electronics and are always transferred to the computer. Column 1 is the tray identifier and it contains the tray number in binary. The other six columns are used during the analysis of the data for the storage of the answers.

The digital output from these trays is in the form of a column number followed by the tube configuration of that column. Only the columns which actually contain data are transferred. The column number is a number between 1 and 96, is in B.C.D. format (Binary Coded Decimal) and occupies 8 binary bits. Similarly, the tube configuration occupies 8 bits, one bit for each of the eight tubes in a column.

2.7.5 The Core Store

Before the information contained in the measuring trays is transferred to the computer, the event is assembled in a ferrite core store. This not only minimises the transfer time to the computer, which is continually involved in other tasks, but more important, whilst data transfer is in progress, the computer is in complete control and a prerequisite is that data be made available to the computer as soon as it is required. This cannot be guaranteed unless the event is first assembled in a core store because of inherent time delays in the digitisation control circuitry.

The ferrite core store consists of 1024 8-bit words or bytes into which binary information can be stored. Each byte is accessed by presenting a binary address defining the byte required and the necessary control pulses. The core store operates in two modes: the clear-write mode and the read-write mode. The clear-write mode is used to place data in the store, the defined byte first being emptied, and this mode is used to load the core store. The read-write mode displays the contents of the defined byte on the output lines of the core store and then writes the data residing on the input lines back into the byte. This mode is used when the contents of the core store are transferred to the computer. A description of the core store and its peripheral circuitry, including the data channel to the computer, is given in Appendix A.

For each event, the data from the measuring trays is preceeded by an event header. This consists of information relevant to the muon, namely, the event number, the time, date and year, the magnetic field direction, the trigger mode (the side of the spectrograph to which the data pertains) and the prevailing atmospheric pressure. The data, including the tray headers and dummy columns, then follow from each tray in turn. A complete description of the data format is given in Appendix B.

Once the data from the last tray (tray 7) has been loaded into the core store, the event is ready for transference to the computer. The capacity of the core store is sufficient to contain all the columns of tubes of one side of the spectrograph but not, in addition, all the columns of the azimuthal trays. If the core store becomes full, then loading is terminated and the data transferred; any data remaining in the azimuthal trays is lost. This loss should not be detrimental to the experiment, because any event with this quantity of data could only be initiallised by a dense air shower and it would almost certainly be impossible to infer the properties of any individual particle present.

When the loading of the core store is complete the data channel is opened and the transfer of data to the computer takes place.

2.8 The On-line Computing System

The on-line computing system consists basically of two units: an IBM 1130 computer and an interface, which forms the data channel between the computer and MARS. The on-line system services two experiments, namely, MARS and a bubble chamber experiment in which it is used to collect data and supervise the scanning of bubble chamber film. In fact, the latter experiment is the main occupation of the computer and the only service rendered to MARS, whilst film measurements are in progress, is that of data storage. The MARS data are analysed overnight on this computer, when film measurements cease and all the facilities of the computer are available to MARS.

Figure 2.7 is a schematic diagram of the organisation of the computer and on-line experiments. The computer consists of a 1131 C.P.U. (Central Processing Unit) with a 8192 16-bit (2 bytes) word memory and a cycle time of 3.6μs. To this are attached two disc drives, one main and one satellite, a paper tape reader and punch, the console printer and keyboard, and the interface.
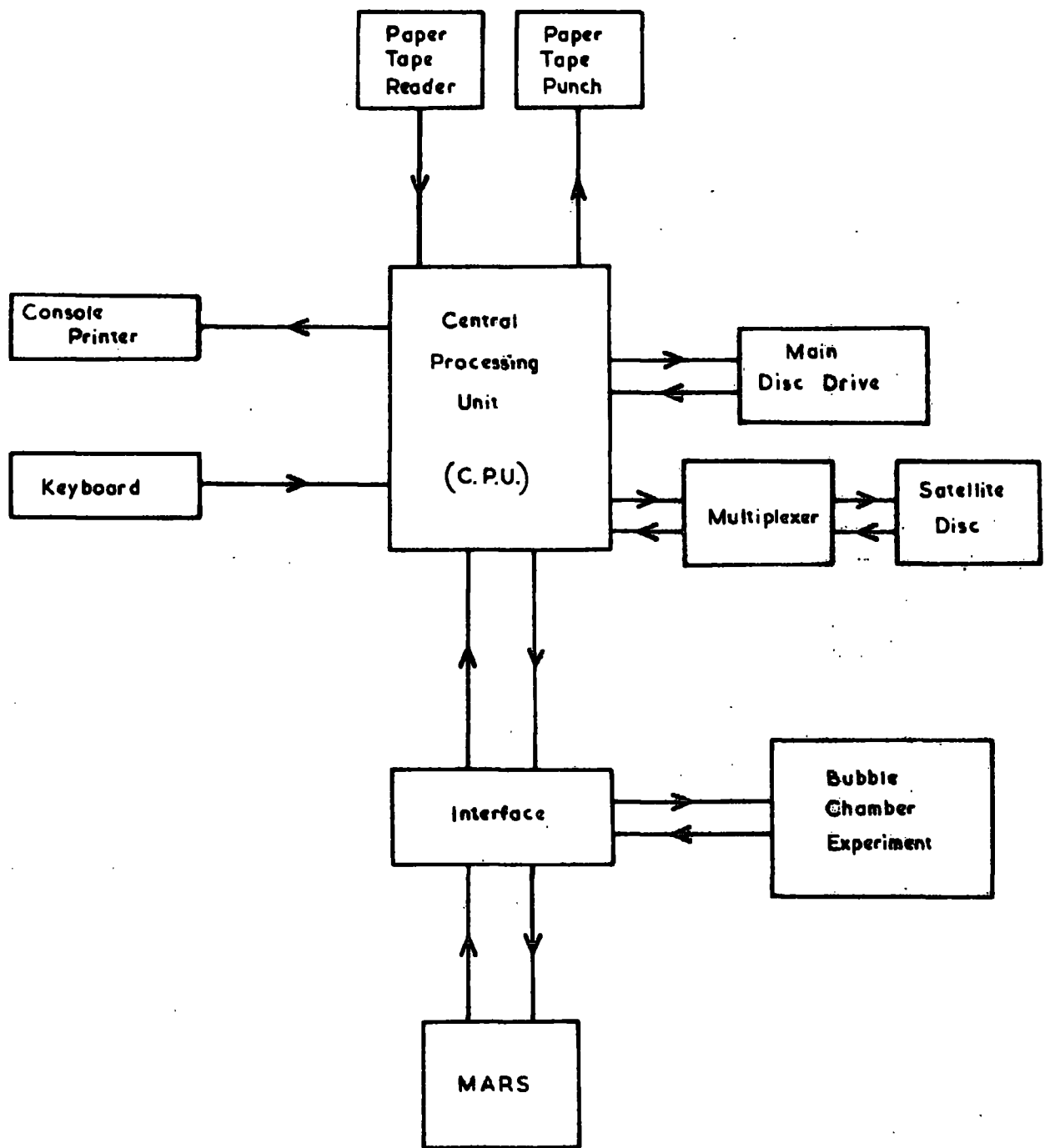
Figure 2.7   The On-line Computing System.

A disc is a magnetic recording device resembling a gramophone record except that its surfaces are coated with magnetic material onto which data can be written or read from at very high speed. Each disc provides the CPU with an extra 512,000 words of memory and their main use is to provide storage areas for data and for computer programmes. A disc is divided into areas known as sectors which are each 320 words long. This is the minimum quantity of words which can be transferred to or from the disc at any one time. The two disc drives attached to the computer provide each experiment with their own data storage areas.

The other main input and output devices are the paper tape reader and punch, and the console printer and keyboard. These provide the main input and output functions required by the computer for job control purposes such as the necessary commands to execute a programme. They also provide output from programmes and the console printer is greatly used, in this respect, to relay messages to the film scanners about the progress of their work.

The interface consists of a large amount of electronics and was specially designed to handle the MARS and bubble chamber experiments. It is connected to the computer by a two-way communications channel which provides for the transfer of commands and data between the computer and the experiments. This channel is composed of four registers. Two of them are each 16 binary bits in length and are known as the read and write buffers. Data and commands from the computer are sent to the interface via the write buffer and data are received back via the read buffer. The other two registers are smaller. One is 4 bits long and is known as the control register. The interpretation of the contents of the write buffer by the interface depends upon the contents of this register. The other register is 6 bits long and is known as the interrupt buffer. The bits of this register inform the computer of the state of the read buffer and which experiment is requiring service.

2.9   The Interrupt Principle of the Computer

The IBM 1130 computer, when handling input and output devices, operates on the interrupt principle. When a device requires some kind of intervention into its actions by the CPU (such as the transfer of more data), the device interrupts the CPU by setting one of the bits of an internal register of the computer. The setting of this bit is immediately acknowledged by the CPU and control is passed from whatever tasks the CPU was pursuing at that time to the programmes residing in core which handle the device. When the servicing of the device is complete, control of the CPU is returned to the point in its tasks where the interrupt occurred.

The majority of the input and output devices on the computer are much slower than the CPU itself and the philosophy of the interrupt principle is that the CPU is not tied to the timing of these devices. Consequently, the CPU is able to perform other tasks whilst awaiting the response from the device and it is also possible to operate several devices simultaneously. This is not true of the interface because it is a fast electronic device, but it does mean that the CPU can be fully occupied, for example with data analysis, and only be interrupted when required by the experiments.

2.10   The Operational Principle of the On-line System

After the core store has been loaded, a pulse is sent to the interface to signify that MARS requires servicing. Bit 4 of the interrupt buffer is set and the computer is interrupted. The computer then acknowledges the interrupt and examines the interrupt buffer to ascertain which of the two experiments requires service. (The bubble chamber experiment sets bit 5 of the interrupt buffer). Having decided that MARS was the cause of the interrupt, the computer opens the data channel to the core store by setting line 1 of the control buffer and placing a special code (binary 79) in the write buffer. This is interpreted by the interface as a control command and the channel is opened. Control line 1 is then reset. The computer then proceeds to send addresses to the core store

and to receive the data from the core store. This is accomplished by setting control line 1 and placing the address of a core store byte in the write buffer. The addresses are produced in logical order starting at zero. The interface transfers the address to the core store together with a pulse which cycles the core store in the read-write mode. The computer waits for bits 1 and 2 of the interrupt buffer to be set, signifying that data have been received from the core store, and it then reads in the data from the read buffer. Control line one is then reset and the cycle repeated with the next address.

The electronic control circuitry of the core store counts the number of addresses received from the computer and, when all the data have been transferred, a control bit is set on the read buffer to signify to the computer that transmission is complete. The data channel is then closed by the presentation of another special code (binary 1024) to the interface in conjunction with the setting and resetting of control line 1. The CPU then returns to continue its other tasks.

The data received from the core store are only one byte long and, to economise disc storage space, two bytes are packed together into one 16-bit computer word. The data are retained in the core of the computer until 320 words have accumulated and they are then transferred to the next available sector of the data storage area of the satellite disc.

This disc is transferred to the main disc drive at night for the data to be analysed by the programme to be described in the following chapters. An empty disc is placed on the satellite drive where data collection continues for another 24 hour period.

CHAPTER 3

The Data Analysis Techniques, Aims and Problems

3.1 Introduction

The automatic collection and analysis of data, especially in large quantities, means that much of the data will go unseen and a great responsibility lies with the computer programmer to ensure that the data is, in all cases, correctly interpreted. The constituent flash-tubes of previous spectrographs have been recorded photographically and the patterns interpreted by film scanners. Before writing the computer programme to analyse the MARS data, a study was made of the actions of the scanner and the decisions made by him in his interpretation of the data, especially with respect to the fitting of trajectories to flash-tube patterns. These actions and decisions were then expressed as logical procedures for the computer and included in the analysis programme.

This chapter is devoted to a description of the analysis techniques adopted and the problems encountered. A more detailed description of the actual programme is given in Chapter 4.

3.2 The Aims of the Programme

The basic aim of the programme is to interpret the binary coded information, transferred from the measuring trays and peripheral equipment of MARS to the IBM 1130 computer via the on-line data channel, and to perform the following functions:

a) to determine the number of particles traversing the instrument,

b) to eliminate spuriously triggered events e.g. those due to air showers,

c) to distinguish and flag electron cascades in any of the flash-tube trays,

d) to determine the momenta of the muons present,

e) to determine the sign of the charge of the muons,

f) to determine the projected zenith and azimuthal angles of the trajectories of the muons,

g) to provide for further collection of data from MARS during data analysis,

h) to continuously monitor and check the performance of the digitisation, the data channel and the general spectrograph operation,

j) to convert the basic binary information and answers into a form in which it can be transferred to the IBM 360/67 NUMAC (Northumbrian Universities Multi Access Computer) at Newcastle, via a land line (16 miles), for storage on magnetic tape and to make such data easily accessible from a Fortran environment on that computer.

Muons are detected by a 3-fold coincidence from the scintillation counters of one side of the spectrograph. Unfortunately, a coincidence may be generated in ways other than by the traversal of a single muon through the three counters, for example, as the consequence of an oblique extensive air shower or by a pair of muons, neither particle traversing the entire instrument. A chance straight line combination in the momentum selector classifies the event as a high momentum event and it is a necessary function of the analysis programme to distinguish and flag such events which occur in the data.

The mean discharged flash-tube density along a muon track in a tray is 5.21 and normally, there are no more than two discharged tubes in any one layer. Occasionally a wide region of a tray is discharged by an electron cascade accompanying the muon. These originate from electromagnetic interactions of the muon in the material above the tray.

The resulting cluster of discharged tubes is known as a burst and, because the high tube density renders them useless for track location purposes, the flow of the analysis programme must be adjusted whenever one is encountered. The

expected probabilities of occurrence of these bursts, as given by Said (1966, see figure 2.1), increases rapidly with muon energy and is 4% per magnet block at 100 GeV and 17% at 1000 GeV. Consequently, with MARS and for muons with an energy of 1000 GeV, there is a 39% chance of seeing one burst and only a 47% chance of seeing a track without any bursts. Clearly, it is most important that the programme should handle these bursts correctly. When the spectrograph is operated such that there is no absorber above tray 5, this tray will not be greatly affected by bursts, but it will be affected by small air showers. This again is expected to be more important at the highest energies, where the muon is more likely to be close to the axis of a shower, where particle densities are highest.

It was shown in section 2.2.1 that the radius of curvature of a charged particle in a magnetic field is proportional to its momentum and this radius may be found by reconstructing the trajectory of the muon through the discharged flash-tubes of the spectrograph. The direction of curvature and of the magnetic field determine the sign of the charge of the muon. The actual momentum measured in this way by MARS is the projection of the true momentum on the plane normal to the magnetic field. The true momentum may be derived if the projected zenith and azimuthal angles are known and these may also be found from the trajectory reconstruction. The theory of the derivation of the true momentum and also the true zenith and azimuthal angles is given in section 3.7.6. A knowledge of the true azimuthal and zenith angles is essential if the momentum of the muon is to be calculated at its production, because it is necessary to know the thickness of atmosphere traversed by the muon to allow for the energy loss. This is especially important in the horizontal direction where path lengths are large and, because of the earth's magnetic field, they are different for each sign of the charge of the muon. This has an important bearing on the observed charge ratio.

Whilst data analysis is in progress, it is intended to continue operating MARS. Consequently, the computer must be available at any time for the storage of data and data analysis will be frequently interrupted for that purpose. An important programming consideration is that the storage of new data does not interfere with the data analysis, besides a brief interruption, and that interrupts at inopertune moments in the analysis are delayed until a position is reached where data storage may proceed. This occurs when the analysis programme is using one of the disc drives and MARS requires to store data. If data storage was allowed to proceed immediately, there is a high probability that the disc handling routines would not be able to cope and a programme error would result.

The computer is able to monitor continually and check the performance of the spectrograph because the data, other than the actual tubes discharged, are in a strict format defined by the digitisation electronics. It is easy for the analysis programme to compare the data with the expected format and flag any discrepancies. For example, only in the header information are data words allowed to be zero. If this is otherwise, then information has been lost between the flash-tubes and the computer. A complete list of the various errors flagged by the programme is given in table 4.1.

The NUMAC computing system at Newcastle, to which Durham University is attached by a land line, consists of an IBM 360/67 computer, which provides a very large and fast CPU and large amounts of back-up storage on magnetic tapes and discs. This facilitates easy handling of large amounts of data such as that accumulated by MARS over the period of several months. All the data collected by MARS are stored on magnetic tape on this machine after processing on the 1130. The best programming language environment to work in on the 360/67 is a high level one, such as Algol or Fortran, and, as the data from MARS are in coded binary, it is necessary to translate this data into a form which can be accessed

by a high level language. Hence an integral stage of the data analysis is the translation of this data into a form which can be accessed by programmes on the 360/67.

All the features described in this section have been included, at various stages, in the programmes for the analysis of the MARS data. Several environmental problems had to be considered whilst the programming was in progress and these are described next.

3.3 Environmental Problems and Considerations

The on-line IBM 1130 computing system has been described in the previous chapter. As a computer it is rather small and slow and is limited in the operations it can perform. However, it is ideally suited to small, on-line experiments such as MARS and the bubble chamber experiment, and where a much larger and versatile computing system (NUMAC) is at hand, to which data received by the on-line system may be sent for further and more detailed processing.

Unfortunately, the NUMAC computer is extensively used by the Universities of Durham and Newcastle, and there is insufficient time available each day for the processing of all the data collected by the on-line system. Whenever MARS is running, it is necessary to have the 1130 computer operational to collect data. During the daytime, the computer is involved in other tasks but, overnight and at week-ends, its services are only required by MARS and then only for a few milliseconds every one or two minutes. It is idle for the remainder of the time. It was decided to take advantage of this available computing time to analyse the data from MARS. Eleven hours of computing time every night and all of the week-ends are available and this is more than sufficient to perform a complete analysis of the data.

The major limitation of the IBM 1130 computer is the size of its core. This consists of 8192 16-bit words of which 7502 are available to the user, the remainder being occupied by the resident monitor including the disc handling routine. In addition, 450 words are required by the programme and

data storage area for the on-line system. Consequently, any programme to analyse the data must be contained in the remaining 7052 words of core.

Two programming languages are available to the user of the IBM 1130 computer. One is a high level language, Fortran, and the other a low level language, Assembler. The main differences between these two languages is that the Fortran compiler is responsible for the translation of programming instructions into machine code, whereas with Assembler (which is symbolic machine code) the translation is the responsibility of the programmer. As a result, it is very much easier to programme in Fortran, but execution time and the amount of core required by the programme can be considerably reduced by writing in Assembler. For these reasons and also the fact that the binary data from MARS is difficult to handle in Fortran, the programmes to analyse the MARS data have been written in Assembler language.

As the data are analysed, a large amount of output is produced by the programmes which, not only includes the results of the data analysis, but also a description of the decisions made by the programme in arriving at these results. The handling of this output, and also the data itself, promotes a serious problem because there is no fast output device on the computer to which this information can be sent, other than the discs. The main input and output device in Durham for the NUMAC computer is also an IBM 1130 computer, which has a fast line printer attached to it, and it is able to accept discs from other 1130 computers. It is thus possible to transfer discs from the on-line system to this computer and either, print the answers on the printer, or transmit the data to Newcastle for storage. The only prerequisite is that the data for transmission be on the disc in pseudo card images, so that, as far as the NUMAC computer is concerned, the input is coming from cards.

3.4   The Analysis of the Data - A General Outline

3.4.1   The Scanning of the Data

The quantity of data for any event is variable and it is solely dependant upon the number of flash-tube columns containing discharged tubes. The events

are packed together as the data are received and stored on the disc. A long data file is thus created amounting to about 200 sectors of the disc for a 24 hour collection period; there being between 4 and 5 events per sector.

The analysis programme systematically works through this data file and its first task is to identify each event in turn, and the amount of data pertaining to it. The data for the event are then scanned and divided up into the various flash-tube trays. The direction of the magnetic field and the trigger mode of the spectrograph (the side of the spectrograph from which the data came) are extracted from the header information. These are required to define the sign of the charge of the muon and the co-ordinates of the flash-tube trays (the latter being different for each side of the spectrograph).

3.4.2 The Scanning of the Trays

Each tray is examined in turn and they are subdivided into groups of discharged tubes through which the muon could have passed. A group is defined as a cluster of tubes, seperated from any other group by at least two empty columns, and containing at least one discharged tube in any three of the eight layers. This was introduced to distinguish between spuriously flashing tubes and the actual muon track but, because of tube inefficiencies, a loss of some muon events results.

The theoretical layer population frequency distribution is shown in figure 3.1 and was derived using a Monte Carlo technique. All tracks up to an angle of 9° were considered together with the triangular angular acceptance function of the spectrograph. It can be seen that no tracks have a tube population of only two tubes and the only candidates for such a population are those tracks with inefficient tubes . It is calculated in Chapter 5 that 14% of all tracks have one inefficient tube and this corresponds to a tube internal efficiency of 96.6%. Folding this efficiency into the layer population frequency distribution yields a 0.13% probability of observing a tray with only two tubes along a muon track. Consequently, for the five measuring trays,
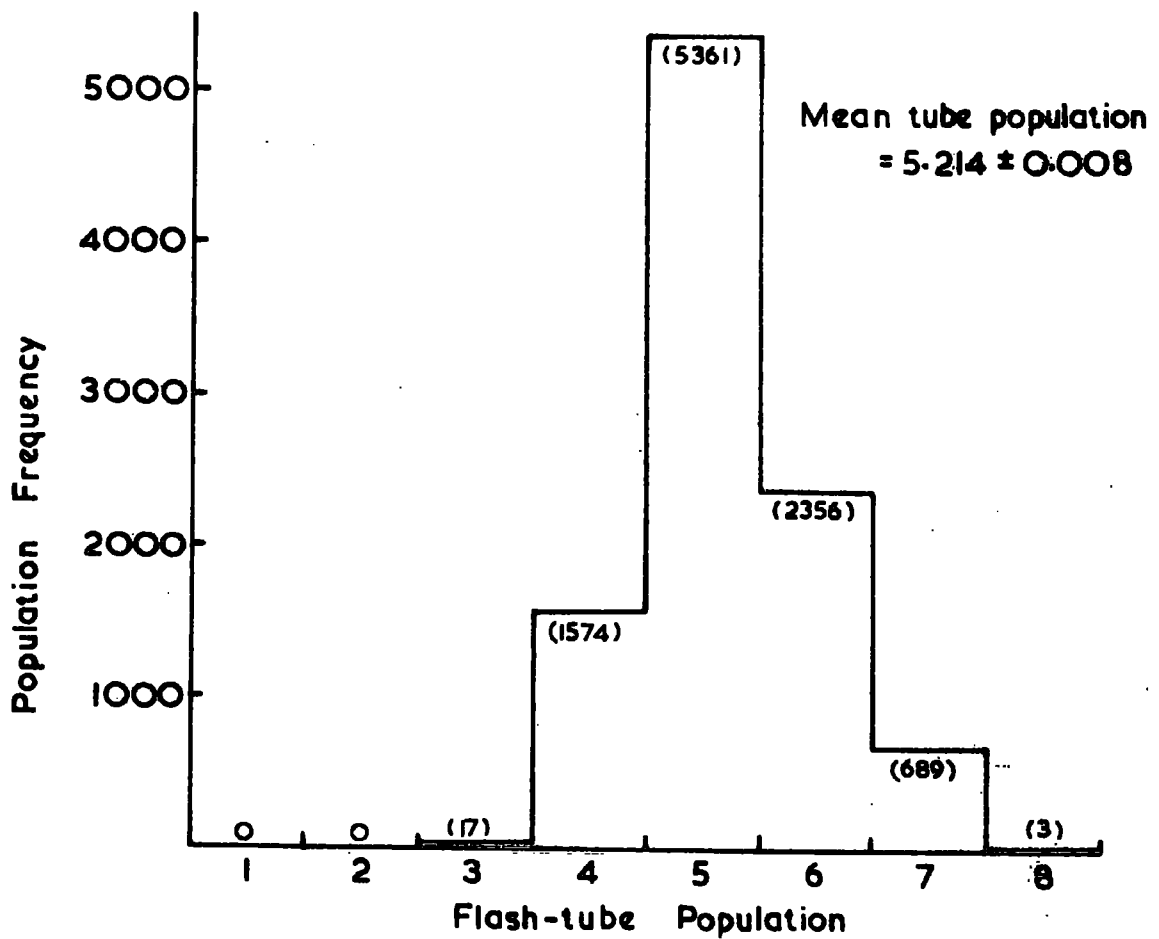
Figure 3.1 The Theoretical Tube Population Distribution for the Measuring Trays.
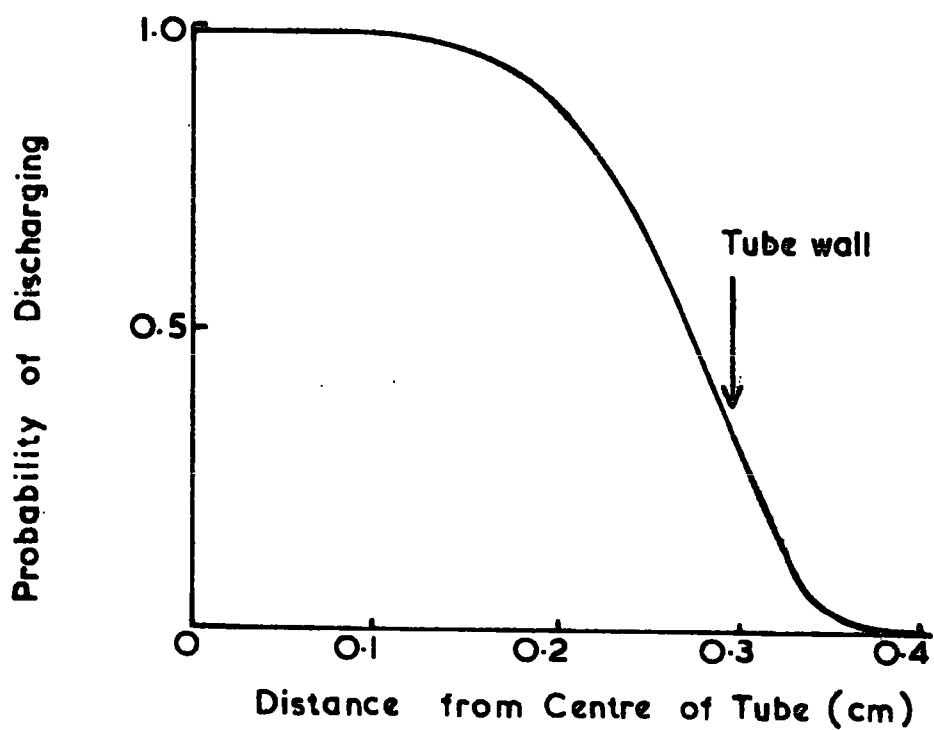
Figure 3.2 The Flash-tube Discharge Probability Function of Bull et al.(1962)

0.62% of all events will be lost because of the insistence that at least three layers contain discharged tubes. This loss will be momentum independent and will therefore not distort any derived spectrum.

If a group comprises more than 5 columns or more than 10 discharged tubes, the group is said to contain a burst and is not used directly in later calculations. These figures were derived after a film study of bursts in flash-tube trays. For a muon with a momentum 100 GeV/c, the maximum angle of the muon's trajectory through a flash-tube tray, even allowing for an increase in angle due to magnetic bending, is 9° and consequently its trajectory should always be contained within two tube columns. It was found that, whenever the track occupied more than two columns, the muon was apparently accompanied by another particle and, if it spread over more than five columns, there was little chance of extracting any information as to where the original muon passed. The theoretical mean tube population along a track was found to be 5.214 ± 0.008 from the distribution of figure 3.1, and so, if there are more than 10 tubes discharged in a confined region of the tray (five columns or less) then there are at least two particles present. The interference of these particle tracks with one another makes it difficult to ascribe specific tubes to each particle, and a limit of 10 tubes was introduced into the track fitting routines above which the results of the track fitting were adjudged to be suspect.

Normally, there is only one group of tubes in a tray but occasionally there are more. These are due to accompanying particles, either another muon or a particle arising from an interaction of the muon somewhere in the spectrograph. It is necessary for the analysis programme to determine which group of tubes pertains to the actual muon and which were due to the other particles. If there are more than two groups in a tray, the tray is deemed unusable and no further examination of that tray takes place. This feature was introduced to assist in the elimination of large bursts and air showers and also to reduce the number of calculations to be done by the analysis programme and the amount of core

storage that would have been required for them.

3.4.3 The Fitting of the Trajectory

The handling of multiple groups, bursts and unusable trays is dealt with in detail in Chapter 4, where a complete description of the analysis programme is given. For the purposes of the present outline, we shall confine our attention to an event comprised of a single, unaccompanied muon with one group in each tray, none of which contain bursts.

Each group in the five measuring trays is examined in turn and the muon trajectory is located in them. The actual procedure for this is described in section 3.6, but briefly, the flash-tube pattern is studied and a small region of the tray through which the muon passed is defined. The mid point of this region is then used as an approximate co-ordinate for the muon in that measuring tray during the next stage of the calculations.

A more precise point can be defined in the measuring tray if the angle, at which the muon traversed the tray, is known. This also forms a criterion for selecting the group pertaining to the muon when more than one group is present in a tray, because it is unlikely that both groups will contain tracks at the correct angle. The angle at a measuring level is defined by constructing the entire trajectory of the muon through the spectrograph using the approximate co-ordinates, and taking the differential of the resulting curve at the measuring level. This angle is defined very precisely because the approximate co-ordinates are only in error by a fraction of a millimetre and the change in angle due to such an uncertainty is negligible over the length of the spectrograph.

The trajectory fitted to the co-ordinates is a parabola and, for the fitting purposes, the magnet is assumed to be a continuum of iron, rather than a multilayer device. Consequently, two approximations are introduced: firstly, the parabola is not an accurate description of the projected trajectory, which is, more precisely, four arcs of a circle joined by tangents, and secondly,

the magnetic path length is increased by assuming a continuum of iron. It is shown in section 5.6 that the effects that these approximations have on the analysis of high momentum events are either negligible or necessitate the application of a simple, momentum independent, correction factor to the results.

Once the angle of the trajectory has been defined at each level, a more precise determination of the co-ordinates of the trajectory is made, and a final parabola is fitted to these new co-ordinates. The momentum of the muon and projected zenith angle are then calculated from the coefficients of the parabola fit, see section 7, and the sign of the charge of the muon is derived from the direction of the magnetic field and the direction of curvature of the trajectory.

The projected azimuthal angle is found from trays 6 and 7, the azimuthal trays, by simply calculating the mean points of the discharged tubes in a group, in each of the two trays and finding the angle subtended. No actual track fitting is attempted in these trays because of the lack of sufficient core storage for the necessary programmes and also because the method is sufficiently accurate as not to merit a more detailed analysis. The accuracy attained is discussed in Chapter 5.

3.4.4 The Storing of the Answers

The muon's momentum, projected zenith and azimuthal angles, together with other information relevant to the goodness of the parabola fit and the decisions made by the analysis programme, are then placed in an answer file on a disc and also inserted back amongst the data in the dummy columns of the event. It is necessary to have the answers stored in these two different ways because it keeps the answers and data together for transmission to the NUMAC computer. In addition, if the programme is unable to interpret the data of a particular event, nothing can be inserted back amongst them, whereas the answer file contains the error code indicating the fault with the data.

3.4.5 Completion of the Analysis

Having stored the answers, the analysis of the event is complete and the programme then continues with the next event. This process continues until the end of the data file is reached and analysis is terminated.

At some later time, the answer file is transferred to the line printer of the IBM 1130 satellite computer of NUMAC, where a list of events and answers is produced. The data file, and its embedded answers, are also translated into card images on another disc, and that disc is transferred to the satellite IBM 1130 and the data transmitted to the NUMAC computer. Here the data and answers are stored on magnetic tape where it is available at any time for further study.

3.5 The Location of the Muon's Trajectory in the Flash-tube Trays

3.5.1 Review of Previous Techniques

The flash-tube has been widely used in cosmic ray spectrographs over the past fifteen years and, during that time, a variety of methods have been developed to locate accurately the particle trajectories in the flash-tube trays. Ashton, Kisdnasany and Wolfendale (1958) compared three methods of determining the best estimate of the trajectory. Their experimental arrangement consisted of two flash-tube trays, some distance apart, and their aim was to determine the angle at which the particle traversed the trays.

The three methods examined were as follows:

i) A line was drawn between the centre of gravity of the discharged tubes in each tray.

ii) A cotton fibre was adjusted across the surface of a full scale diagram of the tube assembly to give the best estimate of the track direction.

iii) The photographic records were projected onto a rotatable screen, ruled with close parallel lines, and the direction of a line determined which satisfied the condition that the sum of the distances from the centre of the flashed tubes to the line was a minimum.

They compared the results obtained by the three methods and concluded that, although method (i) was objective, it was inferior to methods (ii) and (iii) because it did not utilise the information available about the approximate angle of the track, as defined by the two trays taken together. Methods (ii) and (iii) utilised this information but were both subjective in that they required the scanner to interpret the flash-tube patterns in some way. Of these two methods, they concluded that method (ii) was more accurate because not only the tubes but also the gaps between their sensitive regions could be used to locate the trajectories.

Hayman and Wolfendale (1962) analysed data from a similar experimental arrangement to that of Ashton et al., by a track simulator method. The device consisted of an enlarged model of the flash-tube tray fronts in which the discharged tubes were represented by illuminated lights. The track was located by placing a cursor across the tube pattern, at the angle defined in conjunction with the tubes in other trays, and then positioning it laterally using certain criteria. A comparision of the location accuracy achieved by this method with that obtained by the authors simply placing a cursor on projected images of the events, shows that the track simulator was 2.5 times more accurate.

A widely used computer method for the analysis of flash-tube data has been described by Bull et al. (1962). Their method utilises the probability of a flash-tube discharging as a function of the distance the particle passed from the centre of the tube, and the probability distribution used is shown in figure 3.2. Tracks are drawn between the flash-tube trays and the probability of a tube flashing or not flashing is calculated at each layer. The product of these probabilities gives the total probability for the track and the track with the highest probability is selected. Hayman and Wolfendale (1962) compared the accuracy of the computer technique with their own and found little difference in the attained trajectory resolution.

3.5.2. Conclusions and Discussion

It is concluded from the preceeding review that it is essential to include two features in any trajectory location technique if high precision is to be attained and they are

1) that the gaps between the sensitive areas of the tubes through which the muon passed should be used, as well as the discharged tubes, for track location purposes, and

2) that due consideration should be given to the required angle of the track in a tray as defined by the other flash-tube trays.

Several other properties of flash-tube trays must also be considered, namely

1) that a flash-tube may be discharged in a layer after it has been traversed by a locally generated knock-on electron, whereas the muon passed outside of the tube's sensitive volume;

2) that flash tubes are not 100% internally efficient and they may not discharge after being traversed by an ionising particle; and

3) that there is always an uncertainty in the position of each individual tube because of the variations in the tube diameters and the bending of the tubes.

Hayman and Wolfendale (1962) commented that they encountered difficulties in establishing fitting criteria for their track simulator because of the first two effects but they do not state what were finally adopted. The use of a probability function by Bull et al. (1962) is an attempt to allow for all three effects, but the success of this method is dependant upon the severity of the interference of these effects with the actual track. For example, consider two identical tracks in a flash tube tray, if, for one of these tracks, there was a knock-on electron or a tube inefficiency in one layer, then the analysis of the two tracks with the Bull et al. probability function would yield two different trajectories. This is because the trajectory will be biased either towards (for knock-ons) or away from (for inefficiencies) the offending tube and will never coincide with the true trajectory.

It is shown in Chapter 5 that the probability, P_{KO}, of there being a tube on a muon track, which was discharged by a knock-on electron, whereas the muon passed outside of the sensitive region of the layer containing the tube, is $17.2 \pm 2.0\%$ per tray. Consequently, $(40.4 \pm 0.8)\%$ of the events will have one knock-on in one of the five trays and $(38.9 \pm 4.7)\%$ will have none at all. Similarly, for tube inefficiencies, the expected probability of occurrence, P_{IN}, is $(14.2 \pm 3.7)\%$ per tray, and consequently $(38.5 \pm 3.4)\%$ of the events will have a tube inefficiency in one of the five trays and $(46.5 \pm 10.0)\%$ will have none. The probability of an event having neither tube inefficiencies or tubes discharged by knock-on electrons in any tray is given, approximately, by $(1 - P_{IN} - P_{KO})^5$ and hence $(84.4 \pm 4.7)\%$ of all events will be contaminated in some way, in at least one tray.

Contamination of the data in a flash-tube tray also occurs when the muon is accompanied by other particles emanating from the magnet blocks. These, even if they do not traverse the whole tray, cause flash-tubes to discharge which do not lie on the muon's trajectory. It is difficult to see how a probability function could interpret this data correctly and produce the correct trajectory, because every discharged tube, even if it is completely unrelated to the trajectory of the muon, is included in the fit. The only way to interpret this data correctly is to do exactly what the film scanner would do and that is to eliminate the extraneous tubes from the data using certain criteria.

It is for these reasons that the technique involving the tube discharge-probability function, as used by Bull et al. (1962) to analyse flash-tube data, is considered to be unsatisfactory and an alternative technique has been adopted.

3.6 A New Computer Technique for the Analysis of Flash-Tube Data

3.6.1 Introduction

The only method by which consistent answers as to the position of the trajectory of a particle in a flash-tube tray may be produced from two

identical tracks, except that one has suffered a knock-on electron or a tube inefficiency, is to isolate the offending tube and correct it accordingly by turning it 'off' or 'on'. This method is open to criticism because the data are being altered and there is a chance that the wrong correction may be made to them. In Chapter 5, a comparison is presented between the decisions of the programme and certain properties of the data which reflect knock-ons and inefficiencies, and experiment and theory agree exceedingly well. It is concluded in Chapter 5, that these results justify the decisions made by the programme and that the technique is successful.

3.6.2 The Basic Technique

The flash-tube configuration in a tray is examined and one tube is selected from each layer that contains a discharged tube. If a layer contains more than one tube both are taken in turn and the process, described below, is repeated for both of them. A straight line is fitted, by the method of least squares, to the co-ordinates of the centres of the tubes. The layers which do not contain any discharged tubes are then examined and the centre point of the gap, between the sensitive areas of the flash-tubes nearest to the line, is selected. A co-ordinate is thus obtained for every layer and a new line is fitted through them.

Small perturbations of position and direction are now made around this new line to see if it is possible to draw a line through this configuration of flash-tubes without violating any information. This occurs when a line cannot be contained within all the discharged tubes and selected gaps at the same time. The perturbations made are shown in figure 3.3. Six points are defined above and below the tray, centred around the fitted line, and they are $^1/10$ th of a tube spacing apart.

All the possible lines (36) are drawn between these points and for every line a check is made to see if any information is violated. If, for a few lines, no information is violated, then the track is considered to be satisfactory. If none of the lines fit then there is either a tube present which was discharged
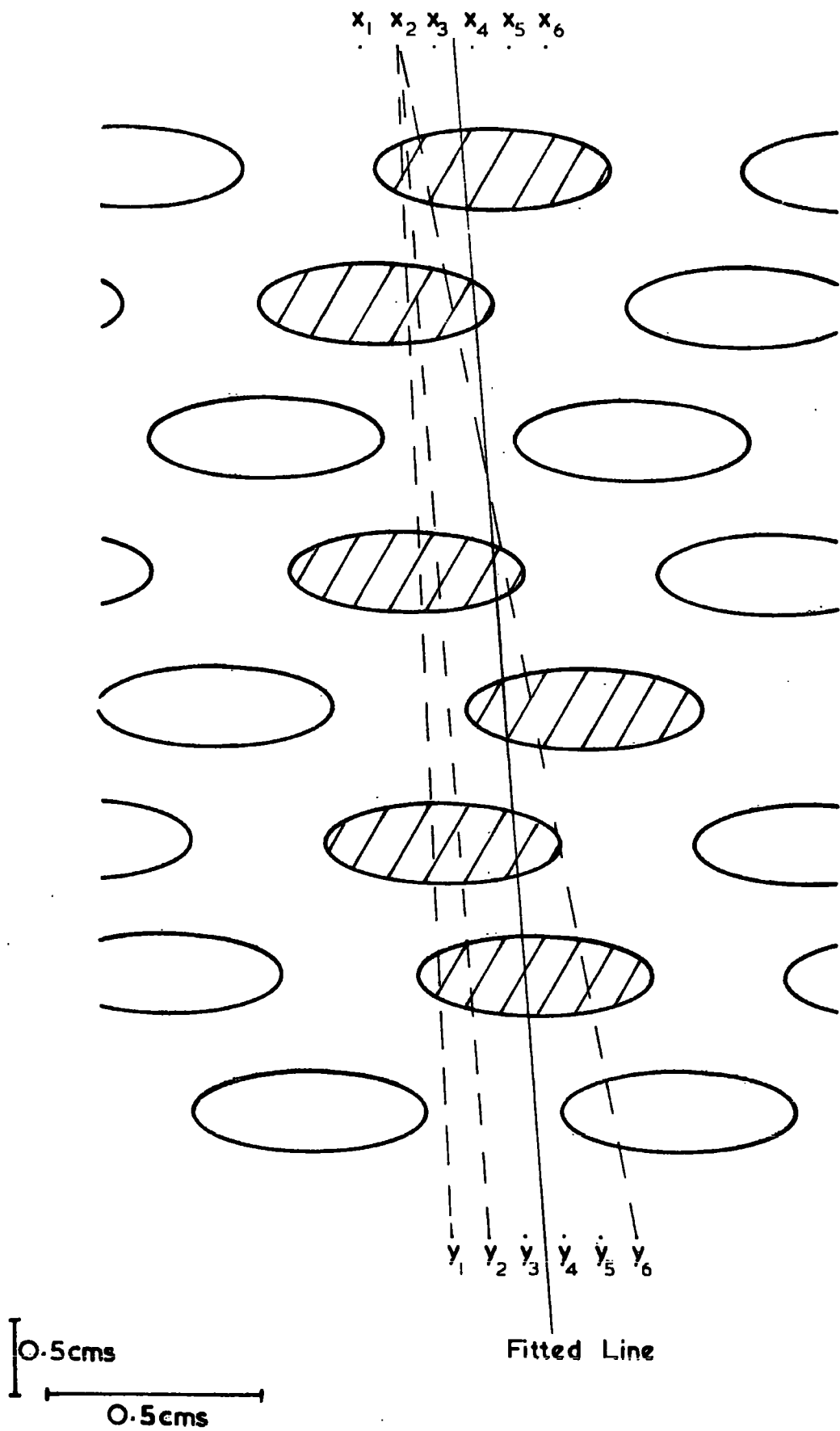
Figure 3.3   The Perturbations Made in the Position and Direction of the Track.

by a knock-on electron, rather than the muon, or a tube has been inefficient.
In this case the programme has several options open to it to try and detect
and adjust what is wrong with the data. These are discussed in the next section.

The lines that are drawn through the tray define a channel through which
the muon could have passed and a typical channel is shown in figure 3.4. The
position of the centre of this channel at the centre of the tray (between tube
layers 4 and 5) is taken as the approximate co-ordinate of the track until a
more precise value is available, after using an angular criterion at a later
stage in the calculations.

3.6.3 Knock-ons, Inefficiencies and Bent Tubes

As mentioned in section 3.5.2, there are three properties of flash-tube
trays which must be taken into consideration when analysing flash-tube data,
namely, tubes discharging due to knock-on electrons, tube inefficiencies and
the uncertainty in the absolute diameter and position of each tube. These all
render the data difficult to analyse and it has been necessary to include
features in the analysis programmes for the MARS data in an attempt to resolve
these difficulties.

Allowance is made for the variation in tube diameters and for bent tubes by
letting the internal diameters of the tubes and the gaps between their sensitive
regions overlap by a small amount, as shown in figure 3.5. This, in effect,
produces a small, neutral region around a tube wall for which, if the muon track
lies within it, no regard is taken as to whether the tube discharged or not.
The amount of overlap required depends upon the properties of the flash-tube trays
and it is very difficult to measure directly. In Chapter 5, a detailed analysis
is described of a sample of data which was analysed with various sizes of overlap.
It is concluded in that chapter that an overlap of 5% of a tube spacing is
required at each edge of a tube for the MARS measuring trays.
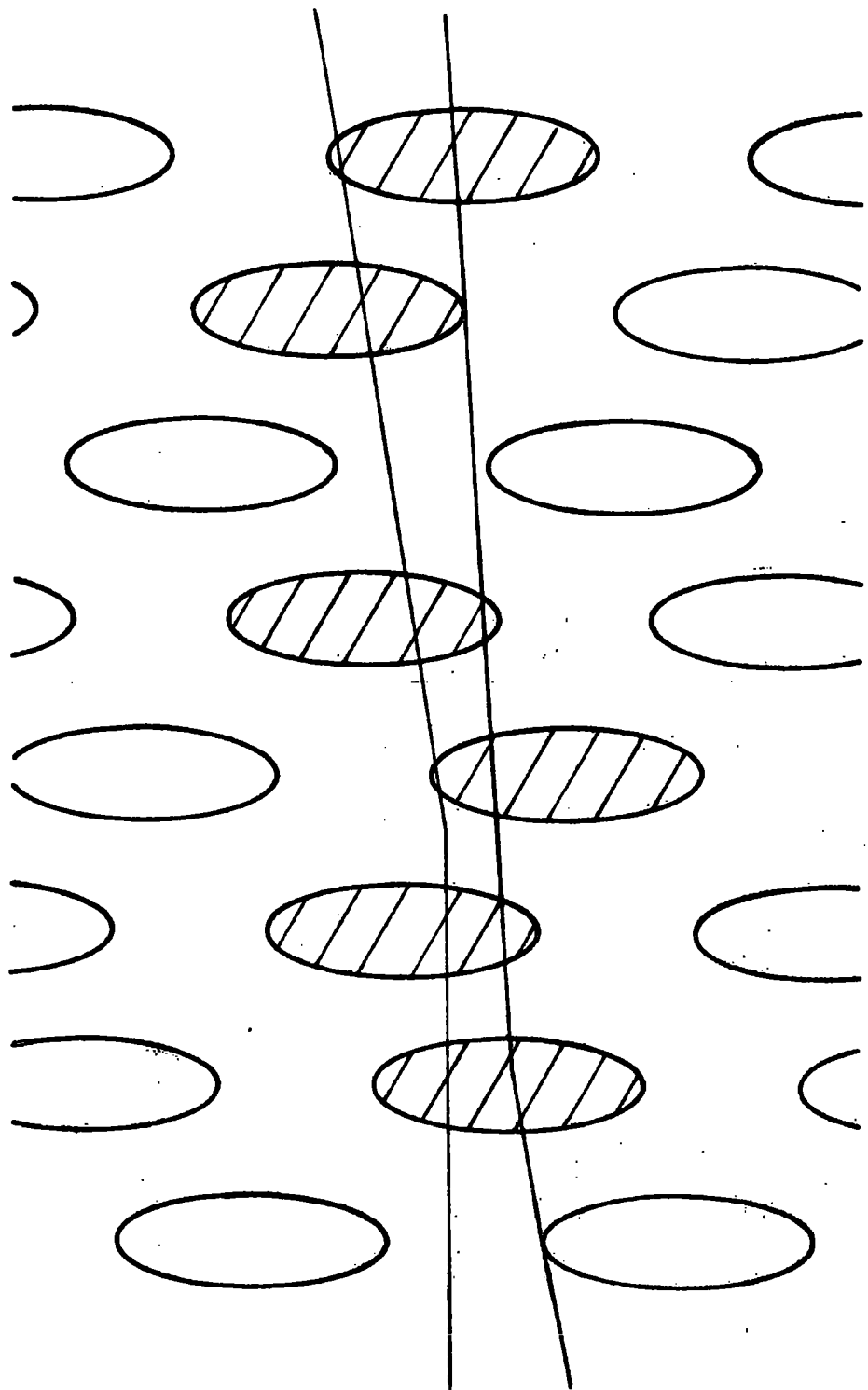
0.5 cms

0.5 cms

Figure 3.4   A Typical Channel through Flash-tube Tray.
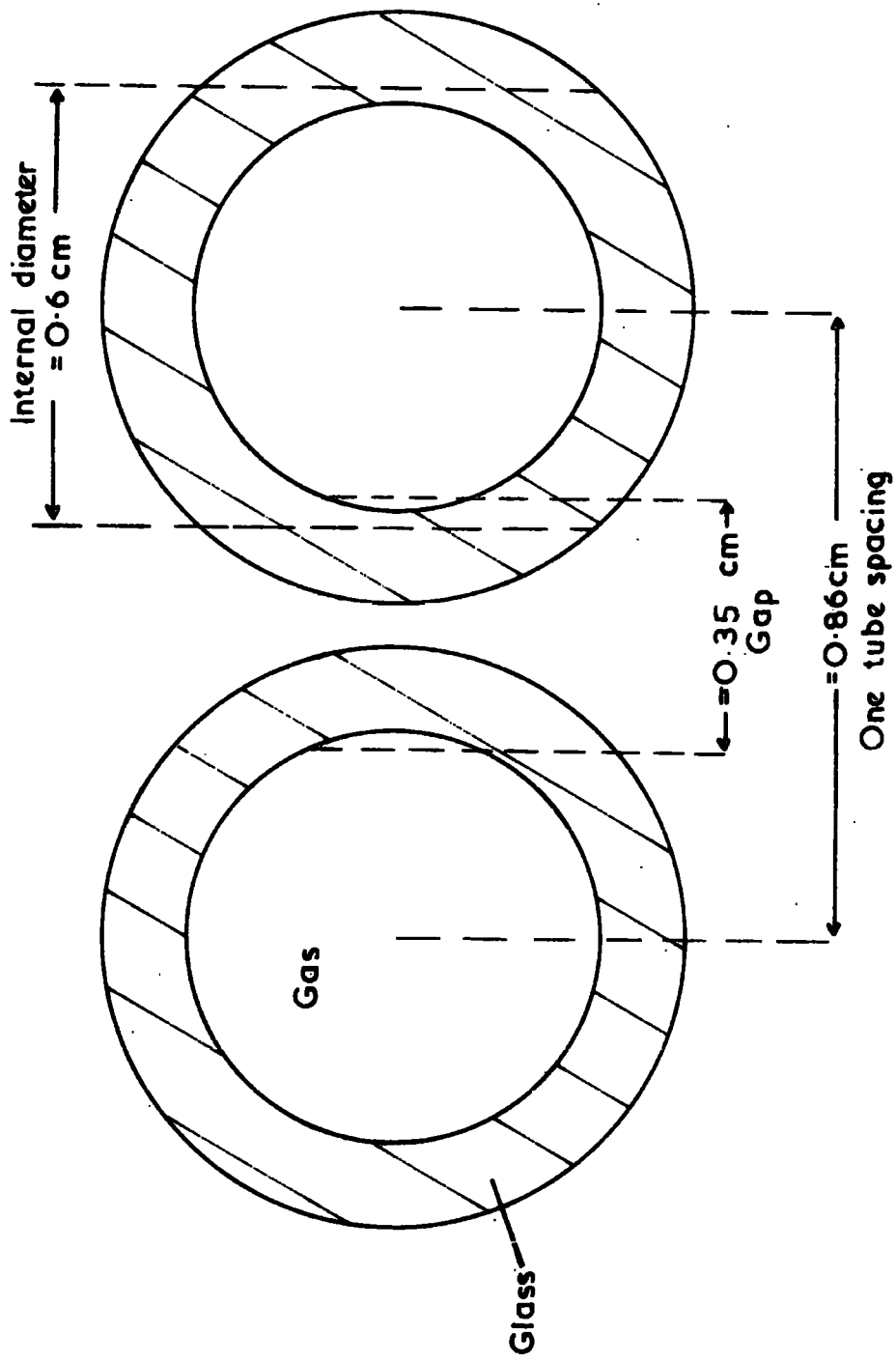
Figure 3.5   The Overlap of the Tube Internal Diameters with the Gaps between them.

If it is impossible to draw a line through the tube configuration, then the programme has a series of options open to it which adjust the tube pattern. These options are examined in order of decreasing probability until a particular option produces a configuration which satisfies the fitting criteria. A list of these options is given in table 3.1 and they are illustrated in figure 3.6.

The first option is that of a single tube which was discharged by a knock-on electron, rather than the muon. The programme turns 'off' the tube from one of those layers which contains only one discharged tube in turn and then tries to refit the track. Consequently, the track is forced to lie outside of the sensitive regions of each layer in turn. If a successful fit is achieved with this option, the analysis is complete otherwise further, less probable options are tried. For tube inefficiencies, two tubes adjacent to the already suggested track are turned 'on' in one of those layers which contain no discharged tubes, in turn, and a track fit is attempted. The other options refer to combinations of knock-ons and inefficiencies.

When an option produces several possible fits, then the first five found are stored and the correct one selected in the next stage of the analysis when the angle criterion is applied. Only the first five are stored because of lack of available core space but, as only about 1% of trays analysed ever contain more than five possible tracks, the majority of the data are unaffected. It is also highly probable that the correct track is amongst the five.

3.6.4 The Angle Criterion

A parabola is fitted to the co-ordinates of the tracks in those trays which were not classed originally as unusable and which did not contain a burst. The angle of the trajectory in a tray is found by taking the differential of the parabola at that tray. Lines are then drawn at this angle through the tube configuration (either the initial configuration or that chosen by the options) and a check is made, for each line, to see if any information is violated. The lines which are drawn are $^1/80^{th.}$ of a tube spacing apart and they begin $^1/4$ of

Table 3.1

The Track Fitting Options

Option	Description
0	Good fit - no information has to be assumed.
1	A knock-on electron is assumed (a discharged tube is neglected).
2	A tube inefficiency is assumed (an undischarged tube is assumed to have discharged).
3	A knock-on electron and a tube inefficiency in different layers are assumed.
4	Two knock-on electrons in different layers are assumed.
5	Two inefficiencies in different layers are assumed.
6	One single knock-on and one double knock-on are assumed in different layers.
7	A tube inefficiency and a knock-on in the same layer are assumed.
8	Two knock-ons in the same layer are assumed (muon passed between them).
9	Two knock-ons in the same layer are assumed (muon passed to one side of them).
10	An inefficiency and a double knock-on are assumed in the same layer.
11	Assumes an inefficient tube between two knock-ons.
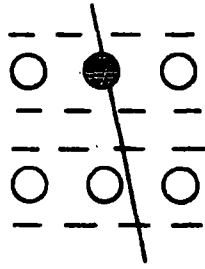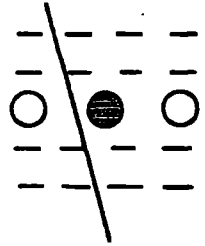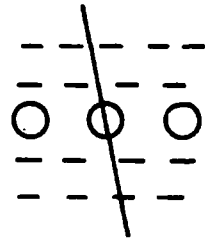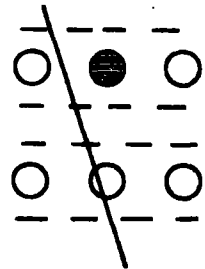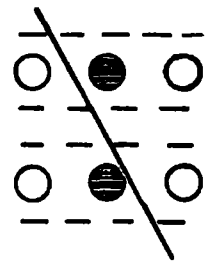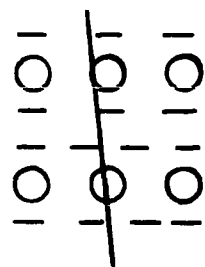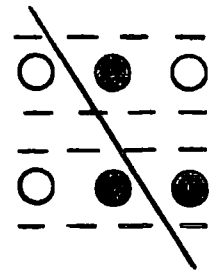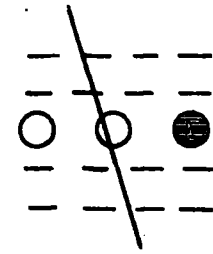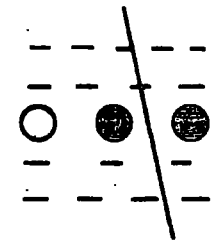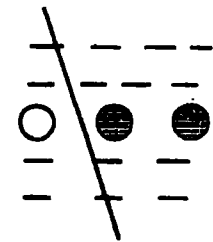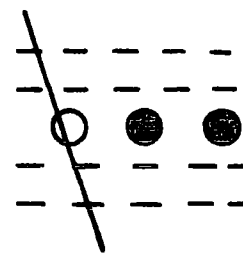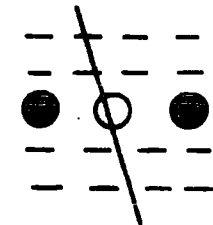
Figure 3.6 Illustration of Track Fitting Options.

a tube spacing on one side of the initial co-ordinate and finish $^1/4$ of a tube spacing on the other side. A total of 41 lines are drawn. A typical channel is illustrated in figure 3.7.

If some of these lines do not violate any information, then they define a region of the tray through which the muon could have passed and the centre of this region, at the middle of the tray, is taken as the final co-ordinate of the muon in that tray. If several configurations of tubes were possible then they are all examined with the angle criterion to determine which one is correct. If none of the configurations contain a track at the correct angle then other track fitting options are tried and the angle criterion reapplied until a successful combination is obtained.

3.7 The Determination of the Muon's Momentum and the Zenith and Azimuthal Angles

3.7.1 The Momentum of the Muon

It was shown in section 2.2.1 that the trajectory of a charged particle moving in a magnetic field describes the arc of a circle. Figure 3.8 shows such a trajectory and its equation of motions can be written as

$$(x - p)^2 + (y - q)^2 = r^2$$

where (p,q) is the centre of the circle, whose radius is r

$$\text{Hence} \quad y = q \pm r \sqrt{\left(1 - \left(\frac{x - p}{r}\right)^2\right)} \tag{3.1}$$

In the co-ordinate frame of the spectrograph shown in figure 3.9, $p \sim r\sin\theta$, $q \sim r\cos\theta$ where θ is the zenith angle, and for a 100 GeV/c muon, the radius of curvative r, from equation 2.1, is 204m. The zenith angle has a maximum value of $\sim 7^o$ and because $x \sim 3$m, the term $(x - p)^2/r^2$ has a value of 0.02. Hence equation 3.1 can be expanded binomially, higher order terms being neglected to give

$$y = \frac{1}{2r} \cdot x^2 - \frac{p}{r} x + \left(q - r + \frac{p^2}{2r}\right) \tag{3.2}$$

The negative sign of the square root has been taken because $y \sim 0$ in the reference frame.

a a'-Limits of Scan
b b'-Channel Width

0.5 cms

0.5 cms
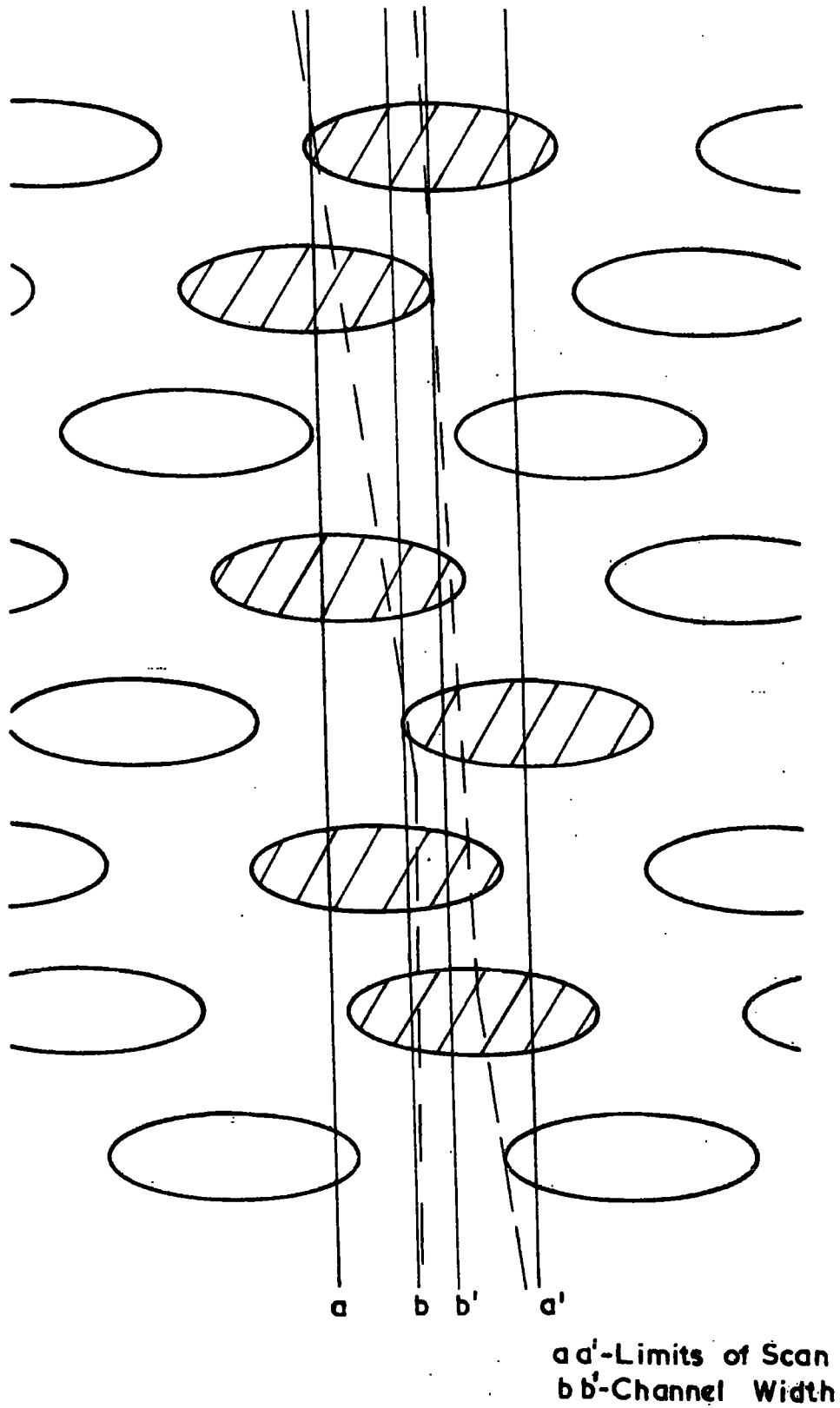
Figure 3.7   A Typical Channel Defined with the Angle Criterion.
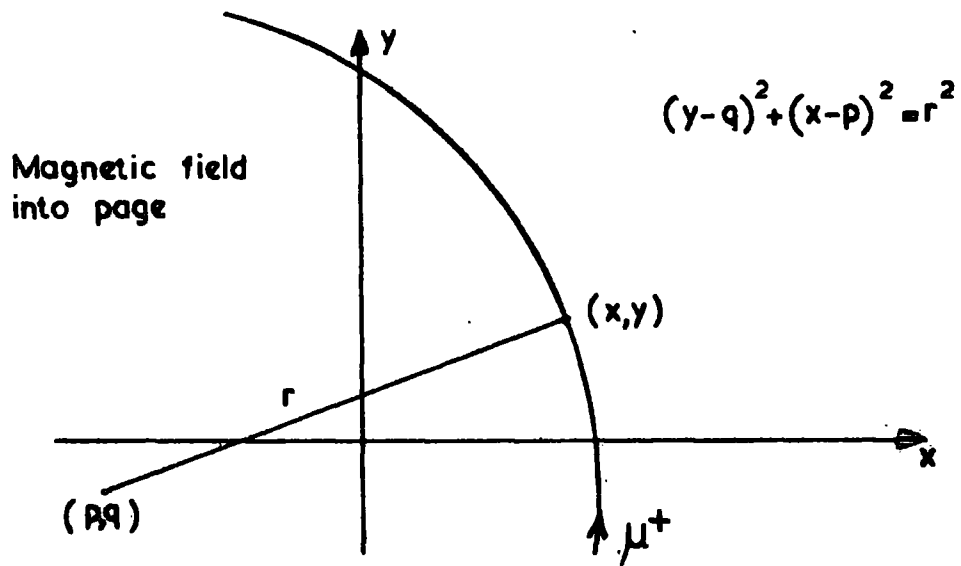
Figure 3.8 The Trajectory of a Muon in a Magnetic Field.
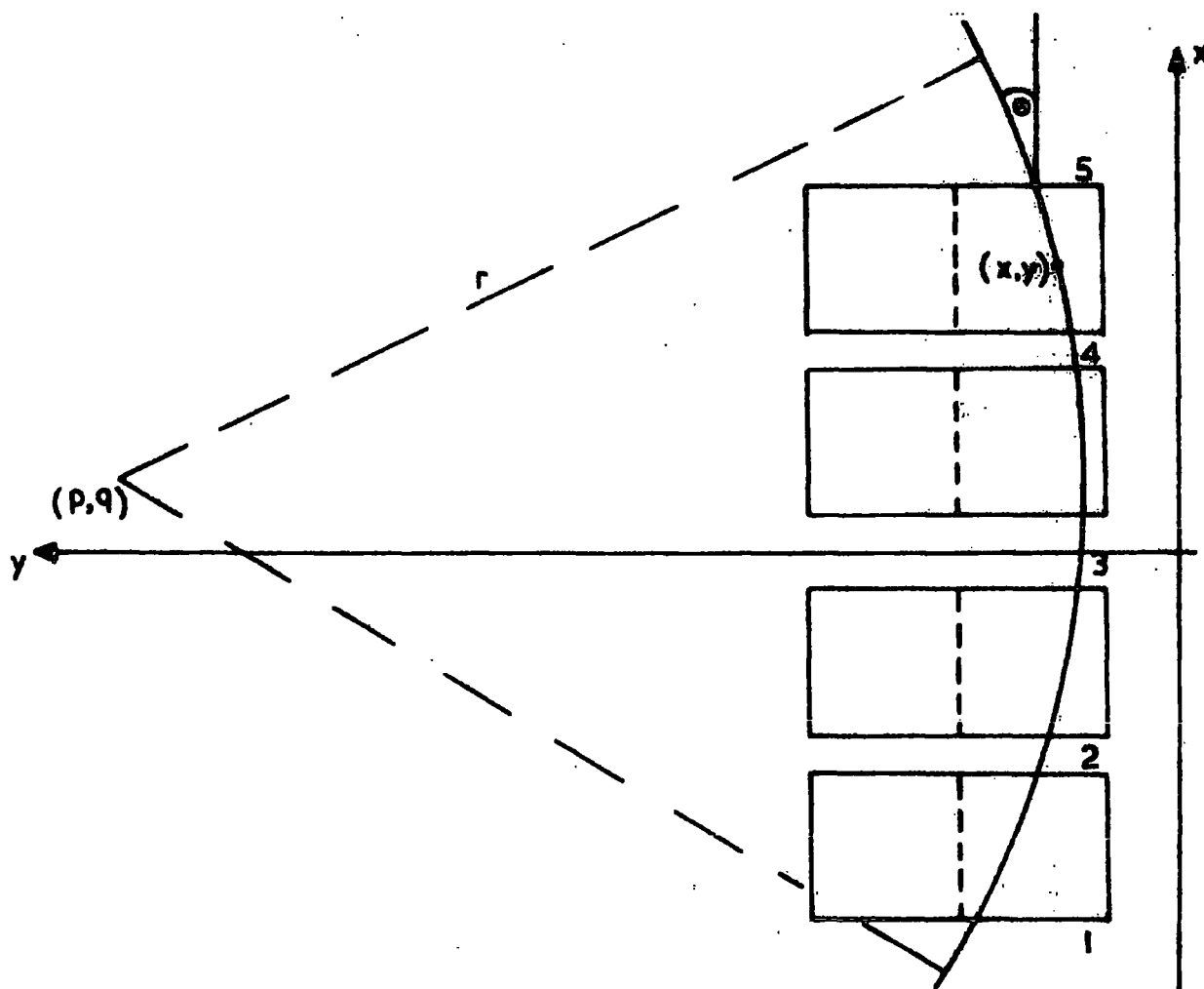
Figure 3.9 The Co-ordinate Frame of the Spectrograph.

It can be seen that this can be written in the form $y = ax^2 + bx + c$ and

the latter is the general equation of a parabola. If such an equation is fitted

to the co-ordinates of the trajectory of the muon, the radius of curvature of

the trajectory (and hence the muon's momentum) may be extracted from the

coefficient of the x^2 term. From equations 2.1 and 3.2 the momentum of the

muon, P_μ, can be defined in terms of the parabola coefficient, a, as

$P_\mu = Be/2a$, or, substituting the characteristics of MARS

$$P_\mu = \frac{0.2445}{a} \text{ GeV/c} \qquad (3.3)$$

It is shown in section 5.6 that, to allow for the effects on the derived

momentum of the gaps between the magnet blocks, a correction factor of 0.7972

must be introduced into the above equation. Hence

$$P_\mu = \frac{0.1949}{a} \text{ GeV/c} \qquad (3.4)$$

and this is the equation that the programme uses to calculate the momentum of

the muons. The accuracy of equation 3.4 is discussed in Chapter 5.

3.7.2 The Theory of the Parabola Fitting

The parabola fit was found by the method of 'least squares', where the

standard deviation of the points around the fitted curve is minimised. For the

equation $y = ax^2 + bx + c$, the sum of the standard deviations, S, of the points

around the curve is defined as

$$S = \left(\sum_{n=1}^{m} (y_n - ax_n^2 - bx_n - c)^2 \right)^{1/2}$$

For S to be a minimum the following conditions must be satisfied

$$\frac{\partial S}{\partial a} = \frac{\partial S}{\partial b} = \frac{\partial S}{\partial c} = 0$$

and hence the following equations must also be satisfied

$$a \Sigma x^4 + b \Sigma x^3 + c \Sigma x^2 - \Sigma yx^2 = 0$$

$$a \Sigma x^3 + b \Sigma x^2 + c \Sigma x - \Sigma yx = 0$$

$$a \Sigma x^2 + b \Sigma x + c \Sigma 1 - \Sigma y = 0$$

The coefficients of the parabola fit are found by solving these three linear equations for a, b and c.

3.7.3 The Zenith Angle of the Muon

The programme calculates the projection of the angle of the muon's trajectory, at level 5, on the measuring plane and this angle is termed the zenith angle. This angle, ψ , is defined as the gradient of the parabola at level 5 and this is given by

$$\psi = 2a.x_5 + b \tag{3.5}$$

The angle, so defined, is the tangent of the required angle but because it is usually less than 7° for the higher momenta muons, the angle is accurate to better than 0.6%

3.7.4 The Azimuthal Angle

The azimuthal angle, which is again the projected azimuthal angle, is defined by the flash-tube trays across the top of the spectrograph. As described in section 3.4.3, no actual fitting of a trajectory is attempted through the discharged tubes but only the mean point of the discharged tubes in each tray is taken. A line between the two trays is so defined and the inclination of this line to the vertical is taken to be the azimuthal angle. The quantity defined is the tangent of the required angle and because this angle may take values up to 15.5° account must be taken of this approximation in later calculations. The accuracy attainable by this method of measuring the azimuthal angle is discussed in Chapter 5.

3.7.5 Energy Loss

Energy is lost by the muons, at a rate of about 1.4 GeV/m of iron, as they traverse the spectrograph. Consequently, their trajectories are not circular but are helices. No allowance is made by the programme for this energy loss because the majority of events should have a momentum greater than 200 GeV/c and the energy lost by these muons amounts to $\leqslant 5\%$ of their total energy; an amount for which a correction can be easily made. Values for the correction factors are given, with details of their derivation, in section 5.6.

3.7.6. The True Momentum and the True Zenith and Azimuthal Angles

Only the projected momentum and angles are measured with MARS but with a knowledge of all three projected values the true values may be calculated. Consider figure 3.10. The plane XZ represents the measuring plane for the momentum and the zenith angle and the plane YZ the measuring plane for the azimuthal angle. If P_o, Z_o and α_o are the measured momentum, zenith and azimuthal angles and P_T, Z_T and α_T are their true values then

$$AH = P_T \cos Z_T = P_o \cos Z_o \qquad\qquad (a)$$

$$AB = P_T \cos Z_T \tan Z_o = P_T \sin Z_T \sin \alpha_T \qquad\qquad (b)$$

$$AC = P_T \cos Z_T \tan \alpha_o = P_T \sin Z_T \cos \alpha_T \qquad\qquad (c)$$

from equations (b) and (c) $\tan \alpha_T = \tan Z_o \cot \alpha_o$ and $\tan^2 Z_T = \tan^2 Z_o + \tan^2 \alpha_o$ hence substituting Z_T in equation (a) we obtain, for the three true values

$$
\begin{aligned}
P_T &= P_o \cos Z_o \left[1 + \tan^2 Z_o + \tan^2 \alpha_o \right]^{\frac{1}{2}} \\
Z_T &= \tan^{-1} \left[\tan^2 Z_o + \tan^2 \alpha_o \right]^{\frac{1}{2}} \\
\alpha_T &= \tan^{-1} \left[\tan Z_o \cot \alpha_o \right]
\end{aligned}
\qquad\qquad (3.6)
$$

It should be noted that the values of the projected zenith and azimuthal angles calculated by the programme are, in fact, the tangents of the respective angles and they can be substituted directly into equations 3.6. If $\alpha = \tan \alpha_o$ and $Z = \tan Z_o$, i.e. α and Z are the values given by the programme, then

$$
\begin{aligned}
P_T &= P_o \left(\frac{1 + Z^2 + \alpha^2}{1 + Z^2} \right)^{\frac{1}{2}} \\
Z_T &= \tan^{-1} (Z^2 + \alpha^2)^{\frac{1}{2}} \\
\alpha_T &= \tan^{-1} (Z/\alpha)
\end{aligned}
\qquad\qquad (3.7)
$$

Hence, the true momenta, zenith and azimuthal angles may be found from the values of their projections on the measuring planes calculated by the programme with equations (3.7).

	Measured Value	True Value
Momentum	$P_O = BH$	$P_T = DH$
Zenith	$Z_O = <AHB$	$Z_T = <AHD$
Azimuth	$\alpha_O = <AHC$	$\alpha_T = <GHF$
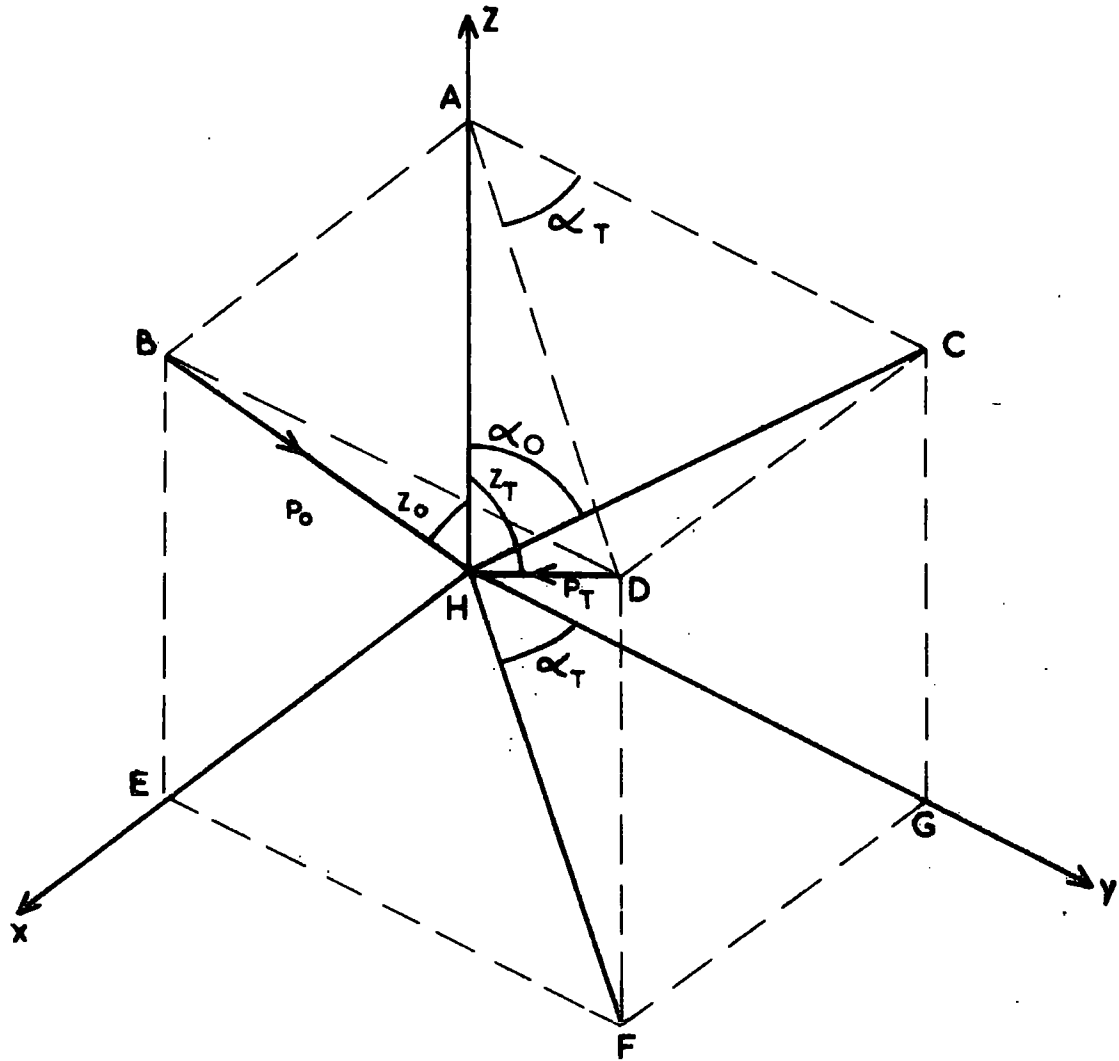
Figure 3.10 The Relationship between the True and the
Measured Momentum Zenith Angle and
Azimuthal Angle.

CHAPTER 4

The Data Analysis Programme

4.1 Introduction

A complete description of the analysis programme is given in this chapter, together with logic flow charts and explanatory notes. The name given to the programme, which is executed to initiallise data analysis, is MARS1 but this is not the programme which performs the actual analysis. MARS1 only prepares the computer for data analysis by loading data and various spectrograph co-ordinates into a special area of core (a common area). A link is then performed to the analysis programme whose name is CHURN.

The programme which is used to locate the measuring trays with the data from a zero magnetic field run is also described. Programme execution is initialised as above except that the respective programme names are MARSZ and ZCHRN.

In order that the analysis programme can be understood, it is first necessary to consider how the programme handles multi-particle events, bursts and air showers.

4.2 The Handling of Multi-tracks, Bursts and Air Showers

The programme, in determining the type of event, divides the discharged tubes in a tray into groups of columns, as defined in section 3.4.2. It is demanded that each tray contains at least one group, otherwise the event is declared void. This feature assists in the removal of spurious events such as those due to air showers.

Any tray which contains more than two groups is declared unusable and the tray is omitted from any of the trajectory fitting procedures. This reduces the number of calculations and the core storage requirements, and it occurs when the muon is accompanied through a tray by two or more well separated particles which originated in an air shower or interaction of the muon.

The remaining multi-track events fall into two categories:

1) where all the usable trays contain two groups and

2) where only some trays contain two groups, the others one.

The two categories of events are handled differently by the programme.

When all the trays contain two groups, it is assumed that the spectrograph was traversed by two muons. In addition, it is assumed that the two trajectories do not cross and that the set of first groups contains the trajectory of one muon and the second set, the other. Consequently, the analysis of such an event is restricted to the set of first and to the set of second groups separately and cross combinations are never considered. Any event which consists of a pair of muons with crossed trajectories will not be analysed correctly and will certainly fail the fitting criteria. It is considered that this will not constitute a severe loss of particles because, of all the muons observed photographically (10,000, details of which are given in Chapter 6) no muon pairs were observed which were totally contained within the acceptance of the spectrograph. For those events in which it was possible to trace the trajectories of a pair of muons through at least two levels of the spectrograph, all the trajectories were well separated and none crossed. The approach to the analysis is further justified by the fact that muon pairs, each with momenta in excess of 100 GeV/c, will certainly have originated high in the atmosphere and their trajectories will be essentially parallel. If their trajectories are separated sufficiently to enable each tray to be divided into two groups, then there is insufficient curvature on their trajectories to enable them to cross.

For those events where some trays contain two groups and the others only one, the programme has to decide which combination of the groups forms the trajectory. To simplify the procedure and to minimise the number of calculations and core storage requirements, it is assumed that, for those trays with two groups, the trajectory lies within either the set of first groups or the set

of second groups. Each of these sets is then combined with the trays containing only one group and the programme ascertains, using certain criteria, which group combination forms the trajectory. Normally, only one group combination satisfies the fitting criteria but, if both do, then the trajectory which has the smallest standard deviation of its co-ordinates around the fitted parabola is selected.

A group which contains a burst is omitted from any precise trajectory location procedures. However, if there is another group in that tray which does not contain a burst, this group will be used for trajectory location purposes but only under the group combinations described above. At a later stage in the calculations a check is made to see if the bursts, in the selected group combination, lie within 1.0cm of the fitted trajectory. This distance was calculated by scattering 100 GeV/c muons through the spectograph, with $<\theta_s>/\theta_m$ = 0.12, and finding the distribution of the distance of the co-ordinate in any one measuring tray to a parabola fitted to the other four co-ordinates. The distance used is three times the standard deviation of these distributions.

4.3. Summary of the Handling of Multi-track Events

The group configurations, including bursts and air showers, which are correctly handled by the programme are shown in figure 4.1 and those which are unsuccessfully handled are shown in figure 4.2. Of the latter, the only two configurations which fail because of an incorrect interpretation of the data (rather than because of a lack of useful information) are 4.2(a) and (d). Configuration 4.2(a) has been discussed and does not constitute a serious loss of particles. Configuration 4.2(d), where side tracks at two levels on opposite sides of the muons trajectory do not permit a correct interpretation of the data, will (after Said, 1966) constitute 6.0% of the data at a momentum of 1000 GeV/c and will therefore cause a small loss of muons at high momenta. The programme will, however, attempt to produce answers from these two configurations by omitting those trays it considers to be offending. This procedure is described in the next section.
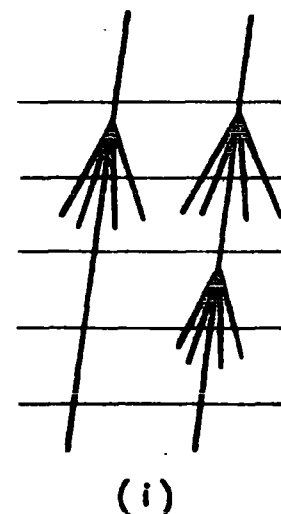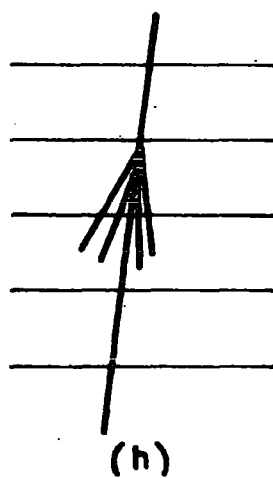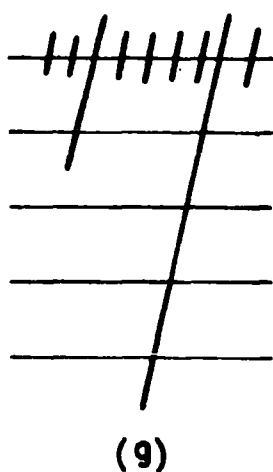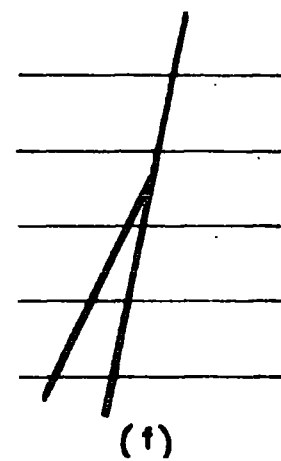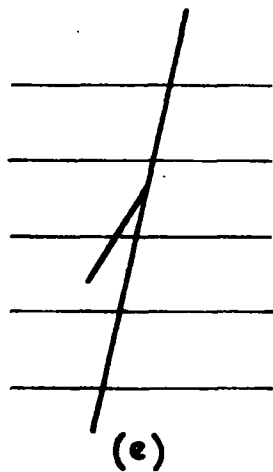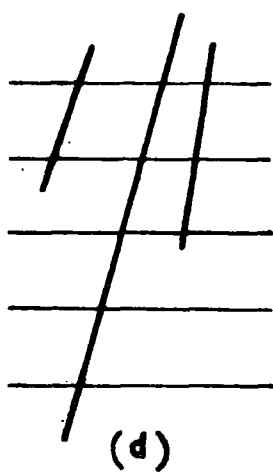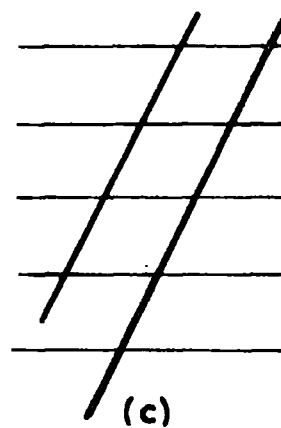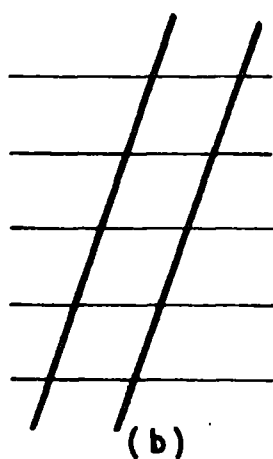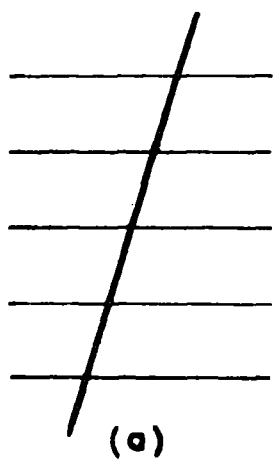
Figure 4.1 The Group Configurations which are Successfully Handled by the Analysis Programme.
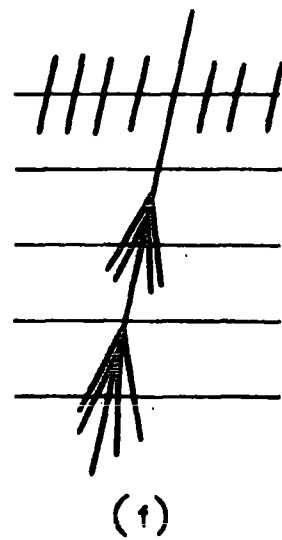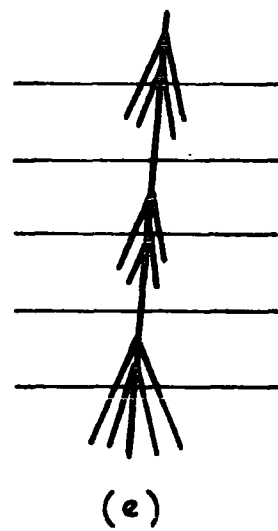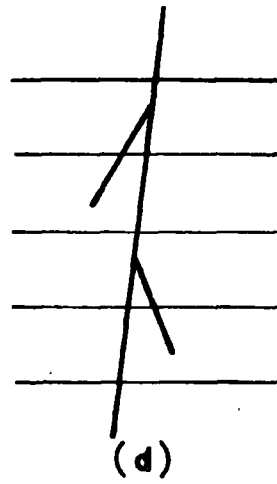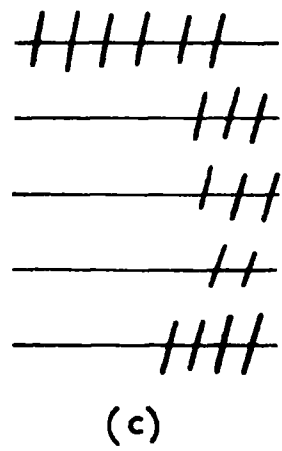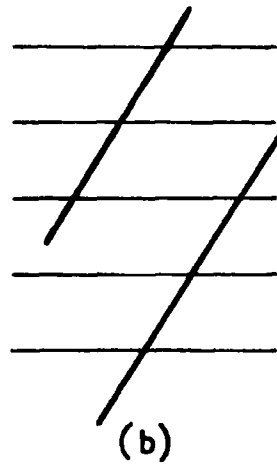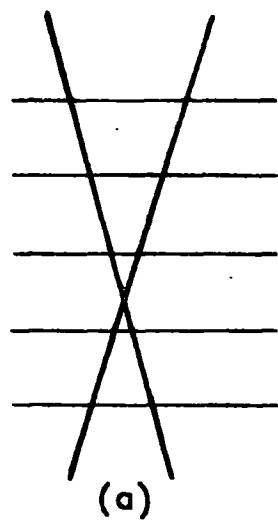
Figure 4.2 The Group Configurations which are Unsuccessfully Handled by the Analysis Programme.

4.4. Event and Tray Rejection

Apart from the demands made previously on the data, i.e. that every tray must contain at least one group with at least three layers containing discharged tubes, there are other reasons for event rejection. A syntax error in the data will terminate the event and similarly, if there are less than three usable trays with which to define the trajectory of the muon, termination will occur. (A minimum of three points is required to define a parabola).

An outline of the analysis technique was given in section 3.6.2 and it can be seen that the tube patterns are investigated twice; once to define an approximate co-ordinate and then to find a more refined co-ordinate using the angle criterion. If, on the first investigation, the programme is unable to place a track through the flash-tube configuration of one tray, then the analysis of the event is terminated. This is because the programme is unable to interpret the data even when all the fitting options are tried and so the event is rejected. If a track cannot be placed through the tube configuration at the required angle, then only the tray is rejected. The analysis of these events is continued and other trays rejected as necessary, until either an answer is obtained or analysis terminated because of a lack of remaining co-ordinates.

4.5. The Input File

The events are packed together on the disc as they are collected and consequently some events overlap sector boundaries. It is advantageous to have the entire event in core during its analysis and therefore, it is necessary to have a buffer in core 640 words long to hold the two sectors of data which contain the event.

The answers to the analysis are stored back amongst the data and so the data on the disc are overwritten with the same data and their embedded answers. The analysis programme works through the buffer in the core and, when the end is reached, the first 320 words are written back onto the disc in the sector from where they came. The second 320 words of the buffer are then transferred to the first 320 words of the buffer and the next sector of data is read into the second 320 words.

Table 4.2

The Error and Warning Codes Flagged by the Programme

E1   No track in a group or event.

E2   Tray missing or trays out of order.

E3   No data for a tray.

E4   Trigger mode undefined.

E5   No discharged tubes in a column.

E6   Less than seven trays present.

E7   A tray identifier missing.

E8   No data for event (i.e. header only).

E9   The event cannot be contained in core.

E10   Erroneous zeros in data.

E11   No dummy columns in a tray.

E12   Less than three usable measuring trays.

E13   Unusable trays and bursts in first set of groups exceeds two.

E14   Unusable trays and bursts in second set of groups exceeds two.

E15   Two muons but first did not satisfy fitting criteria.

E16   Two muons but second did not satisfy fitting criteria.

E17   Other groups present but too many unusable.

E18   Magnetic field direction undefined.

E19   Tray deemed unusable as more than two groups present.

An example of a sector of data before analysis is given in table 4.1. The data are in hexadecimal format, one character representing four binary bits. The binary equivalents of the characters are given in Appendix B. The sector contains nearly 5 events and the event header and the individual trays of the first event completely contained in the sector are depicted. An explanation of the contents of the header and of the format of the tray data are to be found in Appendix B.

4.6. The Scanning of the Data

4.6.1. Introduction

Before the analysis can proceed for any event, it is necessary to scan the data for that event and define the quantity of data for each tray and the positions of the various flags, such as tray headers and dummy columns. The consistency of the data is also examined during scanning and errors are generated if any faults with the data are detected. A complete list of the generated errors is given in Table 4.2. Errors E1 - E11 and E18 are produced during scanning and all of them except E6 and E18 terminate the analysis of the event. All of the errors are placed in the output file and when possible back amongst the data.

The subroutine which is responsible for this scanning of the data is known as SIFT. A diagram of the logic flow of this programme is shown in figure 4.3 and it is described in the following sections. The numbers in parentheses in the text refer to the numbered stages of the logic flow diagram.

4.6.2. Defining an Event

The beginning of an event is defined by the event header and the end of an event by the header of the next event. The first and ninth words of a header are always zero and they are used to identify the header. The only other place zeros can occur in the data is within the header, never in the data for the trays.

As each event is found, the core address of the beginning of the next event is stored and this serves as the continuation point at which to start

Figure 4.3   The Flow Chart of the
Programme which Scans the Data
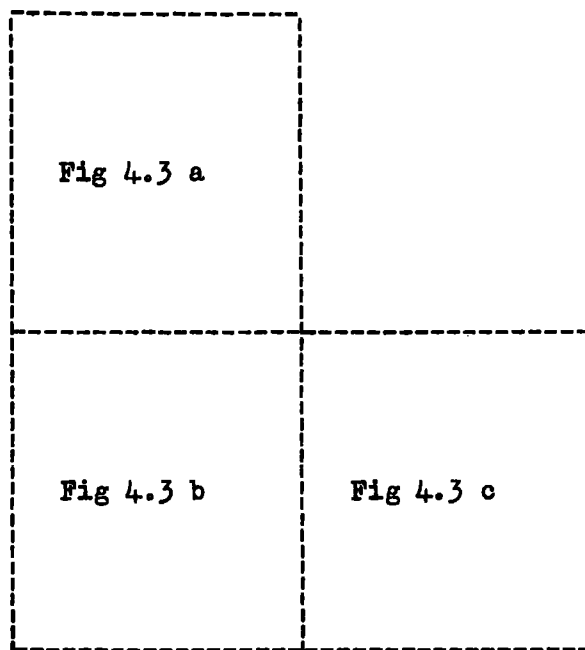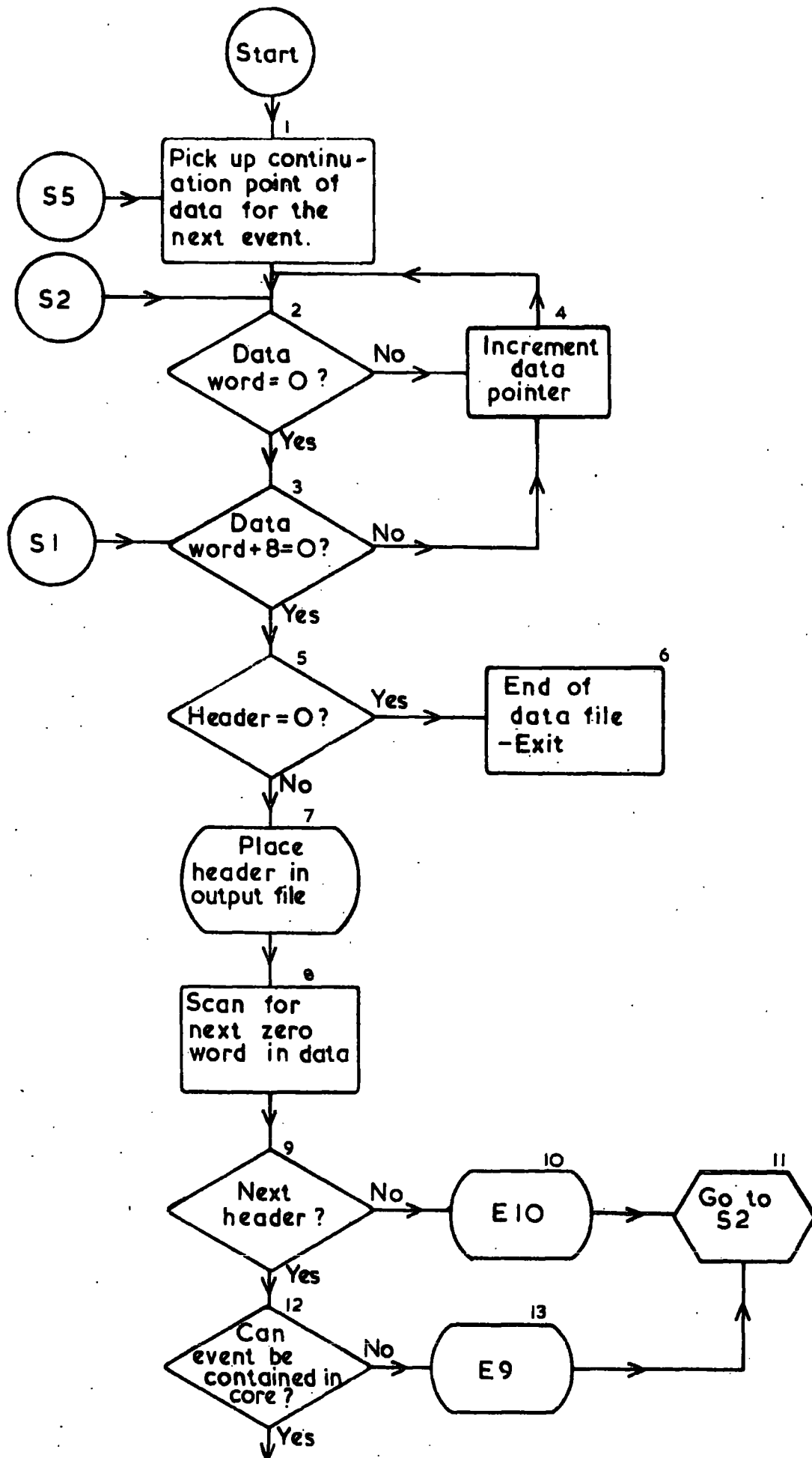
Figure 4.3a
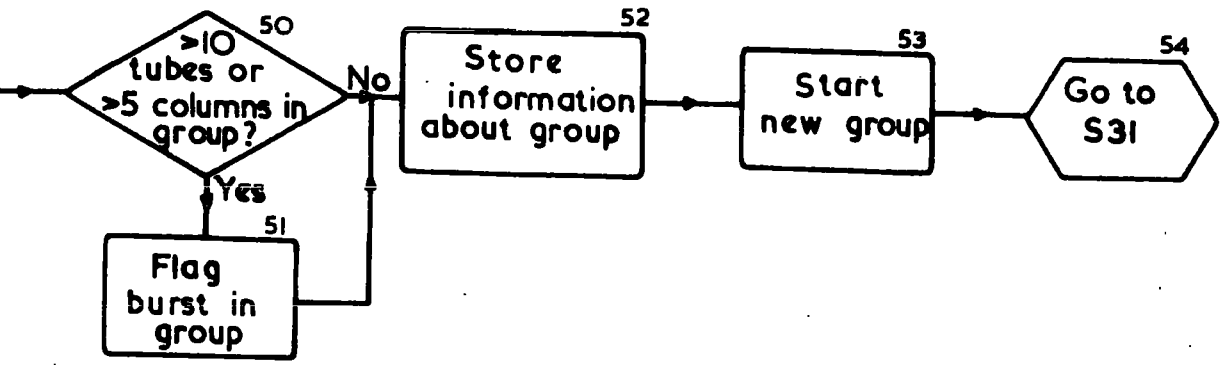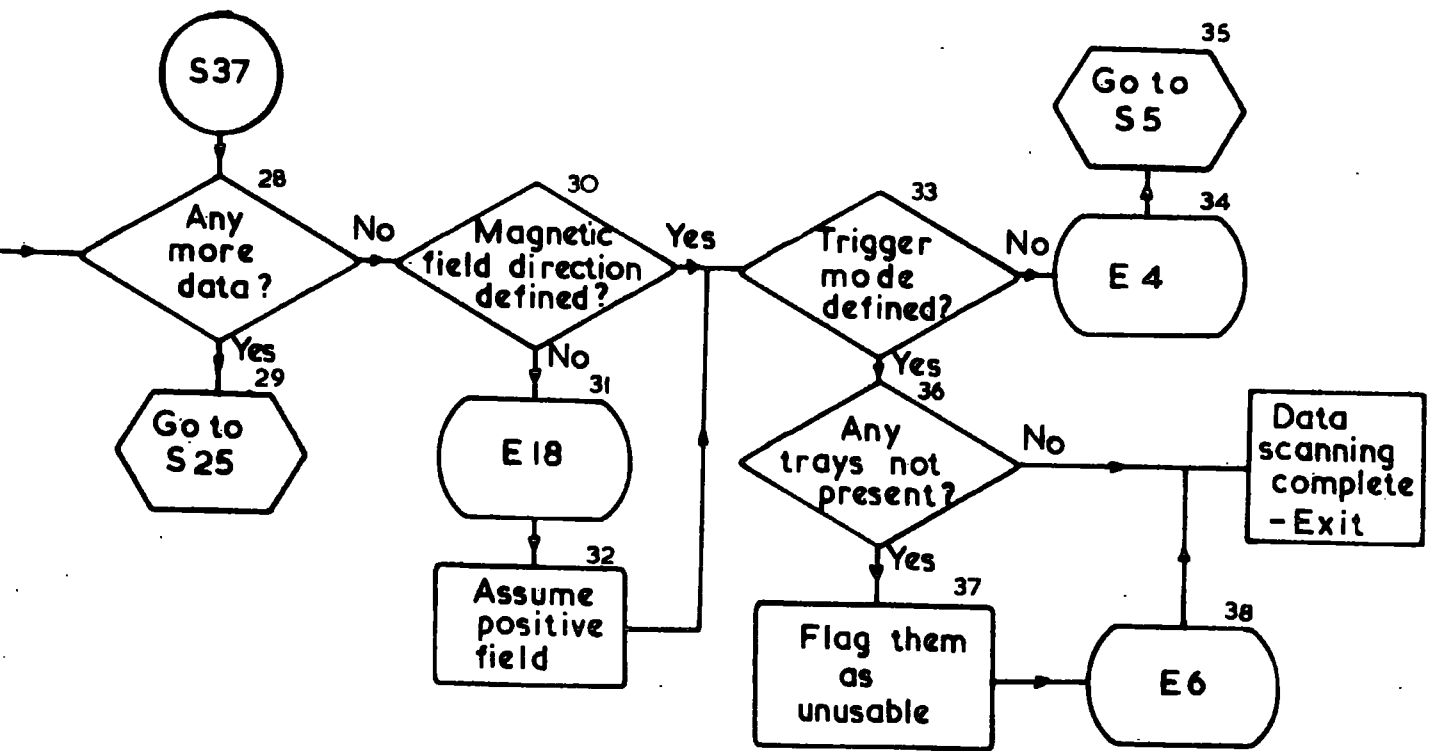
Figure 4.3c

scanning the next event[1]. (For the first event, the continuation point is the beginning of the data buffer).

The data are scanned for a word which contains zero[2] and when found, the eighth word after it is examined to see if the two together form a header[3]. If this is not the case, then scanning is continued until a header is found[4]. The contents of the header are then examined to see if it is entirely composed of zeros[5], in which case the end of the data file has been reached and the analysis of the data is terminated[6]. The contents of the header are placed in the output file[7] so that any error codes and the answers to the analysis may be associated with the header (which includes an event number). A complete description of the header is to be found in Appendix B.

The next zero word is then found in the data[8] and a check is made to see if this also belongs to an event header[9]. If it does then the end of the data for the event has been found, if it does not, then an erroneous zero has been found amongst the data indicating that the data is unreliable. Error E10 is generated and the analysis of that event is terminated[10,11].

If at any time during the scanning the end of the data buffer is reached, new data is brought into core and the old returned to the disc, as described in section 4.5. This is only allowed to occur once whilst the length of one event is being determined, otherwise it means that the data for that event stretch over three sectors and cannot be contained in core[12]. An event with this quantity of data must have at least 264 columns containing discharged tubes. It is improbable that the data for such an event could be interpreted because they were probably the result of an extensive air shower. Error E9 is generated and analysis continues with the next event[13,11].

4.6.3. The Scanning of the Trays

The data for the event are then divided into the respective flash-tube trays. If there are no data for the event (only an event header), error E8 is generated and analysis continues with the next event[14-16]. The first data

word of each tray (as described in Appendix B) is the tray header. The left hand 8 bits of this word are all set at logical '1' and the right hand eight bits contain the tray number in binary. If a tray header is not found immediately following the event header or the data for the previous tray, error E7 is produced[17-19]. The trays should follow each other in logical order and, if this is not found to be the case, then error E2 is generated[20,21]. The analysis of the event is terminated in both cases[16].

The data for the tray are then scanned until column 91 is found[22,23], which is the beginning of the dummy columns. The positions of these dummy columns amongst the data are stored for later use[27]. Error E11 is generated if the dummy columns are not present and the event is terminated[39-41]. A check is made at this stage on each data word to ensure that they each contain at least one discharged tube. Error E5 is generated if they do not and analysis terminated[55-57]. The data are also divided into groups[42,43], bursts being flagged as necessary[50,51], and spurious tubes ignored[44,46]. It should be noted that it is not demanded of the azimuthal trays (trays 6 and 7) that a group must contain at least three layers of discharged tubes because of the low tube density from these trays with only 4 layers of tubes[44,45].

Once column 91 has been found, a count of the number of groups in the tray is made[24]. The tray is flagged as unusable if there are more than two groups[27]. Error E3 is generated if there are no groups and the event is terminated[24-26]. Information as to the position of the groups within the data and also the lengths of the groups are stored for later use[27].

The above processes continue until all the trays have been scanned and the end of the data for the event is reached[28,29].

4.6.4 Completion of the Scanning

The direction of the magnetic field and the trigger mode of the spectrograph are extracted from the event header[30,33]. Errors E18 and E4, respectively, are generated if these quantities are undefined[31,34]. A positive magnetic

field direction is assumed if the field direction is undefined[32] but an undefined trigger mode terminates the event[35].

Error E6 is generated if any of the trays are not present and these trays are flagged as unusable[37,38]. This will occur when there is a large amount of data for the first few trays and the later trays could not be contained in the core store. The analysis of these events is continued if there are sufficient trays present to do so.

The scanning of the data is now complete and the data are ready for analysis.

4.7 The Analysis of the Data

4.7.1 Introduction

The analysis programme is necessarily rather complex and a diagram of the logic flow is given in figure 4.4. Once again, the numbers in parentheses in the text refer to the numbered stages of the logic flow diagram. It is essential, if the programme is to be understood, that the manner in which the programme handles multi-track events and tray failure, as described in earlier sections, be born in mind whilst following the programme.

The term 'group combination' is used to describe any combinations of the groups in the trays permissable under the group handling scheme, described in section 4.2. The termination of an event is always by way of the portion of the programme[70-73] described in section 4.7.7, except that the answers are only stored and the azimuthal trays analysed when it is possible to do so.

4.7.2 Special Features of the Programme

It will be seen from the flow chart (figure 4.4) that the first decision made by the programme is 'Is termination required?'[1]. Whilst the programme is running, at least one of the console entry switches of the computer must be 'on' otherwise, if they are all 'off', the programme terminates (including data storage) at the completion of the analysis of the event being processed.

Figure 4.4 The Flow Chart of the
Data Analysis Programme

```
+----------------------+----------------------+
|                      |                      |
|                      |                      |
|                      |                      |
|     Fig 4.4 a        |     Fig 4.4 b        |
|                      |                      |
|                      |                      |
|                      |                      |
+----------------------+----------------------+
|                      |                      |
|                      |                      |
|                      |                      |
|     Fig 4.4 c        |     Fig 4.4 d        |
|                      |                      |
|                      |                      |
|                      |                      |
+----------------------+----------------------+
```
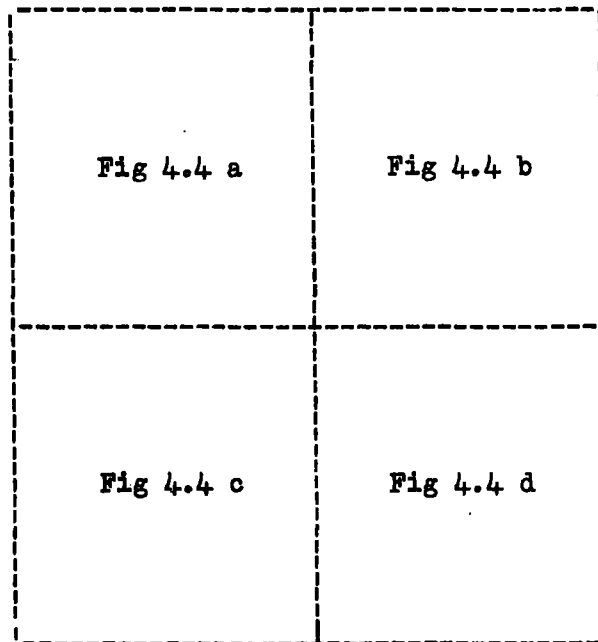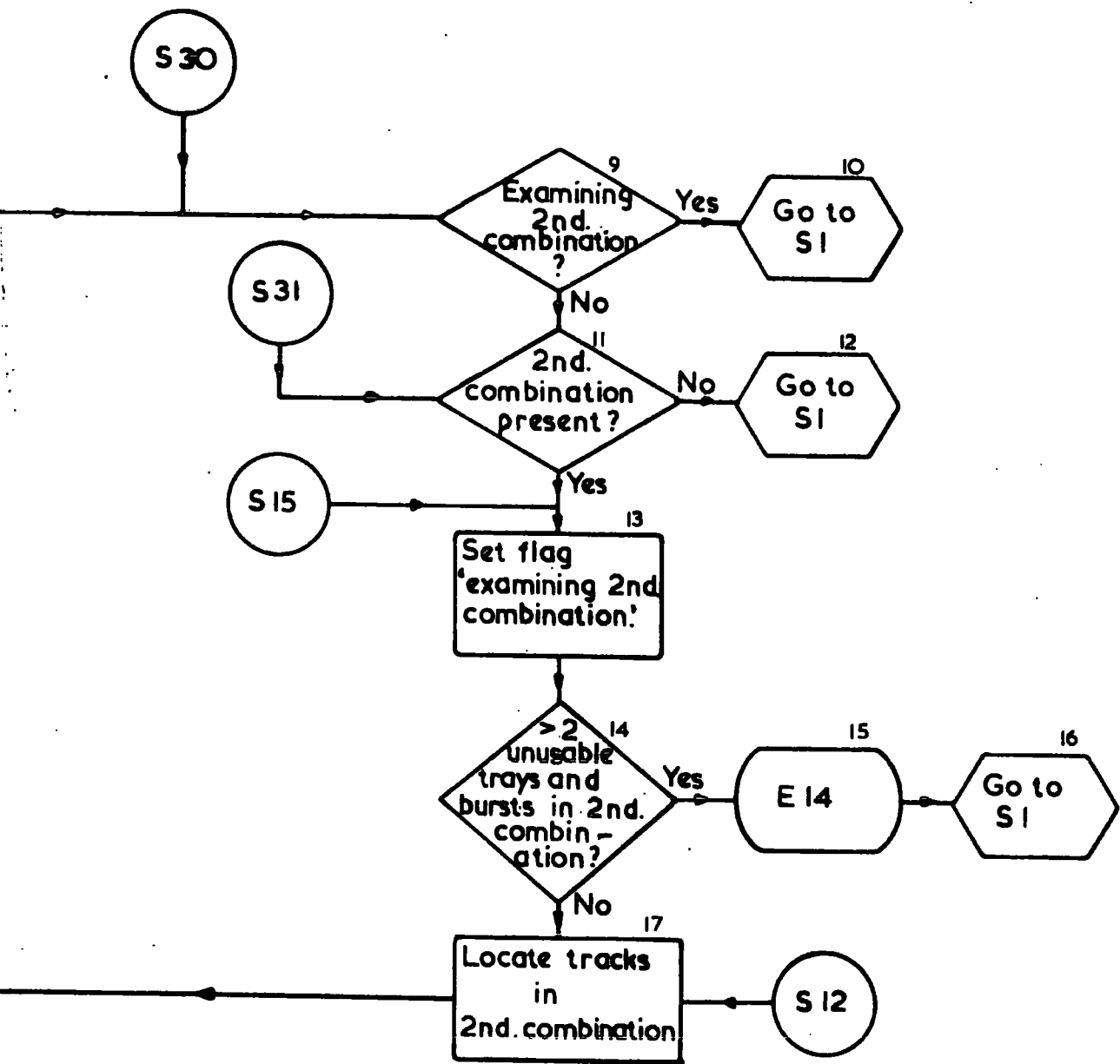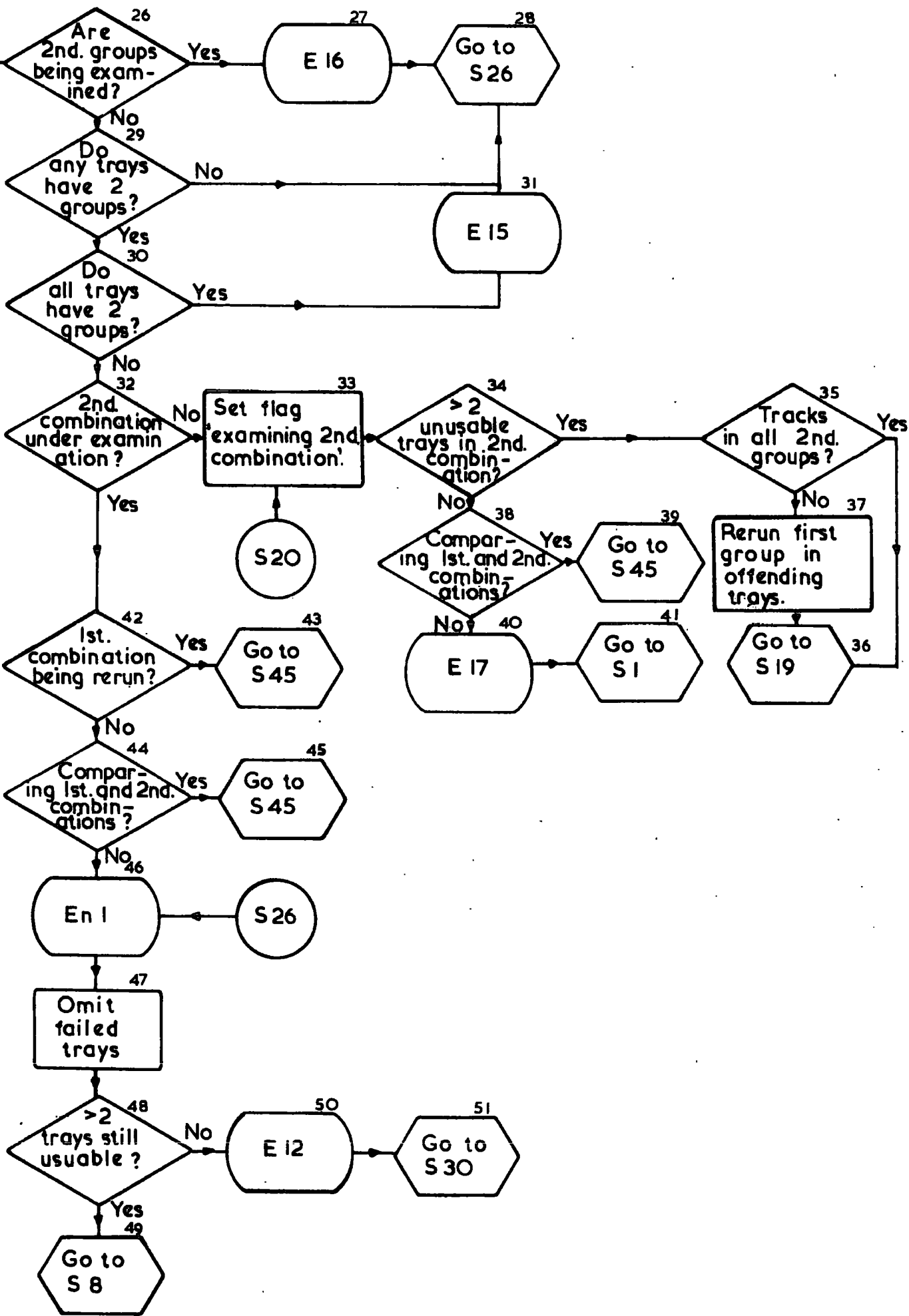
Figure 4.4b

Figure 4.4d

Another feature of the programme is that counts are kept of the number of events which are successfully and unsuccessfully analysed. These may be placed, for examination in the display panel of the computer by turning 'on' console entry switches 1 or 2 respectively, and depressing the 'INT. REQ.' (interrupt request) button on the computer console. Depressing 'Programme Start' continues the data analysis. This feature enables the progress of the analysis to be monitored.

The storing of data from MARS whilst data analysis is in progress, is accomplished by a special subroutine which is loaded into core with the analysis programme. Interrupts from MARS are trapped by this subroutine and consequently data storage is unseen by the analysis programme. The only linkage between the two programmes is an initial call from the analysis programme to the subroutine to facilitate the loading of the subroutine into core.

4.7.3 Selection of the Event and the Group Combination

The data are first scanned by the programme described in section 4.6 and control is returned to the analysis programme when an event has been found which is suitable for analysis[3].

At least three trays are required by the programme to fit a parabola and a count is made of the number of unusable trays[4]. If this is greater than two, then error E12 is generated and the analysis of the event terminated[5,6].

The first group combination is studied and a count is made of the number of unusable trays, including bursts[7]. Analysis continues if there are at least three usable trays otherwise error code E13 is generated[8]. In the latter case, a check is made to see whether another group combination exists which has not been examined and analysis continues with this combination if possible[9-13,17]. Error E14 is produced if there are insufficient usable trays in the second combination[14-16].

4.7.4 The Fitting of the Trajectory

All of the usable trays in the group combination are examined and a track located in each of them using the track fitting technique described in Chapter 3[18]. A group is first divided into subgroups. These consist of three columns, or less, of data and they limit the angular search for tracks (which do not spread across more than three columns). They also help to separate close side tracks from the muon's track. A group consisting of five data columns will be divided up into three subgroups, each of three columns. The first subgroup will contain the first three columns of the group; the second, the middle three columns; and the third, the last three columns of the group. A group with four columns will be divided up into two subgroups and one with three columns or less into one subgroup only. Each subgroup is examined in turn and the subgroup which contains the track with the most probable tray option fit is selected. A record is kept of all subgroups which contain tracks[18].

When the programme is unable to place a track anywhere within a group and the first group combination is under examination, then the programme examines the second group in that tray[18]. If there is not a second group present or the second group fails as well, error code En1 (where n is the tray number) is generated and the event terminated[19,20]. This error is automatically generated if the second group configuration is under examination and a tray fails at this stage of the analysis[19,20].

A parabola is fitted to the co-ordinates of the tracks in the flash-tube trays. When there is more than one possible track in a subgroup, the mean point of their co-ordinates is taken[21]. The gradient of the parabola at the various measuring levels of the spectrograph is then used to define the angle of the trajectory in each tray and a more refined co-ordinate is found by the method described in section 3.6.4[22,23].

A new parabola is then fitted to these more precise co-ordinates and the coefficients of this parabola are used in the calculation of the final answers[52]. If there is more than one possible track in a subgroup, even after the angle criterion has been applied, parabolas are fitted to all possible combinations of the co-ordinates and the combination which has the smallest standard deviation of its points around the parabola is chosen[52].

Any bursts contained in the group combination are then examined to see if at least two tubes lie within 1.0cm of the fitted trajectory (see section 4.2)[53]. If none do, then error En1, where n is the tray number, is generated but the analysis continues[54].

4.7.5 Comparison of the Group Combinations

When only some trays contain two groups, the programme examines both group combinations and selects the better fit either on the basis of tray failure or the one with the smallest standard deviation of its co-ordinates around the fitted trajectory[55-56].

On the successful completion of the analysis of the first combination, the programme sets suitable flags and then analyses the second combination[58,59,61,62]. The two results are compared and the better one selected[63,64]. When the first combination is selected to be the better of the two, it has to be rerun because all the results of its original analysis were destroyed during the running of the second combination. The first combination is also rerun if the second combination fails[64-66].

4.7.6 Tray Failure with the Angle Criterion

Occassionally the programme finds that it is unable to fit a trajectory at the required angle through a subgroup, even when all the tray fitting options are tried[23]. When this occurs, the other subgroups of the group, if present, are examined to see if they contain a track which satisfies the fitting criteria [24,25]. If the programme is still unable to find a suitable track the programme decides what other group combinations are available to it and examines any possibilities[26-51].

When all the trays contain only one group, the offending tray is omitted from any further calculations and error code En1, where n is the tray number, is generated and the analysis continues[26,29,28,46-51].

When all the trays contain two groups error E15 is generated if the first combination fails[30,31,28] and E16 if it is the second[26-28]. In both cases the offending tray is omitted, error code En1 generated and analysis continued (46-51).

The options available to the programme are more complex when only some trays contain two groups, because it has to decide which is the best option to use. When the first group combination is under study, the other combination is examined (32,33). If there are insufficient usable trays in the second combination, code E17 is generated and the event terminated[34,41], otherwise the second groups, in those trays with two groups are examined[35,36]. If any fail, the first group in that tray is rerun[37]. When a set of new co-ordinates has been obtained a new parabola is fitted and the angle criterion applied. If this combination fails as well then the offending tray(s) are omitted, error code En1 generated and analysis continued with this combination[46-51].

When a tray is omitted from a group combination, a count is made of the remaining usable trays and if this becomes less than three, error code E12 is produced[48,50,51]. Analysis is then terminated unless all the trays contain two groups and the second combination is yet to be examined, in which case analysis continues with the second combination[13-17].

4.7.7 The Storing of the Answers

The momentum, the sign of the charge of the muon and the projected zenith angle are then calculated from the coefficients of the parabola fit for the group combination, using equations 3.4 and 3.5 and the direction of the magnetic field (67). The answers, together with the standard deviation of the co-ordinates around the parabola and the tray fit option codes, are stored in the dummy columns of the data and in the output file. Bursts and unusable trays are also flagged in the output[68].

Table 4.3

The Contents of the Dummy Columns after Analysis

Tray Number	Column Number	Contents
1	91	Unchanged
	92	Tray 1 codes*
	93	1st Error Code
	94	2nd Error Code
	95	3rd Error Code
	96	4th Error Code
2	91	Unchanged
	92	Tray 2 codes*
	93	Number of muon tracks analysed
	94	Number of azimuthal tracks analysed
	95 and 96	Unchanged
3	91	Unchanged
	92	Tray 3 codes*
	93 and 94	Momentum of 1st muon
	95 and 96	Momentum of 2nd muon
4	91	Unchanged
	92	Tray 4 codes*
	93 and 94	1st azimuthal angle
	95 and 96	2nd azimuthal angle
5	91	Unchanged
	92	Tray 5 codes*
	93 and 94	Zenith angle of 1st muon
	95 and 96	Zenith angle of 2nd muon
6	91	Unchanged
	92	Tray 6 codes*
	93 and 94	Standard deviation of trajectory of 1st muon
	95 and 96	Standard deviation of trajectory of 2nd muon
7	91	Unchanged
	92	Tray 7 codes*
	93 - 96	Unchanged

* Tray codes are: /number of groups (8 bits)/tray fit code of 1st muon (4 bits)/tray fit code of 2nd muon (4 bits)/.

When all of the trays contain two groups, the second combination is then analysed and the results similarly stored[69,13].

4.7.8 The Analysis of the Azimuthal Trays

The azimuthal trays, if present, are only analysed by the programme if a momentum fit has been successful, otherwise they are ignored[70,71]. A maximum of two groups in a tray can be handled otherwise the trays are flagged as unusable. The method of calculating the azimuthal angle is described in section 3.4.3. Because no track fitting is attempted, it is impossible to distinguish between spurious groups of tubes and those pertaining to the actual muons. Once again, the trajectories of multiple particle events are assumed to be parallel and the first groups in each tray are taken together and the second groups, if present, likewise. If one tray has two groups and the other only one, only the two first groups are taken. The calculated azimuthal angle(s) are stored with the rest of the data[72,73].

The analysis of the event is now complete and the programme continues with the next event[1].

4.8 The Format of the Dummy Columns and the Answer File

Table 4.3 shows the contents of the dummy columns of the data after analysis. The answer file consists of the event header information and a direct copy of the dummy columns. If a serious error has prevented the storing of the answers in the dummy columns, then the output file only contains the event header and the error code.

Column 91 of all the trays is never altered and acts as a dividing line between the tray data and the answers when the data is rescanned for transmission to the NUMAC computer. Column 92 of all the trays contains the tray fit code for that tray. It contains E19 if the tray was unusable otherwise, assuming the event was analysed, it contains details of the number of groups in that tray, their tray fit option codes and a special flag if they contained a burst.

The format of this column is also shown in table 4.3.

The contents of the remaining columns in a tray depend upon the tray number. Tray 1 contains any generated error codes (a maximum of 4 are stored). Columns 93 and 94 of tray 2 contain the number of muons and the number of azimuthal tracks analysed respectively. Two 16-bit words are required to store a floating point number and consequently, two dummy columns are required to store each computed momentum, zenith angle and azimuthal angle. Columns 93 and 94 of tray 3 contain the momentum of the first muon and columns 95 and 96 contain the momentum of the second, if present. These momenta are stored as negative numbers if the sign of the charge of their muons was negative. Similarly trays 4, 5 and 6 contain the azimuthal angles, the zenith angles and the standard deviations of the parabola fits respectively.

When any of the trays are not present in the data, the corresponding quantities, which are stored in those trays, are omitted.

4.9 The Output from the Programme

The answer file is transferred to the satellite IBM 1130 computer of NUMAC in Durham and here it is interpreted by a special programme, known as ANSER, which produces a list of the events on the line printer. For each event, the contents of the event header are decoded and printed as are the other quantities stored in this file. Figure 4.5 shows the output for a typical event. Any error codes associated with an event are printed immediately after the header and the last line is repeated if two muon trajectories were analysed.

The file containing the original data is, after analysis, translated by a special programme, known as TRANF, which prepares the data for transfer to NUMAC. The output from this programme is another data file which is composed of pseudo punched card images. The first few cards are the job control statements necessary to have the magnetic tape mounted and to execute a programme which reads the data and writes them on the magnetic tape. The cards that follow these statements contain the data for all the events.

Figure 4.5   The Printed Output for a Typical Event.

The first card of each event contains the following quantities: the event number, the time and date and the atmospheric pressure (all in decimal format); a special code containing the trigger mode, the direction of the magnetic field and the magnet current; and then, in decimal format, come the number of muons, azimuthal tracks, errors and trays present, the length of the data for each tray, the total length of the data and any error codes. The second card contains the momentum, azimuthal and zenith angles, and the standard deviation of the tracks, for all muons analysed. These are all in decimal format. The third and subsequent cards contain information pertaining to each tray. The number of groups in each tray and their respective track fitting options appear first, followed by the data for each tray, excluding the tray headers and dummy columns. The information in these cards is in the same format as the original data and it is read by the NUMAC computer in binary format. This sequence of cards is continued for all the data in the input file. After these data cards, there are a few more job control statements which terminate data storage.

The disc containing this file is placed on the satellite IBM 1130 computer and the file is transferred to NUMAC. Here it appears as a normal job entered from cards and it is subsequently executed.

4.10 The Zero Magnetic Field Data Analysis Programme

It is essential that the positions of the measuring trays are known very precisely and the best way of finding these positions is to analyse the trajectories of muons through the spectrograph when there is no prevailing magnetic field. A minimum of three points is required to define a parabola and in fact, it is only necessary to know the position of one point with respect to two others. Consequently, trays 1 and 5 are taken to be the reference frame and the distances between the tracks in trays 2, 3 and 4 and a straight line drawn between the tracks in trays 1 and 5 are calculated. The scattering of the

muons in the magnet broadens the distributions of these distances and many muon trajectories have to be analysed before the tray positions can be found precisely.

The method of analysing the data is exactly the same as for the momentum analysis, except for the calculation of the final answers. If either tray 1 or 5 is unusable or contains a burst, the event is declared void. The distances from the straight line drawn between the tracks in these two trays and the tracks in the other three trays are calculated and they are histogrammed by the programme. Any tray which was either unusable, or contained a burst, or had an associated error code, is omitted. The three distances are also stored in the dummy columns of the trays to which they pertain. The three histograms are made available for inspection at the end of the analysis.

CHAPTER 5

The Properties and Accuracy of the Analysis Programme

5.1 Introduction

This chapter is devoted to a study of the properties of the analysis programme, the accuracy of its results and the corrections which have to be applied to them. The maximum detectable momentum (m.d.m.) of MARS is also calculated. The track fitting options used by the programme to locate the trajectories of the muons are investigated and an attempt is made to reconcile the frequency of their occurrence with theoretical calculations and data. The data used to investigate the properties of the programme were the same as those used in the experiments described in chapters 6 and 7. The mean momentum of these data was only 20 GeV/c and only 140 events were analysed with momenta in excess of 100 GeV/c. Although initially the programme was not intended to analyse data with momenta as low as this, the data served as a useful check on the programme's performance.

5.2 A Comparison between the Accuracy of Track Location Achieved by the Computer Technique and Visual Processing

The accuracy of the location of tracks in flash-tube trays by the technique described in section 3.6 was compared with that achieved by conventional visual processing of the same data. The data was taken from the experiment of Alexander and Thompson (1969) and a schematic diagram of their apparatus is shown in figure 5.1. Four flash-tube trays A, B, C and D were used to locate the muon's trajectory before and after traversing a magnetic field. When the two trajectories, ab and cd, are constructed, they do not intercept at the centre of the magnetic field. This discrepancy, e, can only be attributed to uncertainties in track location because the use of an air gap magnet minimised the particles Coulomb scattering in the apparatus. The standard deviation of the distribution of the discrepancies is a measure of the location accuracy and this was used to compare the two methods of track location.
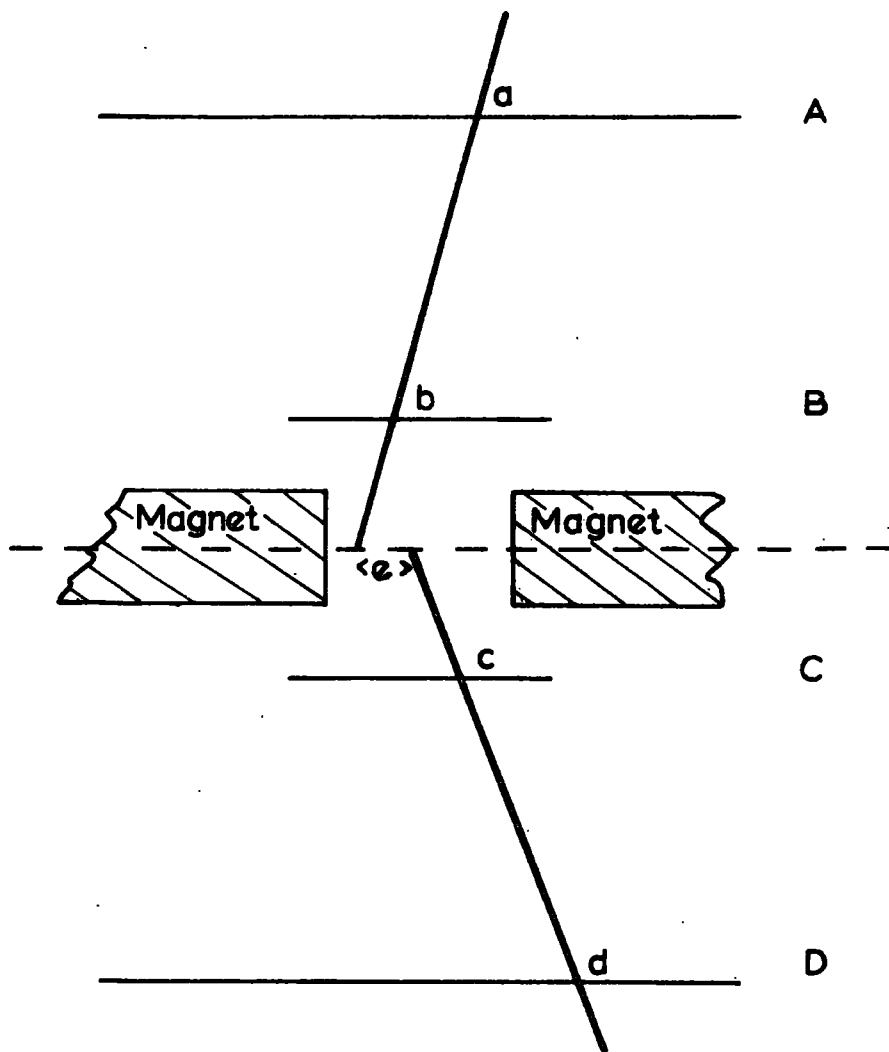
Figure 5.1   A Schematic Diagram of the Apparatus of
Alexander and Thompson (1969)

The data for the experiment were collected photographically and the method of visual processing was to study a projected image of the events and to determine the best position of the tracks by placing a cursor across the tube patterns. The co-ordinates of the tracks in each tray were recorded. The tube patterns for the same events were suitably coded and this information was used by the computer technique to locate the trajectories.

The discrepancies at the centre of the magnet were calculated for each event and the distribution of discrepancies for each method are shown in figure 5.2. The standard deviation of the distribution for the visually processed data was 0.153 ± 0.013 cm and 0.109 ± 0.010 cm for that processed by the computer technique. It is concluded that the computer technique for the location of tracks in flash-tube trays is more accurate than the method of visual scanning.

5.3 Examination of the Track Option Fits

5.3.1 Introduction

The frequency that the track fitting options occur is dependent upon the sizes of the tubes and the spaces between the tubes that are used in the analysis programme. It was stated in Chapter 3 that it is necessary to allow some overlap of the tubes and spaces to compensate for the variation of the tube internal diameters and for the slight bending of the tubes. The amount of overlap that is required cannot be measured directly but can only be inferred by an analysis of data from the flash-tube trays in question. If the frequency of occurrence of one of the track fitting options can be calculated theoretically then it is possible to determine the overlap that is required.

5.3.2 The Expected Rate of Knock-on Electrons

Knock-on electrons, which are produced as the muon traverses matter, may sometimes cause a tube to be discharged in a layer of flash-tubes, whereas the muon passed outside of the sensitive region of that layer. Before the programme

Visually Processed Results

$6 = 0.153 \pm 0.013$ cm

Computer Results

$6 = 0.109 \pm 0.010$ cm
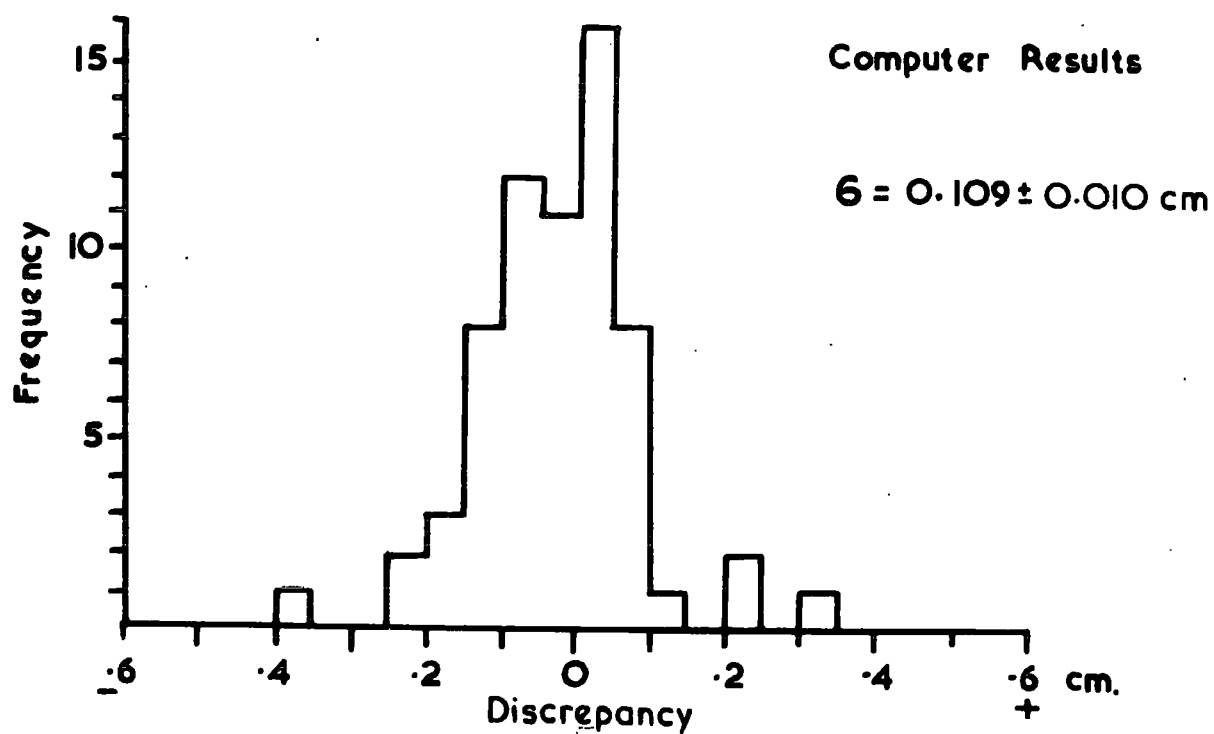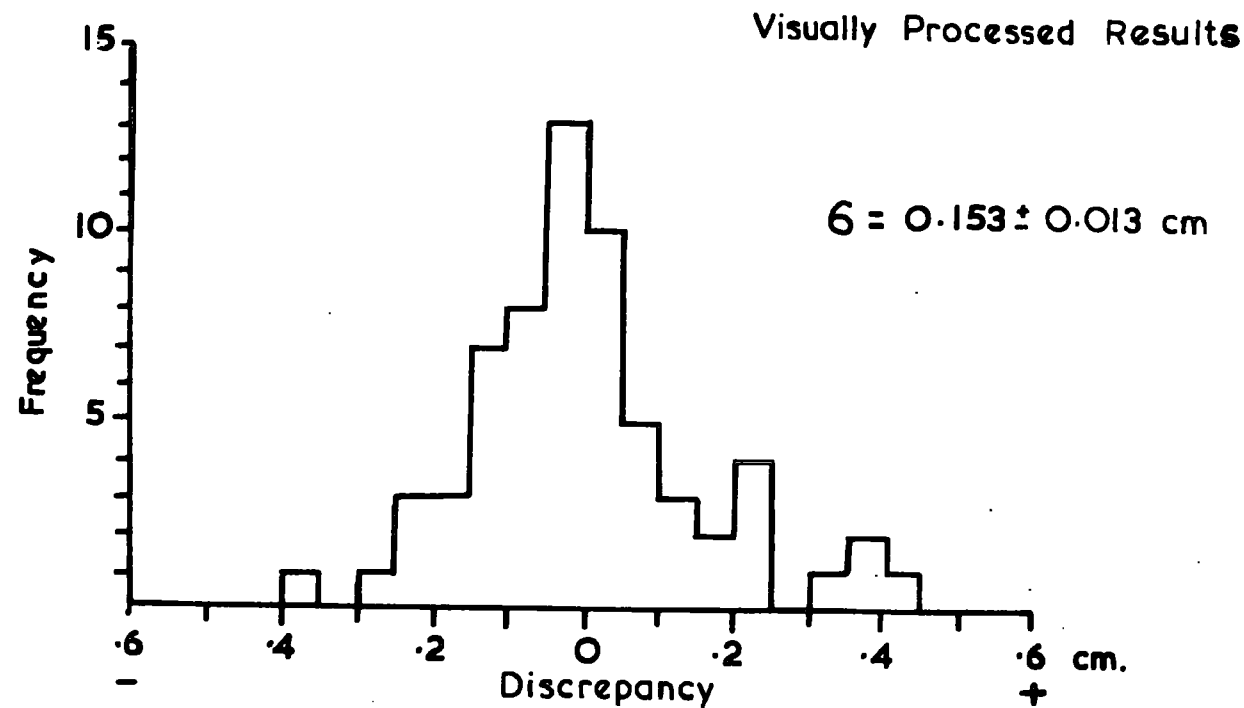
Figure 5.2 The Discrepancy Distributions for the Visually and Computer Processed Data.

is able to fit a trajectory to the resulting flash-tube configuration, it is necessary that the offending tube be turned 'off' by the programme. Such events are handled by track fitting option 1.

An estimate of the probability of production of these knock-on electrons has been made with the theory of Bhabha (1938), the range-energy curves for electrons as given by Katz and Penfold (1952) and the angular distribution of electrons as given by Rossi (1961). After Bhabha, the probability of an energy transfer of E' to an electron, of mass M_e, from a muon of mass M_μ and energy E is

$$\Psi(E,E').\ dE' = 0.3\ \frac{M_e c^2}{\beta^2}.\ \frac{Z}{A}.\ \frac{dE'}{(E')^2}\ \left(1 - \beta^2 \frac{E'}{E_m} + \frac{1}{2}\left(\frac{E'}{E + M_\mu.c^2}\right)^2\right)$$

$$gm^{-1}.\ cm^{-2}$$

where E_m is the maximum transferable energy. Z and A have their usual meaning and are the average values for the material being traversed. The flash-tube trays consist of aluminium and glass and the mean value of Z/A is 0.482. For a 30 GeV incident muon $\beta = 1$ and $E_m = 23$ GeV. The physical conditions placed on the knock-on electron by the option 1 fit is that it must be contained within one layer of tubes and, from the range-energy relation of Katz and Penfold, the maximum energy transfer that is permitted is ~1 MeV. Hence, $E'/E_m \ll 1$ and $E'/(E + M_\mu c^2) \ll 1$ and consequently, for aluminium and glass

$$\Psi(E,E')\ dE' = 0.0739.\frac{dE'}{(E')^2} \tag{5.1}$$

This equation has been used to calculate the rate of track fitting option 1. A section of a flash-tube layer, as shown in figure 5.3, was considered and the rate that knock-on electrons enter either of the two tubes after production in the region between the two vertical lines was calculated. For these calculations it was assumed that 1) above the top electrode there was a layer of glass which corresponded to the tube layer above and in which knock-on electrons could be produced; 2) there was a similar layer of glass below the bottom electrode
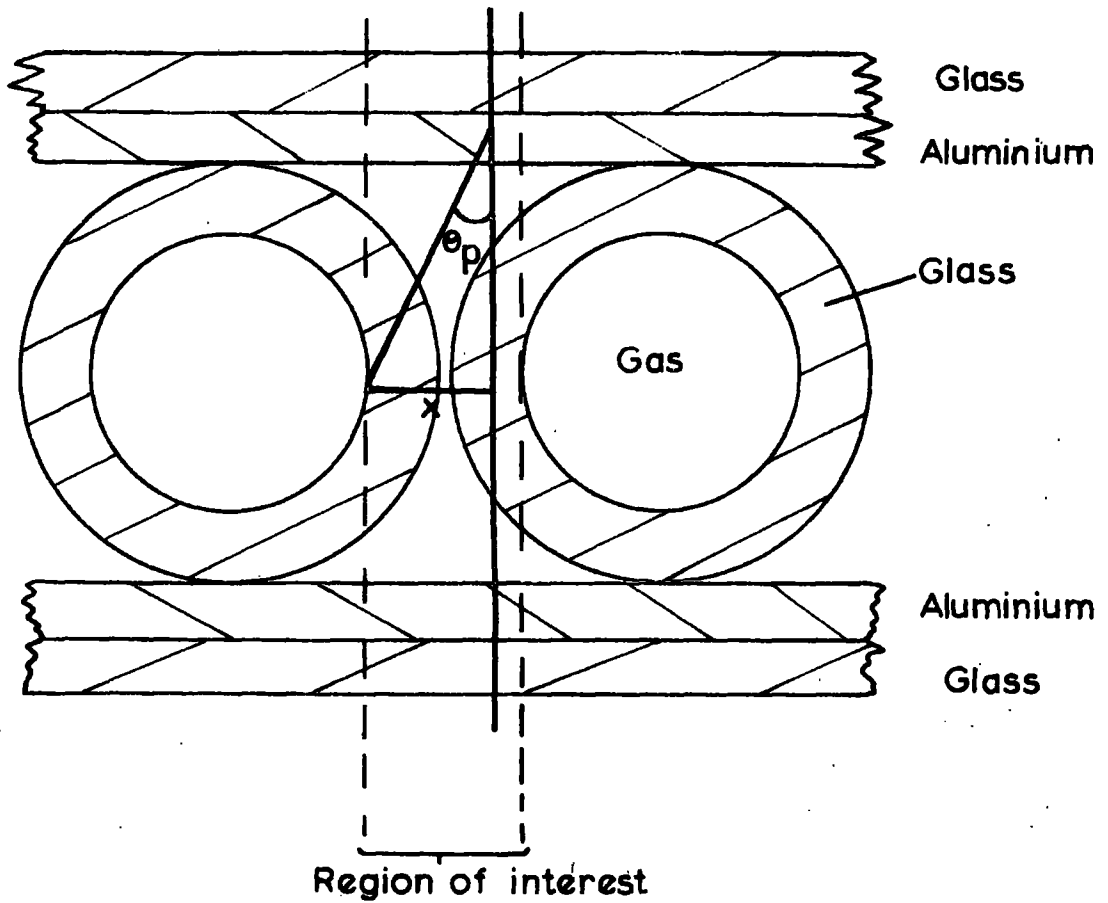
Figure 5.3   The Region of a Tube Layer Considered for Knock-on Electron Production.
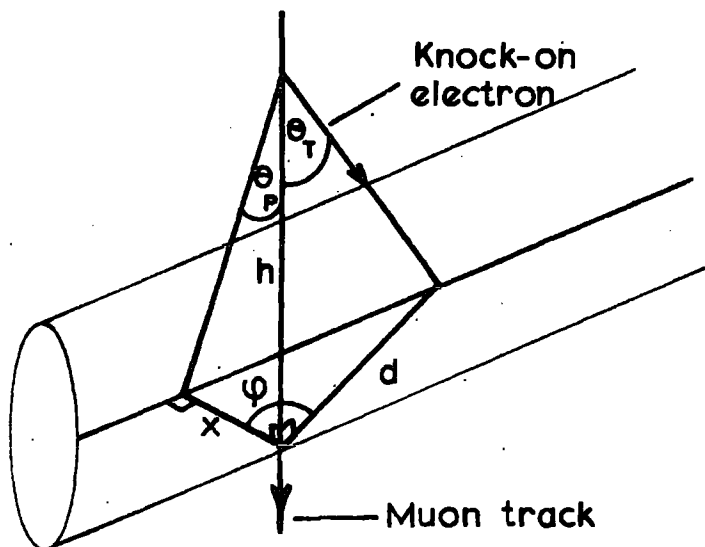
Figure 5.4   The Co-ordinate Frame of the Knock-on Electron.

beyond which knock-on electrons must not pass and 3) if the electron reached the inside of the tube, then the tube discharged.

The angular distribution of the electrons, the amount of absorber traversed and the geometrical acceptance of the tubes were also considered. The spatial angular distribution of electrons with respect to the trajectory of the muon is a function of the electron's energy and, after Rossi, is given by

$$\cos \theta = \left(\frac{E'}{E' + 2M_e} \right)^{\frac{1}{2}} \qquad (5.2)$$

The acceptance for the knock-on electrons was calculated as follows. It was assumed that, for the tube to discharge, the electron had to be inside the tube before it was below the mid point of the tube layer. With reference to figure 5.4, if h is the height of production above the mid point, d the projected horizontal distance to the tube and x the perpendicular distance to the tube, then $d = x.\sec \psi$, where ψ is the azimuthal production angle. Also $d = h. \tan \theta_t$, where θ_t is the angle between the muon and the electron. Hence $\sec \psi = (h/x). \tan \theta_t$. All electrons within an azimuthal angle of ψ are accepted by the tube and the mean projected angle between the muon and electron is

$$\theta_p = \tan^{-1} (\tan \theta_t. \cos(\psi/2)).$$

Hence

$$\cot \theta_t = \frac{x/h \pm \sqrt{(x^2/h^2 + 8\tan^2 \theta_p)}}{4 \tan^2 \theta_p} \qquad (5.3)$$

The angular acceptance, A, for such an electron by one tube is $2\psi/\pi$ and hence

$$A = \frac{2}{\pi} \cos^{-1} \left(\frac{x}{h} \cot \theta_t \right) \qquad (5.4)$$

The region of interest in figure 5.3 for the production of knock-on electrons was divided up into small cells of known x and h. The probability of a tube discharging due to a knock-on electron in a cell was then calculated by integrating equation 5.1 and multiplying by the acceptance at the mean value of θ_t. The energy range of the integration was found by considering the permitted angular range of the knock-on. This was defined by the geometrical acceptance of the tubes, the minimum and maximum thickness of absorber through which the electrons had to pass to reach the tube (allowance was made for the variation of these with the azimuthal angle), and the angular limitation imposed by equation 5.2. The latter occurs because the electron's energy at a certain angle may be insufficient to enable it to traverse the absorber.

The total probability of a knock-on electron causing a tube to discharge in a layer which would not have otherwise contained a discharged tube was found to be 5.2 ± 0.8%. The error was estimated after considering the uncertainties in density and the integration limits. The possibility of the same electron entering the next layer of tubes without being detected is also included in the error.

5.3.3 The Theoretically Expected Frequency of Option 1 Fits

Before it is possible to calculate the expected rate of option 1 fits, two properties of the experimental data with which it is to be compared have to be considered. Firstly, the data has an angular distribution somewhat larger than 7° because it is predominently composed of low momenta particles and secondly, the knock-on probability calculated above has to be corrected for the occurrence of spuriously discharging tubes close enough to the track as to give rise to an option 1 fit.

An examination of the film data yielded a spurious rate of 5.7 ± 1.7 tubes per tray, and, as there are 712 tubes in a tray, the chance of a spurious discharge occurring in a tube next to the muon track is (1.6 ± 0.5)% per layer.

Of these 5.2% will be accompanied by a knock-on electron and they will not contribute to the option 1 rate. Hence, the total probability of an influential tube discharging in a layer either spuriously or because of a knock-on electron is $(6.72 \pm 0.94)\%$.

The angular distribution of the muon tracks in the flash-tube trays for the data is shown in figure 5.5 and it can be seen that it extends to beyond 15°. The theoretical tube population distribution along a track has been found by taking 2500 randomly positioned tracks in a flash-tube tray with an angular distribution corresponding to that of the data and the result is shown in figure 5.6. The internal flash tube diameter used in deriving this distribution was the experimentally measured value of 0.543 ± 0.003 cm. The mean tube population of the distribution is 5.024 ± 0.034. The uncertainty was determined by the statistics of the calculation and the uncertainty in the mean tube diameter.

The expected rate of option 1 fits was calculated from the tube population distribution by taking a binomial probability of 0.0672 for all those layers not containing discharged tubes. The resulting probability of an option 1 fit is $(17.22 \pm 2.0)\%$. In practice however, the option 1 rate will be slightly lower than this value because some option 1 candidates will satisfy the fitting criteria with option 0.

5.3.4 The Theoretically Expected Frequency of Option 2 Fits

The expected frequency of occurrence of the tube inefficiency option (option 2) is more difficult to calculate because the efficiency of a flash-tube cannot be satisfactorily explained on purely theoretical grounds. It can however be calculated from the experimental and theoretical layer efficiencies of the trays and the rate of option 1 fits. The theoretical layer efficiency, η_{t}, of the tube population distribution in figure 5.6 is 0.628 ± 0.004 and the experimental layer efficiency, η_{m}, of the data (from 24000 tracks) is
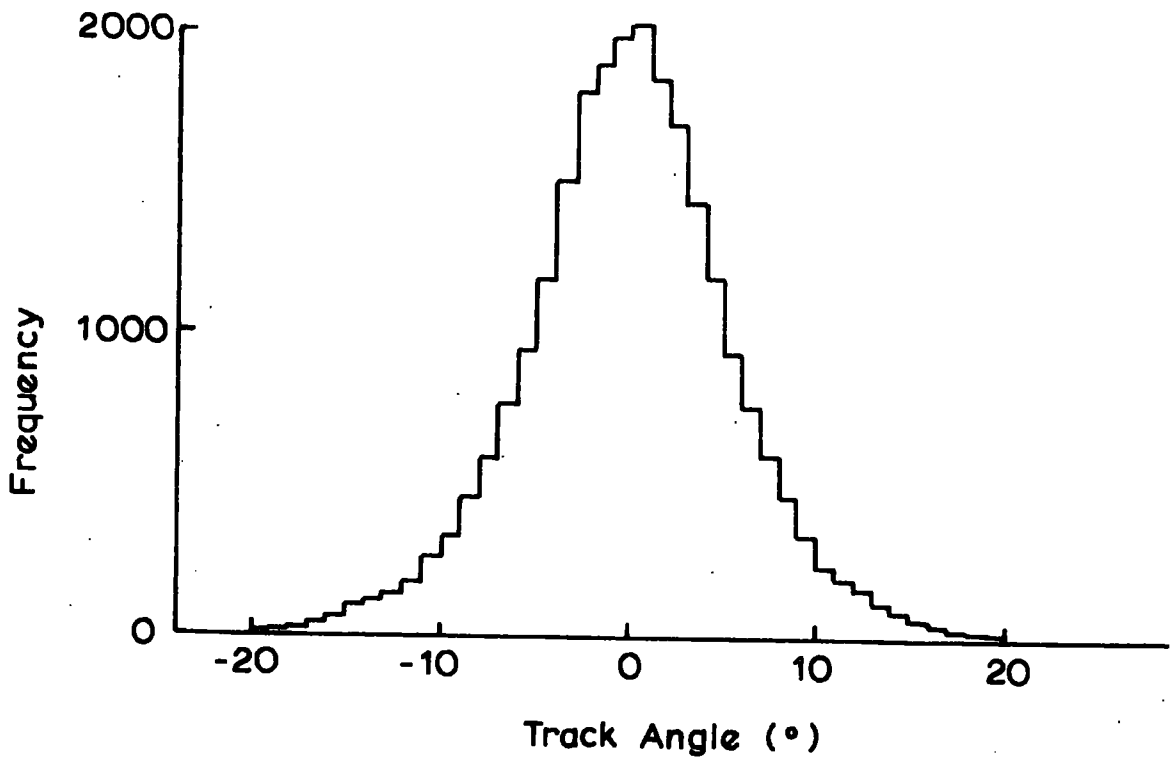
Figure 5.5 The Angular Distribution of the Tracks in the Trays for the Film Data.

Mean Tube Population = 5.024 ± 0.034
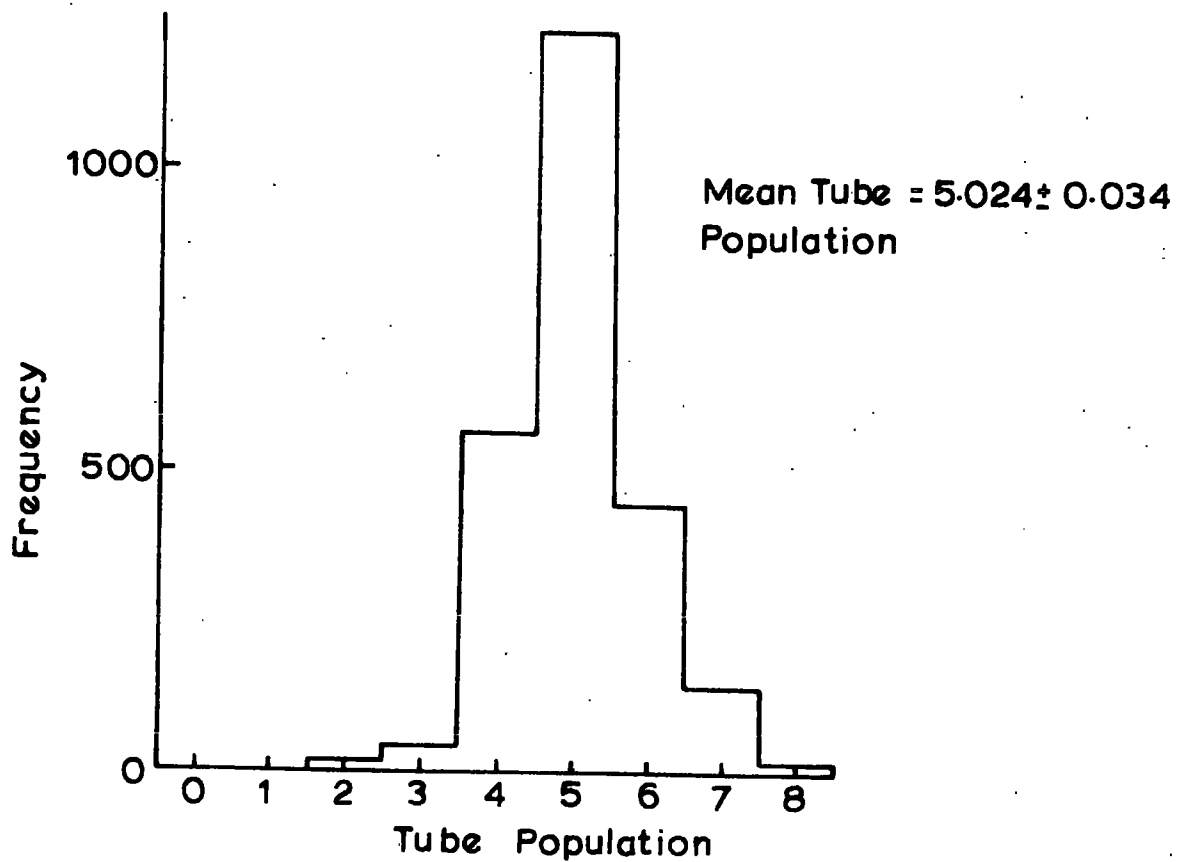
Figure 5.6 The Tube Population Distribution

is 0.6298 $\pm$ 0.0009. This latter value contains tracks with knock-on electrons and with tube inefficiencies and it can be expressed in terms of the theoretical layer efficiency by the equation

$$\eta_M \simeq P_T \, \eta_T \; + \; P_{KO} \eta_{KO} \; + \; P_{KOKO} \, \eta_{KOKO} \; + \; P_{IN} \eta_{IN} \; + P_{ININ} \, \eta_{ININ} + P_{KO} P_{IN} \eta_T$$

$$(5.5)$$

with the condition that

$$P_T + P_{KO} + P_{KOKO} + P_{IN} + P_{ININ} + P_{KO} \, P_{IN} = 1.$$

Here P_T, P_{KO}, P_{KOKO}, P_{IN} and P_{ININ} are the probabilities of no knock-ons or inefficiencies, of one single knock-on, of two knock-ons in different layers, of one tube inefficiency and of two inefficiencies in different layers, respectively, and η_T, η_{KO}, η_{KOKO}, η_{IN} and η_{ININ} are the corresponding layer efficiencies.

Whilst calculating P_{KO} in the previous section, the tube population distribution for option 1 events was calculated and it had a mean layer efficiency of 0.7237 $\pm$ 0.0048. P_{KOKO} and η_{KOKO} have been calculated in a similar manner and have values of 0.0146 $\pm$ 0.0041 and 0.8088 $\pm$ 0.0054 respectively. The equivalent quantities for tube inefficiencies could also be calculated if a value for the flash-tube internal inefficiency was known. However, as the quantities are determined by the choice of inefficiency, successive values can be chosen until one is obtained which causes equation 5.5 to be satisfied. The result of such an iteration leads to a value of 0.0325 $\pm$ 0.0074 for the tube internal inefficiency and the corresponding values of P_{IN}, P_{ININ}, η_{IN} and η_{ININ} are 0.142 $\pm$ 0.037, 0.010 $\pm$ 0.005, 0.5206 $\pm$ 0.0035 and 0.4211 $\pm$ 0.0028 respectively.

It is concluded that the theoretically expected frequency of occurrence of option 2 is (14.2 $\pm$ 3.7)% but again, the experimental frequency should be slightly lower because some option 2 tracks will be lost to option 0 or to option 1.

5.3.5. Comparison of the Theoretical and Experimental Frequencies of Options 1 and 2

A sample of data comprising of 200 events (1000 tracks) were analysed for various sizes of the tube internal diameters and the gaps between the tubes and the frequency of occurrence of the track fitting options found. Figures 5.7 and 5.8 show the frequency of option 1 and option 2 respectively. The abscissa and the parameter of each graph are plotted as a percentage of the mean measured internal tube diameter and gap sizes which were 5.43 $\pm$ 0.03 mm and 3.17 $\pm$ 0.03 mm respectively. The accuracy of the data is 0.2% but the points have been normalised to the respective option rates obtained from the analysis of 32,500 tracks. The points are not independent because they are based on the same sample of data but an alternative sample has also been analysed in a similar manner and it shows a form consistent with the results presented.

The corresponding theoretical rates with their uncertainties are also shown on the figures and it can be seen that the experimental and theoretical results are in good agreement. It is now possible to calculate the effective internal tube diameter and gap sizes for the flash-tube trays and hence the values to be used by the analysis programme.

5.3.6 The Effective Tube and Gap Sizes

The possible limits which can be placed on the tube diameters and gap sizes from the analysis of option 2 events can be displayed on the same diagram as those for option 1, as shown in figure 5.9. If the experimental frequency of options 1 and 2 are to be kept to within one standard deviation of the theoretically predicted values, the selected tube and gap sizes must lie somewhere within the area defined by ABCD.

Before the actual values can be chosen, it is necessary to consider two other properties of the programme which are dependent upon the tube and gap sizes, namely, the execution time and the accuracy of location of the tracks in the trays.
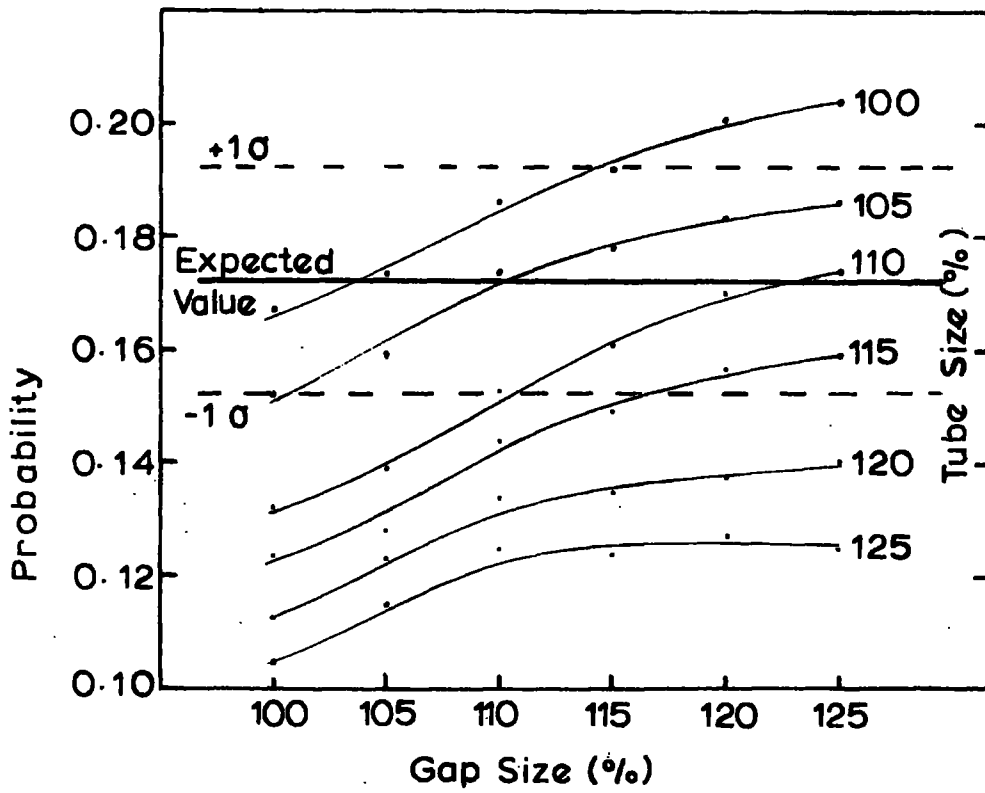
Figure 5.7   The Probability of an Option 1 Fit as a Function
of Tube and Gap Size.
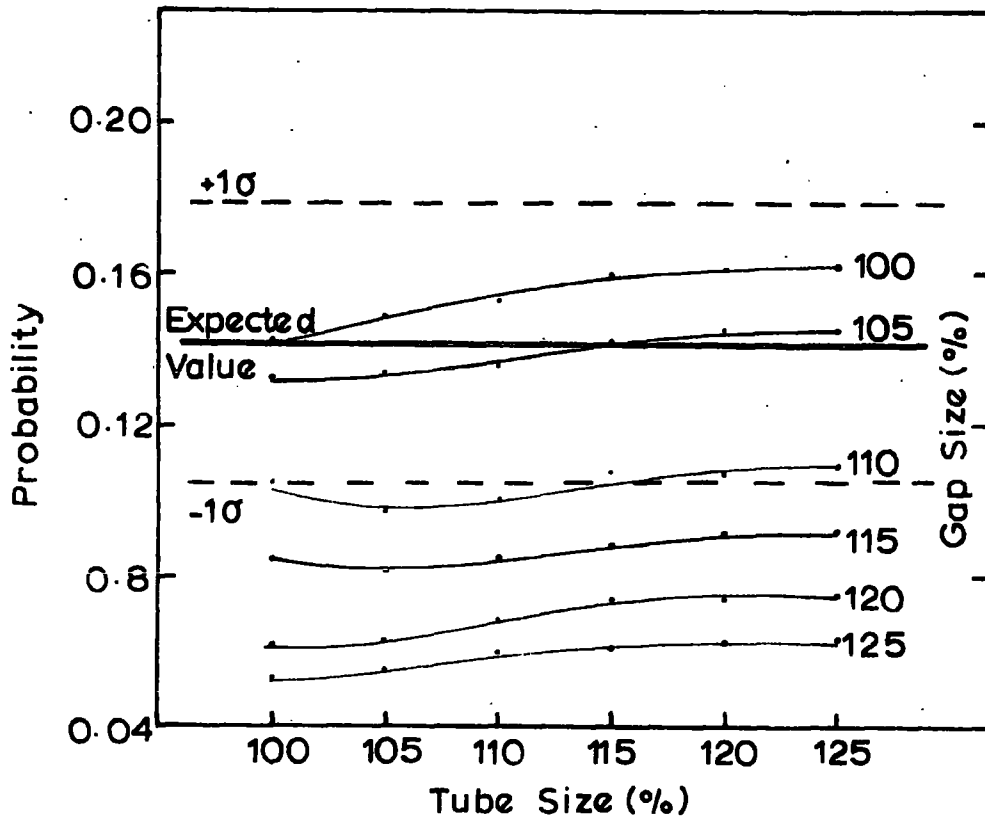
Figure 5.8   The Probability of an Option 2 Fit as a Function
of Tube and Gap Size.

The execution time is a function of the tube parameters because, before a track

fitting option is reached, all previous options have to be tried and this is

time consuming. Similarly, the accuracy of track location is a function of the

parameters because the channel widths in the trays depend upon these parameters.

After consideration of the accuracy of the theoretical results, the

discussion above and the fact that the observed frequencies of occurrence of

option 1 and 2 will be lower experimentally because of losses to option 0 (and to

option 1 in the case of option 2), it is concluded that allowance is satisfactorily

made for the various deficiencies in flash-tube alignment and sizes by considering

that the tube diameters and gaps are each 10% larger than the mean geometric

sizes. The tubes are therefore considered to have a diameter of 5.97 mm and

the gaps between the sensitive regions to be 3.49 mm wide. The distance between

tube centres is 8.6 mm and hence there is a region of overlap of 0.43 mm where

no regard is taken as to whether the tube discharged or not.

5.3.7 The Order of the Track Fitting Options

With a tube and gap enlargement of 10%, the rate of option 1 and 2 events

from figures 5.7 and 5.8 are 15.0% and 10% respectively. It is possible to

calculate the theoretical rates of all the other options from these two values

and these are tabulated in the order of decreasing probability in table 5.1.

The probability of option 3 is simply the product of options 1 and 2. However,

the probabilities of options 4, 5 and 6 are not simply the square of the

corresponding option 1 or 2 probability, because the number of layers available

to the second inefficiency or knock-on is one less than that for the first.

This has been considered in the theoretical calculations. The probability of

there being two tubes discharged on the same side of the track due to knock-on

electrons is unknown because they are either the result of a small electron

shower or a badly scattered high energy knock-on electron. Consequently, it

has only been possible to estimate the probabilities of options 6, 9 and 10.

An option 1 rate of 15.0% corresponds to a probability of 5.6% per layer of
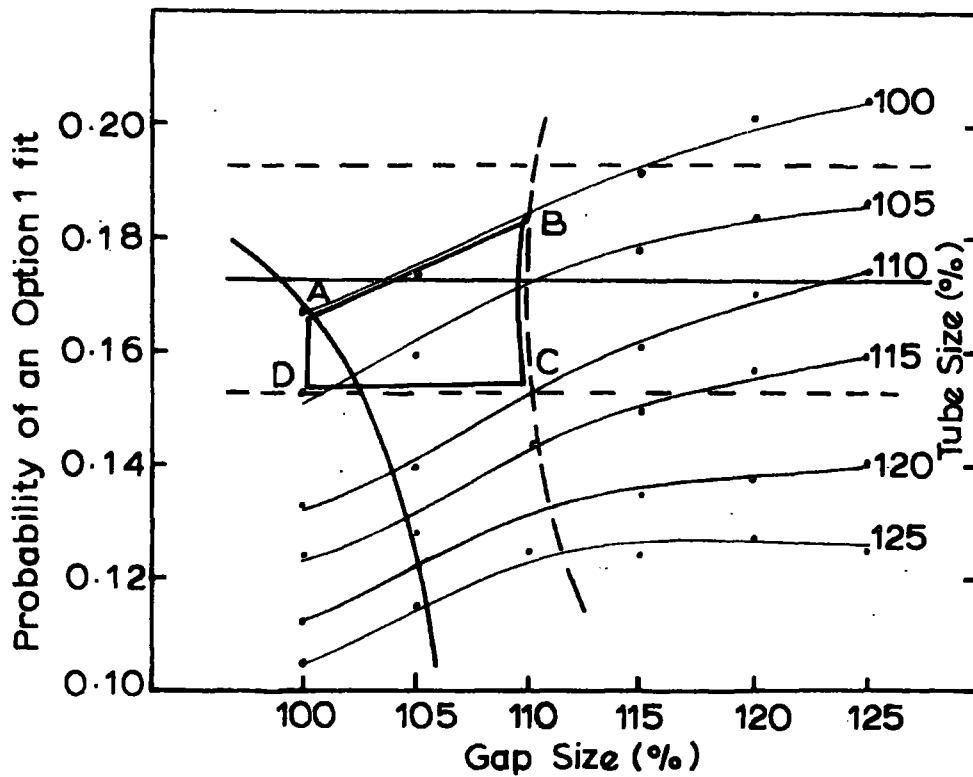
Figure 5.9 The Limits which can be set on the Gap and Tube Sizes.

Standard deviation = 0.318 ± 0.002 mm
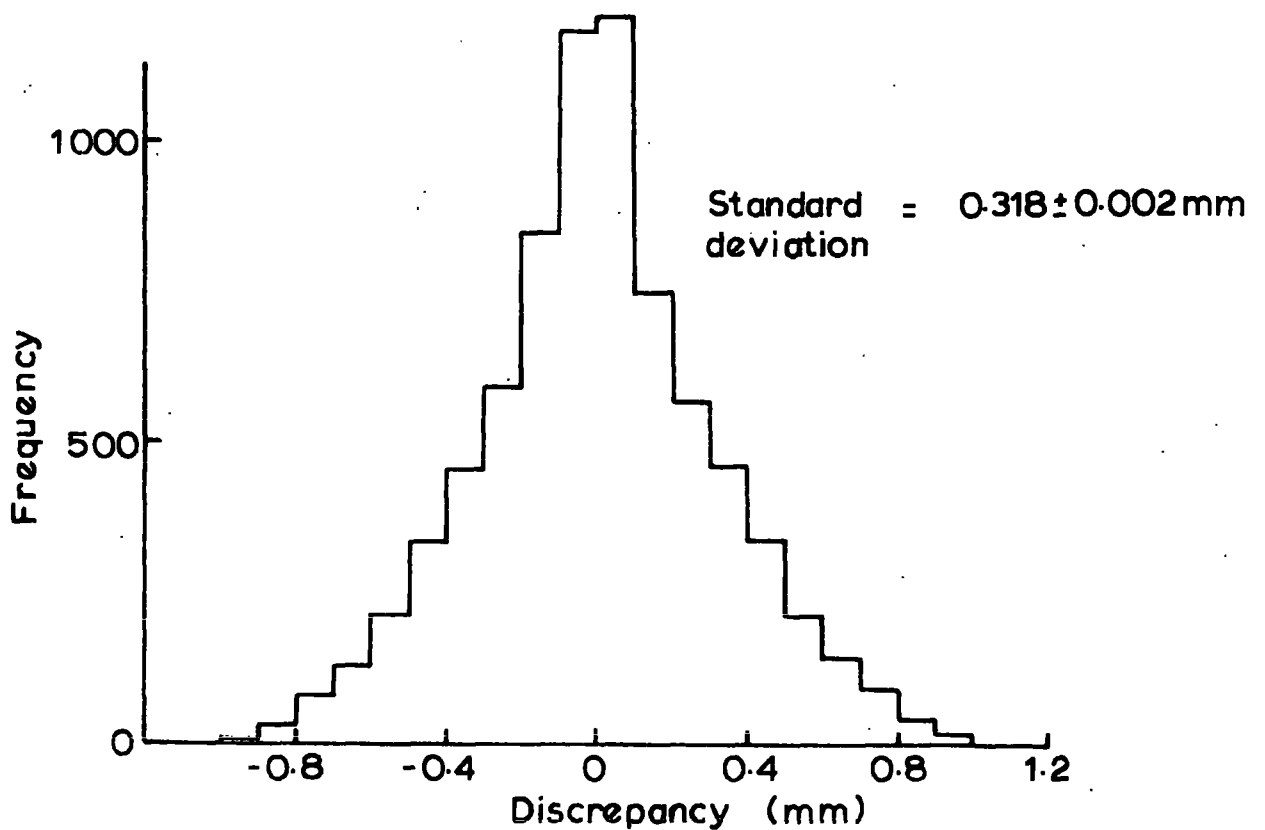
Figure 5.10 The Frequency Distribution of the Discrepancies between the True and Computed Trajectories in a Tray.

producing a knock-on and an option 2 rate of 10.0% corresponds to a tube

internal efficiency of 97.8%. The probabilities of options 7 and 8 were

calculated by taking the product of either option 1 or 2 and the layer probability

of either a knock-on or an inefficiency occurring. The result was halved for

option 8 because the two knock-ons have to be in opposite directions. Option 11

is the product of the probabilities of option 2 and of two knock-ons in opposite

directions in the same layer.

The frequency that the options occur has also been found experimentally by

analysing the data eleven times with a different option first each time. The

proportion of tracks which satisfied the fitting criteria for each option when

it was first are also shown in table 5.1. It can be seen that, in general, the

theoretical and experimental rates are in very good agreement.

5.3.8 The Flash-Tube Layer Efficiencies of the Track Fitting Options

A sensitive test on the performance of the flash-tube track fitting technique

is a comparison between the layer efficiency of those tracks classified by the

programme under each option and the theoretical values given in sections 5.3.3

and 5.3.4. The theoretical layer efficiencies, η, are almost independent of

the choice of ϵ, where ϵ is the probability of observing either a tube discharging

because of a knock-on electron or a tube inefficiency, because $\partial\eta/\partial\epsilon \sim 0.1$ for

all options and hence $\Delta\eta \sim 0.001$. The largest contribution to the uncertainties

in the layer efficiencies is that due to the uncertainty in the theoretical mean

tube population which amounts to 0.7%. Consequently, agreement between the

theoretical and experimental layer efficiencies for the options would indicate

that the programme is interpreting the flash tube tracks correctly.

The theoretical layer efficiencies have only been calculated for options

0, 1, 2, 4 and 5 but the layer efficiencies of the other options are each related

to one of these predicted values. Option 3 should have a layer efficiency

corresponding to option 0 and so should options 7, 10 and 11; whereas options

8 and 9 should correspond to option 1 and option 6 to option 4.

Table 5.1

The Theoretical and Experimental Frequencies of
Occurrence of the Track Fitting Options

Option Number	Pictorial Description	Theoretical Frequency (%)	Experimental Frequency (%)
0		~69.6	64.2 ± 1.1
1		15.0	14.7 ± 0.8
2		10.0	11.1 ± 0.7
3		1.5	4.5 ± 0.2
4		1.4	2.0 ± 0.2
5		0.8	1.7 ± 0.2
6		~0.8	0.61 ± 0.08
7		0.6	0.5 ± 0.1
8		< 0.4	0.38 ± 0.07
9		< 0.4	0.21 ± 0.05
10		0.4	0.14 ± 0.04
11		0.02	0.04 ± 0.01
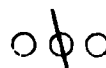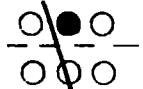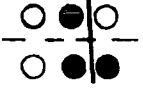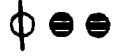
Table 5.2 contains the experimental and theoretical layer efficiencies and their equivalent mean tube density for all the track fitting options. It can be seen that they are in excellent agreement and this is taken as conclusive evidence that the technique developed to analyse flash-tube data correctly interprets the flash-tube configurations.

5.4 The Maximum Detectable Momentum of MARS

5.4.1 Theory

The maximum detectable momentum, m.d.m., is defined as that momentum at which the uncertainty in the momentum is equal to the momentum and it is the result of the uncertainties in the absolute position of the tracks in the flash-tube trays. It is calculated by a method similar to that as given by Allkofer et al. (1971 b). From equation 2.3, the momentum is given by $p = 0.03BH/\theta$, where B is the magnetic field (kilogauss), H is the length of the magnet (metres), and θ is the angular deflection (radians). θ can be rewritten as $1/r$, where 1 is the overall height of the spectrograph and r the radius of curvature of the muons trajectory. The radius is related to the coefficient of the x^2 term of the parabola fit, a, by $a = \frac{1}{2}r^{-1}$ (section 3.7.1) and hence $p = 0.03BH/2la$. If the uncertainty in a is Δa, then the m.d.m. is defined as

$$\text{m.d.m.} = \frac{0.03BH}{2l\,\Delta a} \qquad (5.6)$$

The coefficient a is defined from the parabola fit as

$$a = \frac{\Sigma x^3 \left(N\, \Sigma xy - \Sigma x\, \Sigma y\right) - \Sigma x^2 \left(\Sigma xy \Sigma x - \Sigma x\, \Sigma x^2\right) - \Sigma x^2 y \left(N\, \Sigma x^2 - (\Sigma x)^2\right)}{\Sigma x^4 \left((\Sigma x)^2 - N\, \Sigma x^2\right) + \Sigma x^3 \left(N\, \Sigma x^3 - \Sigma x \Sigma x^2\right) - \Sigma x^2 \left(\Sigma x^3\, \Sigma x - (\Sigma x^2)^2\right)}$$

$$(5.7)$$

where x and y are the co-ordinates of the parabola, N the number of points and $\Sigma x^m \equiv \sum_{i=1}^{N} x_i^m$. For the spectrograph, the x co-ordinates are known precisely because they are the positions of the trays, whereas the y co-ordinates are subject to the uncertainties of the track location in each tray. If the

Table 5.2

The Theoretical and Experimental Layer Efficiences
for the Track Fitting Options

Option	Experimental Value		Theoretical Prediction	
	Mean tube density	Mean Layer efficiency (%)	Mean tube density	Mean layer efficiency (%)
0	4.947 ± 0.009	61.84 ± 0.11	5.024 ± 0.034	62.80 ± 0.42
1	5.705 ± 0.017	71.31 ± 0.21	5.790 ± 0.039	72.37 ± 0.49
2	4.137 ± 0.016	51.71 ± 0.20	4.165 ± 0.028	52.06 ± 0.36
3	4.910 ± 0.025	61.38 ± 0.31	as option 0	
4	6.577 ± 0.052	82.21 ± 0.65	6.47 ± 0.043	80.88 ± 0.55
5	3.324 ± 0.077	41.55 ± 0.96	3.369 ± 0.023	42.11 ± 0.30
6	6.81 ± 0.14	85.1 ± 1.7	as option 4	
7	4.94 ± 0.12	61.8 ± 1.5	as option 0	
8	5.50 ± 0.35	68.8 ± 4.4	as option 1	
9	5.68 ± 0.50	71.0 ± 6.3	as option 1	
10	5.0 ± 0.7	63.0 ± 9.0	as option 0	
11	6.0 ± 0.8	75.0 ± 10.0	as option 0	

uncertainty in the track location in a tray is Δy, then the uncertainty in the coefficient a is

$$\Delta a = \left(\sum_{i=1}^{N} \left(\frac{\partial a}{\partial y_i} \right)^2 \right)^{\frac{1}{2}} . \Delta y$$

Hence, from equation 5.7,

$$\Delta a = F(x).\Delta y$$

where $F(x)$ is purely a function of the co-ordinates of the spectrograph and is defined as

$$F(x) = \sqrt{\left(\frac{N \Sigma x^2 - (\Sigma x)^2}{\Sigma x^4 (N \Sigma x^2 - (\Sigma x)^2) - N(\Sigma x^3)^2 + 2\Sigma x^3 \Sigma x^2 \Sigma x - (\Sigma x^2)^3} \right)}$$

Hence the m.d.m. is given by

$$\text{m.d.m.} = \frac{0.03BH}{21F(x).\Delta y} \tag{5.8}$$

5.4.2 The Accuracy of Track Location

The programme when fitting a track through a flash-tube configuration defines a channel in the flash-tube tray through which the muon passed. The mid point of this channel is used as the track co-ordinate although the muon could have passed anywhere within the channel and the discrepancy between the centre of the channel and the true trajectory is the uncertainty in track location.

The distribution of these discrepancies has been found by simulating the tracks of 10,000 randomly positioned muons in a flash-tube tray with an angular distribution corresponding to the 7° triangular zenith angle acceptance function. The channel width of the flash-tube configuration at the angle of the track was defined for each track and the discrepancy between its mid point and the original track was calculated. The resulting distribution of the discrepancies is shown in figure 5.10. The standard deviation of this distribution is the location accuracy in each tray and this is 0.318 ± 0.002 mm.

5.4.3 The Maximum Detectable Momentum

The m.d.m. can now be calculated using the result of the previous section and equation 5.8. The m.d.m. which is applicable to a particular muon depends upon which trays were used to define its trajectory and consequently the m.d.m. has been calculated for all the various tray combinations. The term H/l in equation 5.8 reflects the effect that the gaps between the magnet blocks have on the measured momentum and it is more precisely the ratio of the true to the observed momentum. This latter ratio has been calculated for all the tray combinations in section 5.6.1 and these values, at a zenith angle of 2° (the mean incident angle), have been substituted into equation 5.8 for H/l when calculating the m.d.m.

Table 5.3 contains the m.d.m. for the various tray combinations. It can be seen that when all five trays are used to determine the momentum, MARS has a m.d.m. of 5427 ± 136 GeV/c and it is concluded that the spectrograph will be capable of determining the cosmic ray muon momentum spectrum accurately to beyond 5000 GeV/c.

5.5 The Accuracy of the Azimuthal and Zenith Angles

It was stated in Chapter 3 that only the mean points of the discharged tubes in the azimuthal trays are used to calculate the azimuthal angle of the muon. The flash-tubes in these trays and their configuration are identical to those of the momentum trays and the latter trays place the trajectory of a muon into cells which are 5 mm wide. The uncertainty in track location in the momentum trays is the discrepancy between the true position of the trajectory and the mid point of the cell and the standard deviation of all possible trajectories around the centre of the cell is given by

$$\left(\frac{1}{0.5} \int_{-0.25}^{0.25} x^2 dx \right)^{\frac{1}{2}} = 1.44 \text{ mm.}$$

If it is assumed that a comparable location accuracy can be achieved in the azimuthal

Table 5.3

The Maximum Detectable Momentum of the Various Tray Combinations

Trays used	M.D.M. (GeV/c)
All trays	5427 $\pm$ 136
1235	5162 $\pm$ 129
1345	5094 $\pm$ 128
1245	4392 $\pm$ 110
1234	3075 $\pm$ 77
2345	2749 $\pm$ 69
135	4705 $\pm$ 117
125	3543 $\pm$ 89
145	3329 $\pm$ 83
124	2481 $\pm$ 62
134	2472 $\pm$ 62
245	2276 $\pm$ 57
235	2110 $\pm$ 53
345	1346 $\pm$ 34
123	1210 $\pm$ 30
234	1111 $\pm$ 28

trays, then, because the azimuthal trays are separated by 45.85 cm, the uncertainty in the azimuthal angle is 0.26°.

The zenith angle is defined as the angle between the vertical and the muon's trajectory at level 5 and it is calculated using equation 3.5. The uncertainty, $\Delta\theta$, in this angle due to track location uncertainties of Δy at each measuring level is given by

$$\Delta\theta = \left(\left(2.x_5 . \frac{\partial a}{\partial y} \right)^2 + \left(\frac{\partial b}{\partial y} \right)^2 \right)^{\frac{1}{2}} \Delta y .$$

$\partial a/\partial y$ has been calculated in section 5.4.1 and b is defined as

$$b = \frac{\Sigma x^4(\Sigma y \Sigma x - N \Sigma xy) + \Sigma x^2 (\Sigma xy \Sigma x^2 - \Sigma y \Sigma x^3) + \Sigma x^2 y (N \Sigma x^3 - \Sigma x \Sigma x^2)}{\Sigma x^4((\Sigma x)^2 - N \Sigma x^2) + \Sigma x^3 (N \Sigma x^3 - \Sigma x \Sigma x^2) - \Sigma x^2(\Sigma x^3 \Sigma x - (\Sigma x^2)^2)}$$

hence $\frac{\partial b}{\partial y} = \left(\overset{N}{\underset{i=1}{\Sigma}} \left(\frac{\partial b}{\partial y_i} \right)^2 \right)^{\frac{1}{2}}$.

Simplifying the resulting equations with the approximation that $\Sigma x = \Sigma x^3 = 0$ we obtain $\partial b/\partial y = (\Sigma x^2)^{-\frac{1}{2}}$. When the trajectory is fitted to all five trays $\partial a/\partial y = 10^{-5} m^{-2}$ and $\partial b/\partial y = 0.204 m^{-1}$, hence, with a track location accuracy of 0.318 mm, the uncertainty in the zenith angle is 0.0035°.

5.6. The Corrections to be Applied to the Computed Momentum and Zenith Angle

5.6.1 The Effect of the Gaps between the Magnet Blocks

When the parabola is fitted to the track co-ordinates, it is assumed that the spectrograph is a continuum of iron rather than a multilayer device. Consequently, the $\int B.dl$ of equation 2.2 is overestimated and hence the momentum is likewise. The relationship between the true and observed momentum has been calculated precisely for the momentum range 10 - 5000 GeV/c. A computer has been used to simulate the trajectory of a muon of known momentum through the spectrograph and to recalculate the muon's momentum from the coefficients of the parabola fitted to the co-ordinates of the trajectory at the measuring levels. The energy loss of the muon was neglected. Figure 5.11
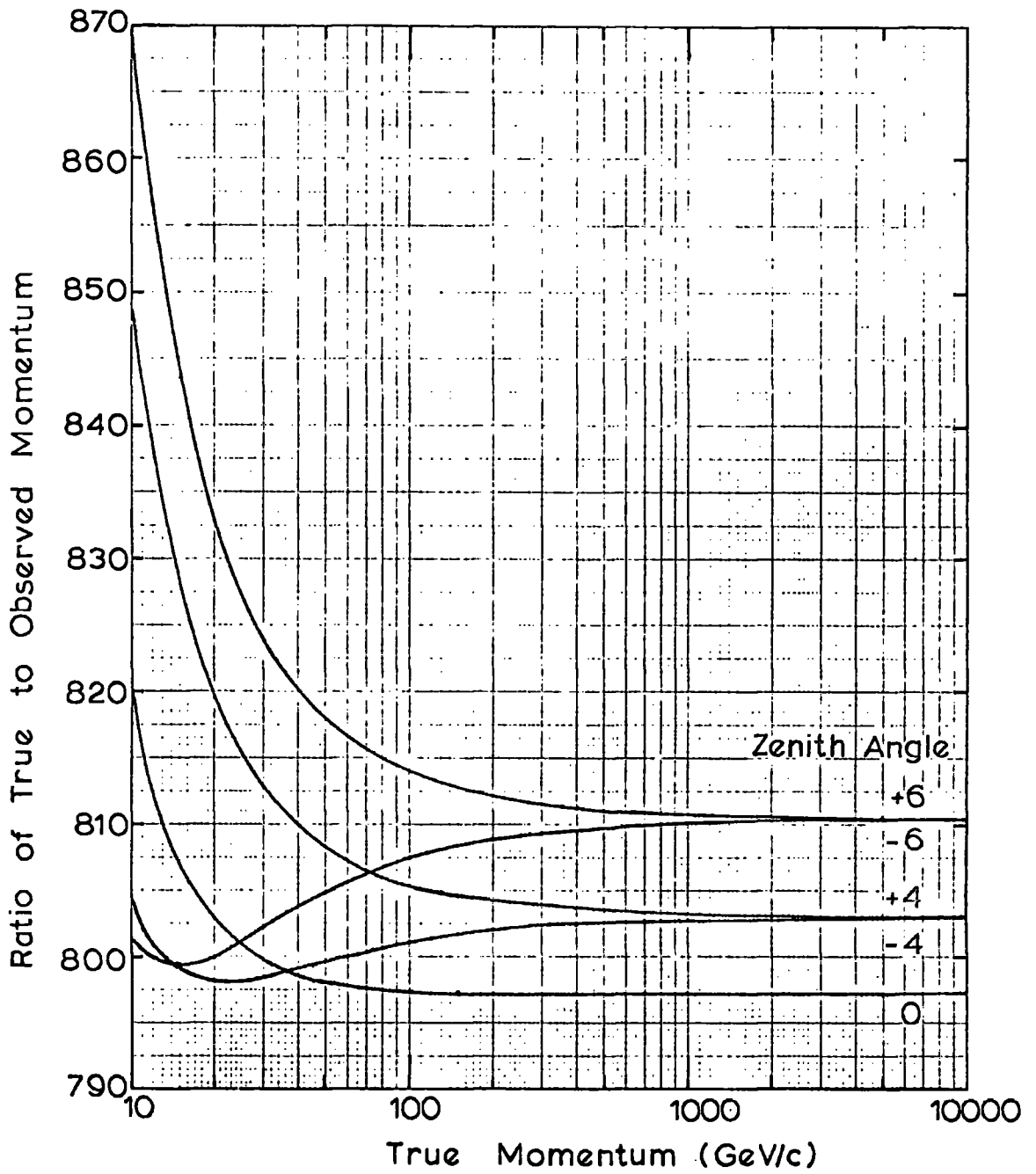
Figure 5.11 The Correction for the Gaps between the
Magnet Blocks.

shows the ratio of the true to the observed momentum as a function of the true momentum for various zenith angles. The sign of the zenith angle shown in this figure is not that derived from the parabola's coefficients but the product of this, the magnetic field direction and the sign of the charge of the muon. This is because the path length of a muon through the spectrograph is a function of the zenith angle and the direction of curvature of its trajectory. As would be expected, this is more important at low momenta where curvature is largest.

The value of the ratio of the true to the observed momentum used by the analysis programme is that for a zenith angle of 0°, namely 0.7972. The momenta of muons at other zenith angles have to be corrected accordingly, but as can be seen from figure 5.11, this only amounts to a correction of $\sim 1.3\%$ for muons with momenta above 100 GeV/c even at a zenith angle of 6°.

The corrections become more important when not all of the five measuring trays are used to define the trajectory. Table 5.4 contains the correction factors for the various tray combinations at zenith angles of 0° and $\pm 6^o$ by which the computed momentum must be multiplied. Once again it is apparent that the correction factors become practically constant at momenta above 100 GeV/c.

It is concluded that all that is required to correct the computed momentum for the effects of the gaps between magnet blocks is a simple correction factor and that this justifies the method of trajectory reconstruction described in Chapter 3.

5.6.2 Energy Loss

The computed momentum must also be corrected for the energy lost by the muon in the spectrograph. The total thickness of absorber in MARS is 3970 ± 21 gm.cm^{-2} and the rate of energy loss of the muons was calculated from the equations of Sternheimer and Peierls, which are given in Chapter 7. An additional correction for energy loss due to pair production, bremsstrahlung and nuclear interactions was also included and this amount to 4×10^{-6}.E MeV/(gm.cm^{-2}) (after Hayman et al.

Table 5.4

The Corrections for the Gaps between the Magnet Blocks for the Various Tray Combinations Relative to that for All Trays

Momentum (GeV/c)	Zenith Angle (°)	Tray Combination														
		1234	1235	1245	1345	2345	123	124	134	234	125	135	235	145	245	345
10	-6	1.012	1.004		1.006	1.016	0.916	0.981	1.041	1.116	0.981		1.052	0.982	0.983	0.933
	0	1.002	1.002	0.982	1.008	1.027	0.898	0.968	1.034	1.117	0.975	1.013	1.060	0.990	0.998	0.952
	+6	0.992	1.000		1.010	1.040	0.881	0.955	1.027	1.119	0.968		1.068	0.998	1.014	0.973
20	-6	1.015	1.005		1.004	1.011	0.924	0.986	1.042	1.113	0.984		1.048	0.980	0.978	0.928
	0	1.011	1.004	0.982	1.006	1.017	0.916	0.979	1.039	1.114	0.981	1.013	1.051	0.984	0.985	0.937
	+6	1.006	1.003		1.007	1.023	0.907	0.973	1.035	1.114	0.978		1.055	0.988	0.992	0.946
50	-6	1.015	1.005		1.004	1.012	0.923	0.985	1.042		0.984		1.048	0.981	0.979	0.929
	0	1.013	1.004	0.982	1.005	1.014	0.920	0.983	1.040	1.113	0.982	1.013	1.049	0.982	0.982	0.933
	+6	1.011	1.004		1.006	1.016	0.916	0.980	1.039		0.981		1.051	0.983	0.985	0.937
100	-6	1.014	1.005			1.013	0.922	0.984	1.041		0.983		1.048	0.981	0.880	0.930
	0	1.013	1.004	0.982	1.005	1.014	0.921	0.983	1.041	1.112	0.982	1.013	1.049	0.982	0.981	0.932
	+6	1.012	1.004			1.014	0.919	0.982	1.040		0.982		1.050	0.982	0.983	0.934
200	-6	1.014				1.013	0.922	0.984							0.980	0.930
	0	1.013	1.004	0.982	1.005	1.013	0.921	0.983	1.041	1.112	0.983	1.013	1.049	0.982	0.981	0.932
	+6	1.012				1.014	0.919	0.983							0.982	0.934

1963). The trajectories of muons were simulated through the spectrograph for various values of momentum and zenith angle and with the corresponding rate of energy loss. Scattering was neglected. A parabola was then fitted to the co-ordinates of the trajectory at the measuring levels and the effective momentum calculated for all tray combinations with the momentum correction factor of 0.7972,

Table 5.5 contains the discrepancy between the incident and computed momenta as a function of incident momentum, zenith angle (as defined in the previous section), and tray combination. It is apparent that, as would be expected, the energy loss is only important below 100 GeV/c and it is fairly independent of zenith angle. The corrections given in the table are fairly constant at low values of momentum because of the domination of energy loss and what fluctuations there are can be accounted for by the extrapolation of the momentum computed for the tray combination to the momentum of the muon at the top of the spectrograph. At higher momenta, where energy loss is less important, the variation in path length (and hence the momentum correction factor) with zenith angle accounts for the fluctuations in the corrections.

5.6.3 The Corrections to be Applied to the Computed Momentum

The momentum of all muons is corrected by the analysis programme for the effect of the gaps between the magnet blocks using the factor for a muon with a momentum of 1000 GeV/c, a zenith angle of 0° and when a trajectory is fitted to all five trays, namely 0.7972. This correction is only approximately true for other tray combinations, momenta and zenith angles. However, the energy loss corrections tabulated in table 5.5 have also been calculated using this correction factor and consequently they contain any necessary re-adjustment factors. Hence the muon's incident momentum can be calculated from the computed momentum by the simple addition of the appropriate correction contained in table 5.5.

Table 5.5

The Corrections to be Added to the Computed Momenta

Momentum (GeV/c)	Zenith angle (θ)	Tray Combination															
		12345	1234	1235	1245	1345	2345	123	124	134	234	125	135	235	145	245	345
10	-6	5.3	6.1	5.5	5.5	5.1	3.6	7.2	6.5	5.6	4.0	6.1	5.2	3.7	4.9	3.4	3.0
	0	4.8	5.5	4.9	4.9	4.5	3.1	6.7	5.9	5.1	3.5	5.5	4.7	3.3	4.1	3.0	2.7
	+6	4.5	5.2	4.6	4.6	4.2	3.0	6.3	5.6	4.7	3.3	5.1	4.3	3.1	3.8	2.8	2.6
20	-6	5.0	5.8	5.2	5.3	4.7	3.5	8.0	6.6	5.1	3.1	6.0	4.8	3.3	4.5	3.6	3.8
	0	4.4	5.1	4.5	4.7	4.1	2.9	7.3	5.8	4.4	2.3	5.3	4.1	2.7	3.9	3.0	3.3
	+6	4.3	4.9	4.3	4.5	4.0	2.9	7.1	5.6	4.2	2.3	5.1	4.0	2.6	3.8	3.1	3.4
50	-6	5.5	6.0	5.5	6.3	5.0	3.6	11.0	7.6	4.5	0.4	7.0	4.9	2.4	5.5	4.7	6.4
	0	4.3	4.7	4.3	5.1	3.9	2.5	9.8	6.4	3.2	-0.9	5.8	3.7	1.3	4.4	3.6	5.4
	+6	4.7	5.0	4.7	5.5	4.3	3.0	9.9	6.6	3.5	-0.5	6.1	4.1	1.7	4.8	4.2	6.0
100	-6	6.4	6.2	6.2	8.0	5.7	3.8	15.8	9.4	3.4	-4.3	8.7	5.1	0.9	7.2	6.4	10.6
	0	4.4	4.1	4.2	6.1	3.7	1.9	13.8	7.3	1.2	-6.5	6.7	3.1	-1.1	5.3	4.6	8.9
	+6	5.6	5.3	5.3	7.2	4.9	3.2	14.7	8.4	2.4	-5.1	7.8	4.3	0.2	6.6	5.9	10.1
200	-6	8.0	6.6	7.4	11.4	6.8	4.1	25.2	12.7	1.0	-13.7	12.1	5.5	-2.3	10.7	9.9	18.9
	0	4.4	2.9	3.7	7.9	3.2	0.5	21.7	9.0	-2.8	-17.7	8.5	1.9	-6.0	7.2	6.5	15.7
	+6	7.2	5.6	6.6	10.6	6.1	3.5	24.2	11.7	0.1	-14.5	11.2	4.7	-2.9	10.0	9.5	18.5
500	-6	13.0	7.7	11.1	21.6	10.2	5.1	53.5	22.7	-6.0	-44.8	22.2	6.6	-11.7	21.0	20.4	43.9
	0	4.5	-1.0	2.5	13.3	1.7	-3.4	45.5	14.2	-14.9	-51.3	13.8	-2.0	-20.5	12.7	12.2	36.1
	+6	12.2	6.7	10.3	20.9	9.5	4.5	52.5	21.7	-6.9	-42.7	21.3	5.8	-12.4	20.4	20.0	43.5
1000	-6	21.2	9.4	17.1	38.6	15.9	6.7	101.	39.2	-17.8	-88.9	38.9	8.4	-27.5	38.2	37.9	85.5
	0	4.5	-7.6	0.4	22.2	-0.8	-10.1	85.1	22.7	-35.2	-107.	22.4	-8.5	-44.9	21.9	21.6	70.1
	+6	20.4	8.3	16.3	27.8	15.2	6.1	99.5	38.2	-18.7	-89.8	38.0	7.6	-28.1	37.6	37.4	85.2
5000	-6	86.5	22.3	65.2	173.	60.8	19.1	476.	171.	-112.	-466.	172.	22.4	-154.	176.	177.	418.
	0	4.4	-60.9	-17.2	93.1	-21.6	-64.0	401.	89.9	-198.	-557.	91.5	-60.8	-240.	95.0	96.8	342.
	+6	85.7	21.3	64.4	173.	60.1	18.5	476.	170.	-113.	-467.	171.	21.6	-155.	175.	177.	418.

The above corrections to the computed momentum allow for the systematic biases of the spectrograph and the method of data analysis. However, the momentum of any muon can never be determined absolutely, because finite uncertainties are introduced into its value by Coulomb scattering and the m.d.m. of the particular tray combination being used. The uncertainty due to Coulomb scattering amounts to 12% of the momentum of the muon and it is independent of momentum (see section 2.2.2) whereas the m.d.m. introduces an uncertainty into the momentum, p, of p/(m.d.m.) and hence this increases with momentum.

5.6.4 The Corrections to be Applied to the Computed Zenith Angle

The true and computed zenith angles were compared for the simulated muon trajectories of section 5.6.2 and table 5.6 contains the results. The discrepancy between the two angles is tabulated as a function of tray combination, momentum and true zenith angle. The sign of the zenith angle and the corrections apply to a positively charged muon in positive magnetic field. For any other condition the sign of the zenith angle to be used is the product of the signs of the computed zenith angle, the muon's charge and the magnetic field direction. It can be seen that the computed zenith angle is very close to the true angle for all tray combinations above a momentum of 50 GeV/c but below this value, the corrections become increasingly important.

5.7 Programme Diagnostics

The time that it takes the programme to analyse one event depends upon how many track fitting options have to be tried before the fitting criteria are satisfied and also upon the number of tubes in the groups. The minimum time taken for a five tray fit is 8 secs/event but the average time taken to analyse an event is about 30 secs. Consequently, the overnight analysis of the data collected in a 24 hour period (500 events) will only consume 4 of the 11 hours available.

Table 5.6

The Corrections to be Added to the Computed Zenith Angles (in Degrees)

Momentum (GeV/c)	True Zenith Angle	Tray Combination															
		12345	1234	1235	1245	1345	2345	123	124	134	234	125	135	235	145	245	345
10	-6	-3.4	-7.2	-3.7	-3.9	-2.4	-0.76	-17.5	-9.5	-4.8	-1.6	-5.7	-2.7	-0.97	-1.0	-0.49	-0.38
	0	-2.7	-5.5	-2.9	-3.1	-1.9	-0.60	-13.5	-7.3	-3.7	-1.2	-5.4	-2.1	-0.74	-0.83	-0.41	-0.32
	+6	-2.2	-4.5	-2.4	-2.5	-1.5	-0.48	-11.1	-6.0	-3.0	-0.9	-3.7	-1.7	-0.59	-0.70	-0.35	-0.28
20	-6	-0.31	-0.65	-0.34	-0.40	-0.19	-0.03	-2.0	-1.0	-0.34	0.07	-0.58	-0.21	0.0	-0.11	-0.06	-0.07
	0	-0.26	-0.55	-0.28	-0.34	-0.15	0.0	-1.8	-0.83	-0.26	0.11	-0.50	-0.17	0.02	-0.09	-0.04	-0.06
	+6	-0.22	-0.47	-0.23	-0.30	-0.12	0.10	-1.6	-0.73	-0.20	0.15	-0.44	-0.13	0.04	-0.08	-0.03	-0.05
50	-6		0.03		-0.03	0.01		-0.34	-0.10	0.04	0.13	-0.05	0.02				
	0	0.0	0.02	0.0	-0.03	0.02	0.04	-0.31	-0.08	0.05	0.14	-0.04	0.02	0.06	0.0	0.01	-0.01
	+6		0.01		-0.02	0.02		-0.30	-0.07	0.06	0.14	-0.04	0.03				
100	-6		0.01					-0.12				0.01					
	0	0.01	0.02	0.01	0.0	0.02	0.02	-0.11	-0.01	0.04	0.08	0.0	0.02	0.04	0.01	0.01	0.0
	+6		0.02					-0.11				0.0					
200	-6																
	0	0.0	0.01	0.0	0.0	0.01	0.01	-0.02	0.0	0.01	0.02	0.0	0.01	0.01	0.0	0.0	0.0
	+6																

The maximum amount of data which can be analysed at any one time is determined by the amount of disc space available. There are usually about 1000 sectors available on a disc, but as there must be sufficient space for the answer file created by the programme, only about 600 sectors can be used for data storage. This is equivalent to about 2800 events, or 6 days worth of data, and this would take about 24 hours to analyse. It is thus feasible to analyse the data for a whole week over the week-end rather than nightly.

5.8 Conclusions

The investigations of the properties of the flash-tube track location technique presented in this chapter provide conclusive evidence that the technique correctly interprets the flash-tube configurations and it correctly allows for tube inefficiencies and knock-on electrons. This is particularly true of the results of the mean layer efficiencies of the options, where the theoretical and experimental values agree exceedingly well, and also, to a somewhat lesser extent, true of the correlation between the theoretical and experimental values for the frequency of occurrence of the options. It is also concluded that the uncertainties in the absolute tube positions and their internal diameters are allowed for by increasing the geometrical tube diameters and gaps between the tubes by 10%

The track location accuracy of 0.318 mm achieved in the measuring trays gives MARS an m.d.m. of 5427 $\pm$ 136 GeV/c and this will enable the muon momentum spectrum to be determined precisely to beyond 5000 GeV/c.

It has been shown that the programme as a whole is easily capable of handling all the data from MARS and it is concluded that the programme and flash-tube track location technique satisfactorily meet the requirements of the experiment.

CHAPTER 6.

A Preliminary Measurement of the Muon Momentum Spectrum & Charge Ratio

6.1 Introduction

During the construction of MARS when the computer link was incomplete, a stage was reached when it was possible to record photographically the measuring tray flash-tubes of one side of the spectrograph. These data which were all analysed by the programme described earlier were to serve as a source for a preliminary measurement of the cosmic ray muon momentum spectrum and charge ratio. They also provided real data with which to test and investigate the properties of the analysis programme. The former work was presented at the International Conference on Cosmic Rays at Hobart, Tasmania, 1971.

6.2 Details of the Experiment

The experimental arrangement was the same as that shown in figure 2.3 except that the measuring tray and scintillator at level 1 were reversed and the measuring and momentum selector trays at level 5 were likewise. The measuring trays (with their digitisation electronics and probes removed) were used to locate the trajectories of muons traversing the spectrograph. Fiducial lights were attached to the fronts of the trays and a mirror system was constructed which enabled the recording of all five trays on one photographic frame of a camera situated at level 3. A clock and an information board were included in the field of view of the camera and it was ensured that the camera looked down the axes of the tubes so that maximum luminosity would be achieved.

Delay lines were used to generate the high voltage pulses for the flash-tube trays. These were discharged with a spark gap through a resistor which had the characteristic impedance of the delay lines $(37 \, \Omega)$ and the pulses to the flash-tube trays were taken from across these resistors. The actual pulses were of $2 \mu s$ duration and of 6kV amplitude. The latter pulse parameter was variable and the value used was determined by a series of voltage flash-tube efficiency measurements.

The trays were made parallel to one another to within 0.5mm by means of two plumb bobs down the side of the spectrograph at either ends of the trays. The approximate co-ordinates of the trays relative to the plumb bobs were also measured. More precise co-ordinates for the tray positions were provided by data from a zero magnetic field run, details of which are given below.

The spectrograph was triggered by a three fold coincidence from the scintillators and, $2\mu s$ later, the high voltage pulse was applied to the trays, the images of the discharging tubes being recorded on the film. There then followed a 4 second paralysis period during which time the fiducials, clock and information board were illuminated and the film in the camera wound on to the next frame.

Altogether, 10,000 events with zero magnetic field were recorded and 50,000 events with a field of 16.3 $\pm$ 0.1 k gauss. The latter events were divided equally between positive and negative magnetic field directions to remove any experimental bias.

Plate II shows a typical event recorded on the film. A positive muon with a momentum of 29.1 GeV/c is shown, which was accompanied by a burst at level 4.

6.3 The Transfer of the Data to the Computer

All the data were analysed by the programme and techniques described in the earlier chapters and consequently, the data had to be presented to the programme in an identical form to that which is received from the on-line system. This was accomplished by first transferring the film data onto paper tape at a scanning table and then interpreting this tape with a special programme on the computer which placed the data on a disc in the correct format.

Each event was projected onto a diagram of the flash-tube tray patterns of all five trays. The positions of the fiducial lights were also marked so that the tubes which discharged could be identified. The flash-tube information and the time of the event were then transferred onto paper tape as described below.
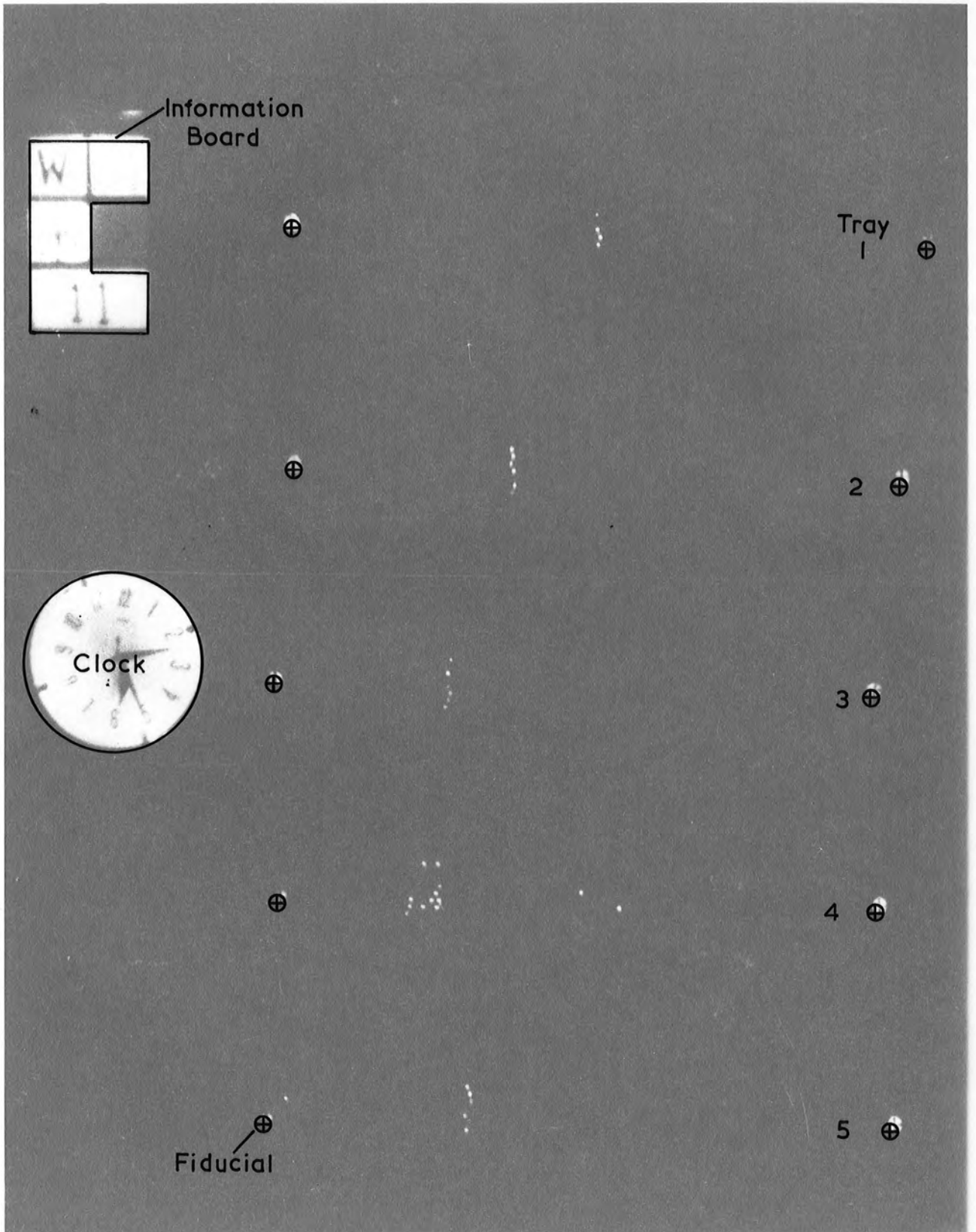
Plate II.   A Typical Film Event.

Those events which would obviously be rejected by the analysis programme, e.g. those due to air showers etc., were not entered onto the tape.

The paper tape device consisted of two panels into which data could be entered, and a paper tape punch. One panel consisted of a matrix of 40 buttons representing a portion of a tray and including five columns of tubes. These buttons remained illuminated once depressed and the flash-tube configuration of a block of tubes containing the muon's track in a tray was entered into this panel. The other panel contained facilities for entering the number of the flash-tube tray and the flash-tube column number of the start of the block of tubes. The time of the event from the clock was also entered into this panel. All of this information was then punched onto the tape for each tray except the time which was only entered once for each event.

All the tracks contained in any one tray were punched on the tape with the proviso that a maximum of 15 columns (3 blocks) could be punched for any tray. This limitation occasionally required the scanner to interpret and edit the data but as this only occured when the trays contained more than three well spaced tracks or a large burst, both of which would be ignored by the analysis programme, it is not thought to have introduced any bias into the data.

The data on the tape was carefully checked by the translation programme for internal consistency. Header information, dummy columns and azimuthal trays were attached to those events which were found to be consistent and they were then stored on the disc. The header information contained an event number assigned to the event, the date and the time of the event, and the direction of the magnetic field. Artificial bursts were placed in the azimuthal trays rendering them incapable of being analysed.

A data file identical in format to that produced by the on-line system was thus generated and this file was then analysed by the programme described in earlier chapters. After analysis, the data and answers were transferred to magnetic tape in Newcastle where they were subsequently studied.

6.4   The Zero Magnetic Field Data

One thousand of the events recorded without a magnetic field were scanned and analysed with the zero field analysis programme described in Chapter 4. Briefly, a straight line was drawn between the tracks located at levels 1 and 5 and the discrepancy between this line and the track co-ordinates at each of the other three levels calculated. Of the 1,000 words scanned, 700 events were finally used to define the tray positions. The remainder were rejected because of the presence of air showers and spurious events and because of the condition that the track had to be unambiguously defined in levels 1 and 5.

The histograms of the discrepancies for trays 2, 3 and 4 are shown in figure 6.1 (a), (b) and (c) respectively. The differences in the widths of the three distributions reflect the effects of scattering, energy loss and the anchoring of the reference line at levels 1 and 5. The approximate co-ordinates for trays 2, 3 and 4 used by the analysis programme were corrected by the mean values of the respective histograms to give the final tray co-ordinates for the analysis of the magnetic field data.

The uncertainty in the positions of trays 2, 3 and 4 from the histograms and the location uncertainty in levels 1 and 5 of 0.32mm leads to an m.d.m. for the film data of 2500 GeV/c.

6.5.   The Magnetic Field Data

A total of 7081 events were analysed and the momenta of the muons, their zenith angles and the signs of their charges were determined by the programme described in earlier chapters. To remove any experimental bias, the events were selected, as far as possible, equally from the data for the two directions of the magnetic field. The final totals were 3611 muons with a positive field and 3470 with a negative field. These data were used to calculate the differential momentum spectrum and charge ratio for the muons.
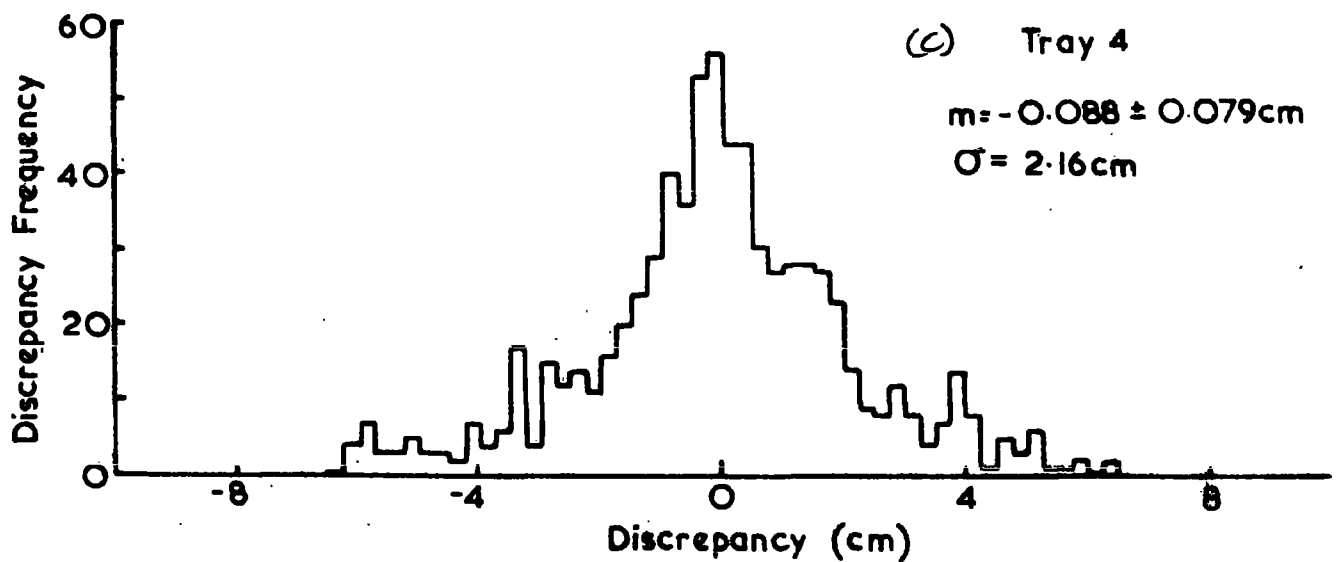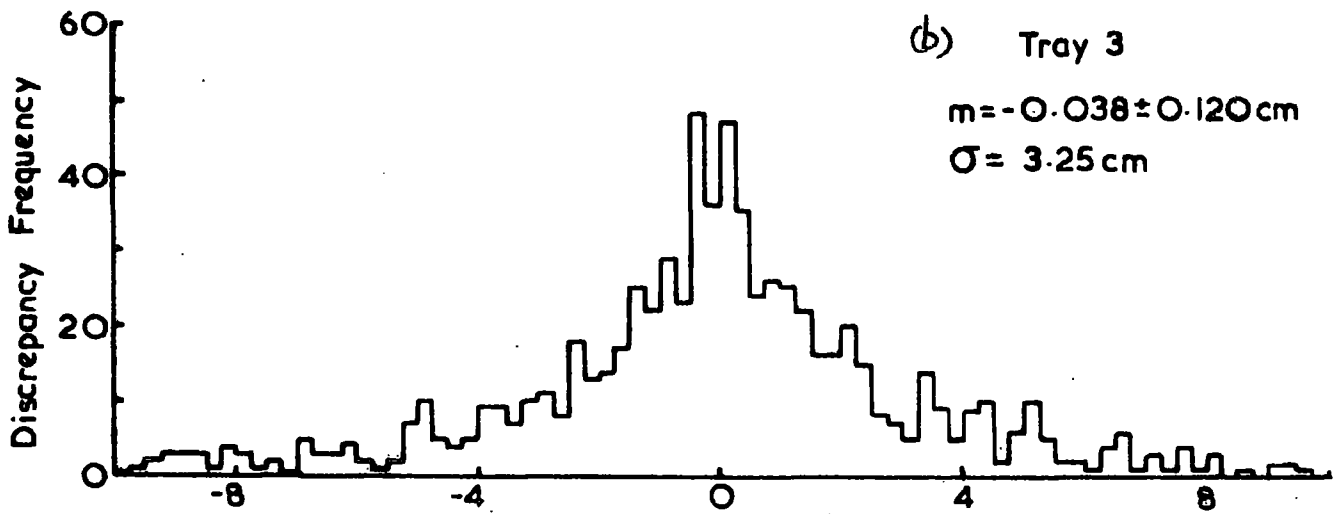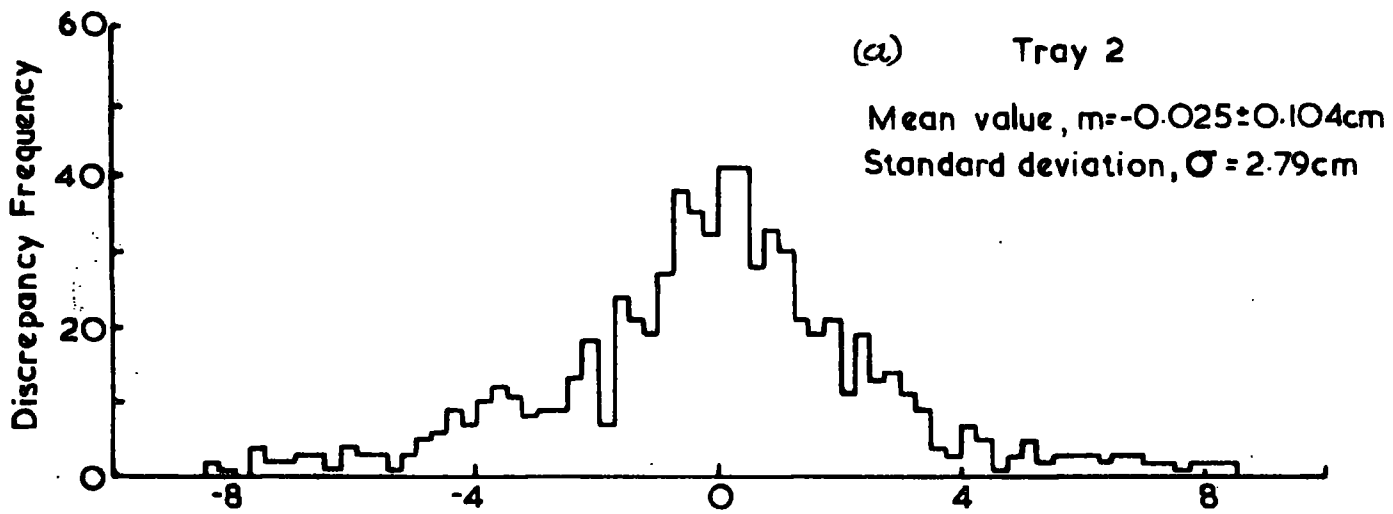
Figure 6.1 The Tray Position Histograms.

6.6. The Differential Momentum Spectrum at Sea Level in the Vertical Direction

The differences in the position of some of the particle detectors in the spectrograph to those shown in figure 2.3 necessitated the recalculation of the corrections for energy loss and for the gaps between the magnet blocks. The value for the latter correction used by the analysis programme was 0.8083 and table 6.1 contains the energy loss corrections to be added to the computed momenta.

The data were first corrected for energy loss by the amount defined by the tray combination used and given in Table 6.1. They were then divided into momentum cells whose mean momenta and cell widths are given in Table 6.2. Data were available for muons with an incident momentum between 7 and 10 GeV/c but, due to uncertainties in the cell width and the acceptance of the spectrograph at these momenta and also because of the relatively large energy loss and the poorness of the parabola fit at these exceptionally low momenta, these data were neglected.

An attempt was made to minimise the effects on the derived spectrum of noise in the data. A measure of the 'goodness of fit' of each track was available in that the standard deviation of the track co-ordinates around the fitted parabola was calculated for each event. The distributions of these deviations were studied for each momentum cell. These distributions are in fact r.m.s. distributions and as such do not conform to the normal properties of gaussian distributions. A study was made of an r.m.s. distribution simulated by fitting a parabola to five points which had been individually displaced from a straight line by an amount randomly selected from a gaussian distribution. The distribution of the standard deviations of the points around the fitted trajectories for 10,000 simulations is shown in figure 6.2. It was found that to chop the distribution at three times its mean value was almost equivalent to chopping a gaussian distribution at three standard deviations. This

Table 6.1

The corrections for energy loss and the tray combination to be added to the computed momentum (GeV/c)

Momentum (GeV/c)	Zenith Angle (°)	Tray Combination															
		54321	4321	5321	5421	5431	5432	321	421	431	432	521	531	532	541	542	543
10	−6	5.3	6.2	5.5	5.4	5.0	3.4	7.2	6.5	5.7	4.0	6.0	5.2	3.7	4.6	3.2	2.8
	0	4.7	5.6	4.9	4.8	4.5	3.0	6.7	6.0	5.1	3.5	5.5	4.6	3.2	4.0	2.8	2.5
	+6	4.4	5.2	4.6	4.5	4.2	2.8	6.3	5.6	4.8	3.3	5.1	4.3	3.0	3.8	2.7	2.4
20	−6	4.9	5.9	5.1	5.1	4.6	3.3	7.9	6.5	5.2	3.1	5.8	4.8	3.2	4.3	3.4	3.5
	0	4.2	5.1	4.4	4.4	4.0	2.7	7.2	5.8	4.4	2.4	5.1	4.1	2.6	3.7	2.8	3.0
	+6	4.1	5.0	4.3	4.3	3.9	2.8	6.9	5.6	4.3	2.3	5.0	4.0	2.6	3.7	2.9	3.1
50	−6	5.3	6.0	5.3	5.9	4.9	3.5	10.5	7.4	4.5	0.4	6.6	4.8	2.4	5.1	4.2	5.6
	0	4.1	4.7	4.2	4.7	3.7	2.4	9.3	6.2	3.2	−0.9	5.4	3.6	1.2	4.0	3.2	4.7
	+6	4.5	5.0	4.5	5.1	4.1	2.9	9.4	6.4	3.5	−0.5	5.7	4.0	1.7	4.5	3.7	5.3
100	−6	6.0	6.1	5.8	7.2	5.4	3.7	14.7	8.8	3.3	−4.2	8.0	4.9	1.0	6.5	5.6	9.2
	0	4.0	4.0	3.8	5.3	3.4	1.8	12.7	6.7	1.2	−6.4	6.0	2.9	−1.0	4.6	3.8	7.5
	+6	5.2	5.1	5.0	6.5	4.7	3.2	13.6	7.8	2.4	−5.1	7.1	4.1	0.3	5.9	5.2	8.8
200	−6	7.4	6.3	6.8	9.9	6.4	4.2	22.9	11.5	0.9	−13.6	10.7	5.2	−1.9	9.2	8.4	16.2
	0	3.7	2.6	3.1	6.4	2.8	0.7	19.3	7.8	−2.9	−17.6	7.0	1.5	−5.7	5.7	5.0	12.9
	+6	6.6	5.3	6.0	9.2	5.7	3.7	21.8	10.4	−0.1	−14.5	9.8	4.4	−2.6	8.6	7.9	15.8
500	−6	11.5	6.8	9.7	18.1	9.4	5.7	47.5	19.4	−6.4	−41.7	18.7	5.9	−10.7	17.4	16.7	37.2
	0	3.0	−1.9	1.1	9.7	0.8	−2.8	39.4	10.9	−15.4	−51.2	10.2	−2.8	−19.5	9.1	8.5	29.3
	+6	10.7	5.8	8.9	17.3	8.7	5.1	46.4	18.4	−7.4	−42.6	17.8	5.1	−11.3	16.8	16.3	36.9
1000	−6	18.3	7.5	14.4	31.6	14.3	8.0	88.3	32.6	−18.8	−88.7	32.1	6.9	−25.3	31.1	30.6	72.3
	0	1.6	−9.5	−2.5	15.1	−2.5	−8.7	72.6	16.0	−36.2	−107.3	15.5	−10.0	−42.7	14.7	14.2	56.7
	+6	17.6	6.5	13.6	30.8	13.6	7.5	87.2	31.6	−19.7	−89.6	31.2	6.1	−26.0	30.5	30.1	71.9

Table 6.2

Mean Momentum (GeV/c)	N+	N-	N Total	Cell Width (GeV/c)	Relative Acceptance	N Total	Charge Ratio
11.0	598	466	1064	2	0.550	967.3	1.28 ± 0.08
13.0	440	348	788	2	0.715	551.0	1.26 ± 0.09
14.9	357	285	642	2	0.800	401.3	1.25 ± 0.10
16.9	326	207	533	2	0.860	309.9	1.58 ± 0.14
19.0	242	195	437	2	0.895	244.1	1.24 ± 0.12
22.1	389	306	695	5	0.925	150.3	1.27 ± 0.10
26.6	306	242	548	5	0.950	115.4	1.26 ± 0.11
31.8	201	171	372	5	0.966	77.0	1.18 ± 0.12
36.8	127	107	234	5	0.970	48.2	1.19 ± 0.15
42.2	95	69	164	5	0.980	33.5	1.38 ± 0.21
47.2	88	57	145	5	0.983	29.5	1.54 ± 0.26
52.9	49	34	83	5	0.985	16.9	1.44 ± 0.31
58.0	33	27	60	5	0.987	12.2	1.22 ± 0.30
65.0	60	42	102	10	0.990	10.3	1.43 ± 0.27
75.0	40	41	81	10	0.993	8.20	0.98 ± 0.21
84.0	23	25	48	10	0.995	4.82	0.92 ± 0.25
93.0	20	15	35	10	0.997	3.51	1.33 ± 0.43
119.0	41	33	74	50	1.0	1.48	1.24 ± 0.29
171.0	19	14	33	50	1.0	0.66	)
262.0	9	11	20	200	1.0	0.10	)1.23 ± 0.33
560.0	4	1	5	–	1.0	0.009	)
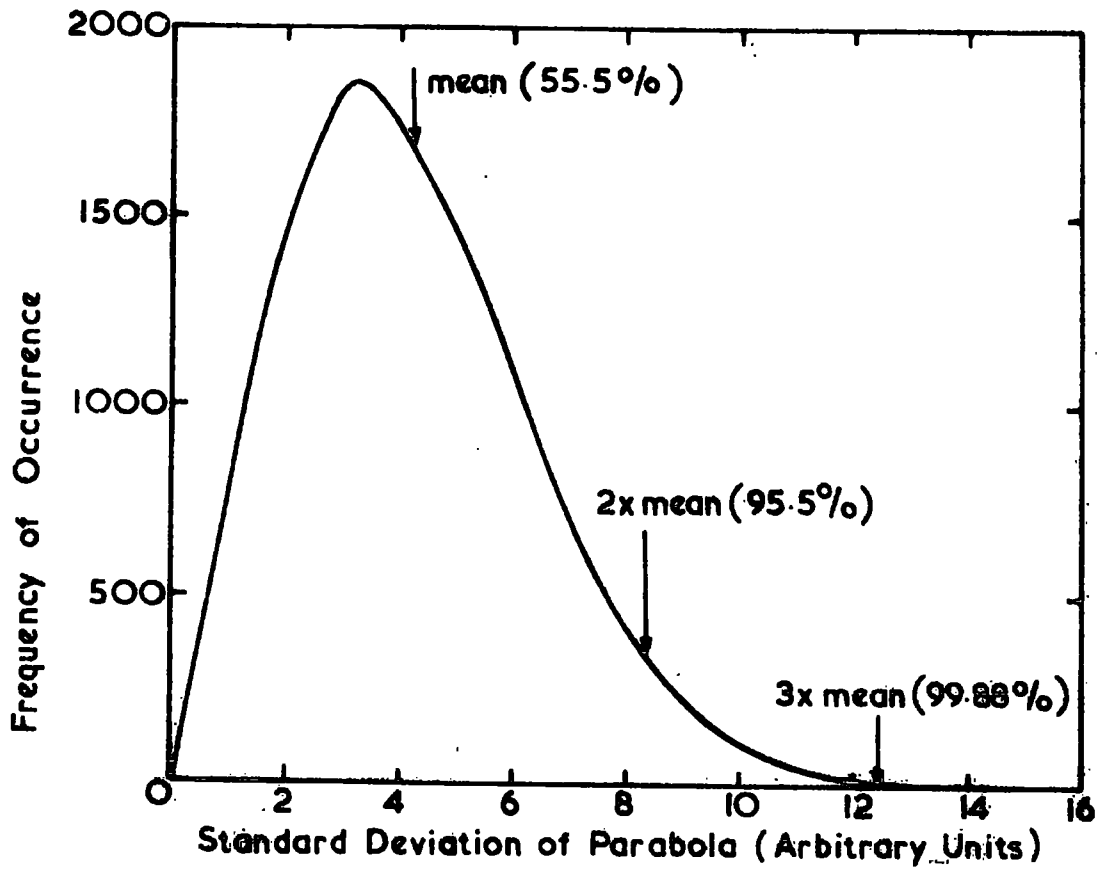
Figure 6.2   An RMS Distribution.
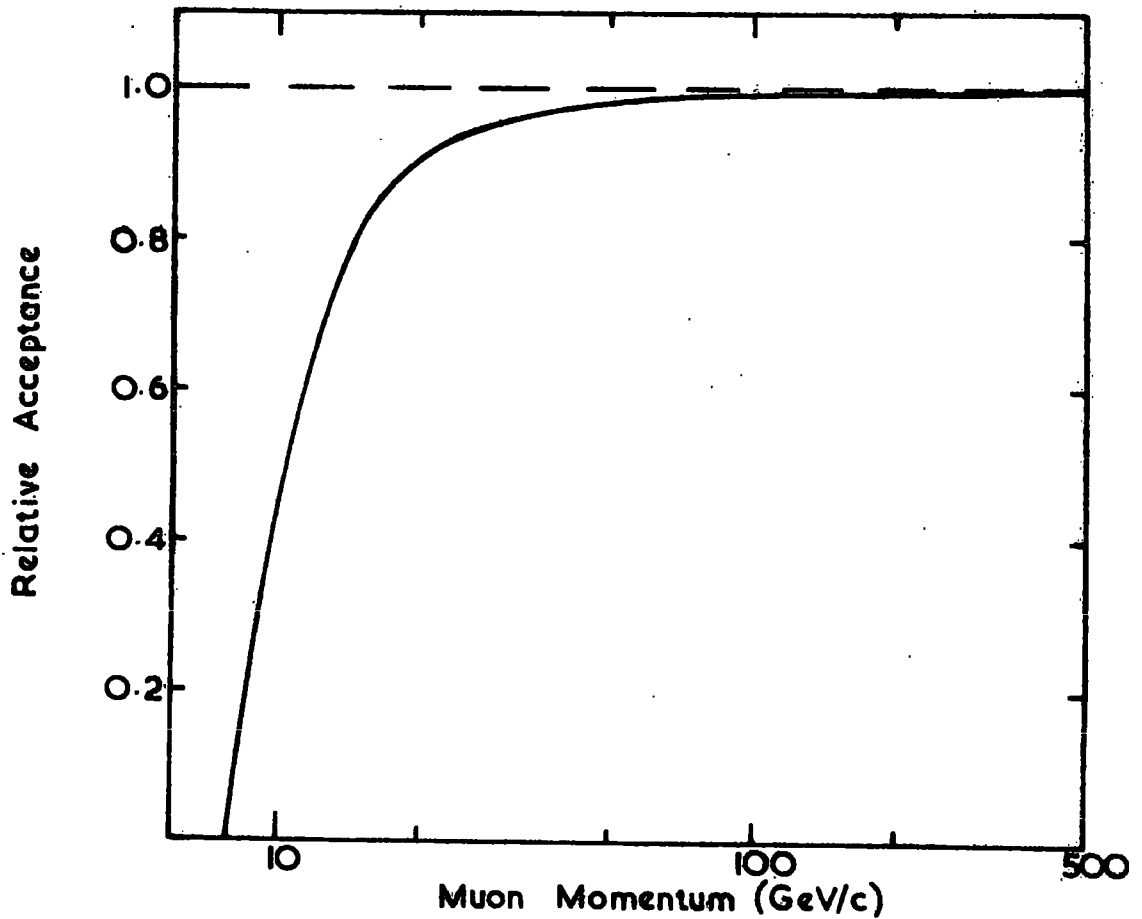
Figure 6.3   The Relative Acceptance of the Spectrograph for the Film Data.

selection criterion was repeatedly applied to the distribution of the standard deviations of the momentum cells until self-consistent distributions were obtained.

The number of positive and negative muons and also the total number of muons remaining in each cell after the application of the selection criterion are shown in Table 6.2. A total of 108 muons were rejected. The acceptance of the spectrograph relative to that at infinite momentum as a function of momentum is shown in figure 6.3. The acceptance for muons of infinite momenta had a value of 426 cm^2sterad. The values of the relative acceptance at the mean momenta of the cells are also shown in Table 6.2. The total number of muons in each cell has been corrected to the acceptance at infinite momentum and unit cell width and the results are also tabulated. The highest momentum cell reflects the integral intensity above 400 GeV/c and consequently its cell width is undefined. Five muons with momenta above 400 GeV/c were observed whereas, from the OPW integral spectrum, 5.6 are expected to occur within the data for the present experiment. The differential intensity for this cell has been plotted at the equivalent OPW differential intensity corrected by 5/5.6.

Since the live time of the spectrograph during the collection of the data was not recorded, no attempt has been made to calculate the absolute muon rates. Instead, the data have been normalised to the differential spectrum, derived from the OPW integral spectrum, at a momentum of 26.6 GeV/c. The experimental data points together with the OPW differential spectrum are given in figure 6.4. It is apparent that the normalised experimental points are in very good agreement with the OPW differential spectrum considering the poor statistical accuracy of the higher nomenta points and the method of the derivation of the spectrum.
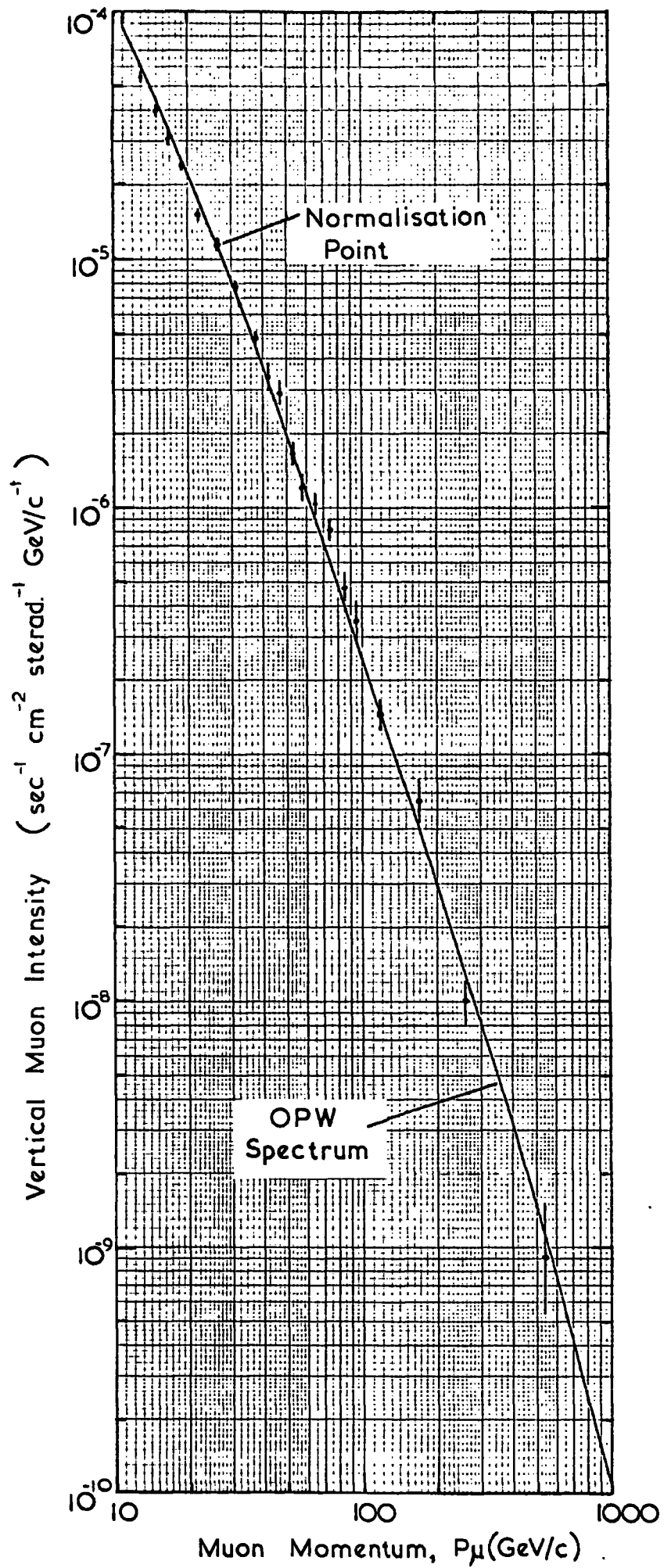
Figure 6.4 The Vertical Muon Differential Momentum Spectrum.

6.7 The Charge Ratio

The charge ratio for the accepted events is shown as a function of momentum in figure 6.5. The last three momentum cells were combined together to improve the statistical accuracy and the resultant charge ratio was plotted at the mean momentum of 210 GeV/c. The broken line on the figure is the mean charge ratio of 1.286 ± 0.026 for all the data.

The results of the world survey of charge ratio measurements presented in figure 1.3 have been combined together into momentum cells and are shown in figure 6.6. It can be seen that the results of the present preliminary experiment are not in disagreement with the combined world survey. It is also apparent that there is evidence for the charge ratio remaining fairly constant over the momentum range 10 - 1,000 GeV/c. However, there are some indications of fine structure in the region above 60 GeV/c but confirmation of this will have to await the better statistics which will become available from spectrographs such as MARS.

6.8 Conclusions

The statistical accuracy of the present experiment is similar to that of previous experiments and confirms the OPW spectrum and previously measured charge ratio to within the experimental uncertainty. This agreement between the present results and those of previous workers indicates that the spectrograph and the analysis programme are performing correctly.

It is of interest to note that all the data analysed were collected during 18 hours of operation of the spectrograph and that they took over 2 months to scan. The necessity of having an automated spectrograph with which to make a precise determination of the muon momentum spectrum and charge ratio beyond 1,000 GeV/c at sea level is very evident.
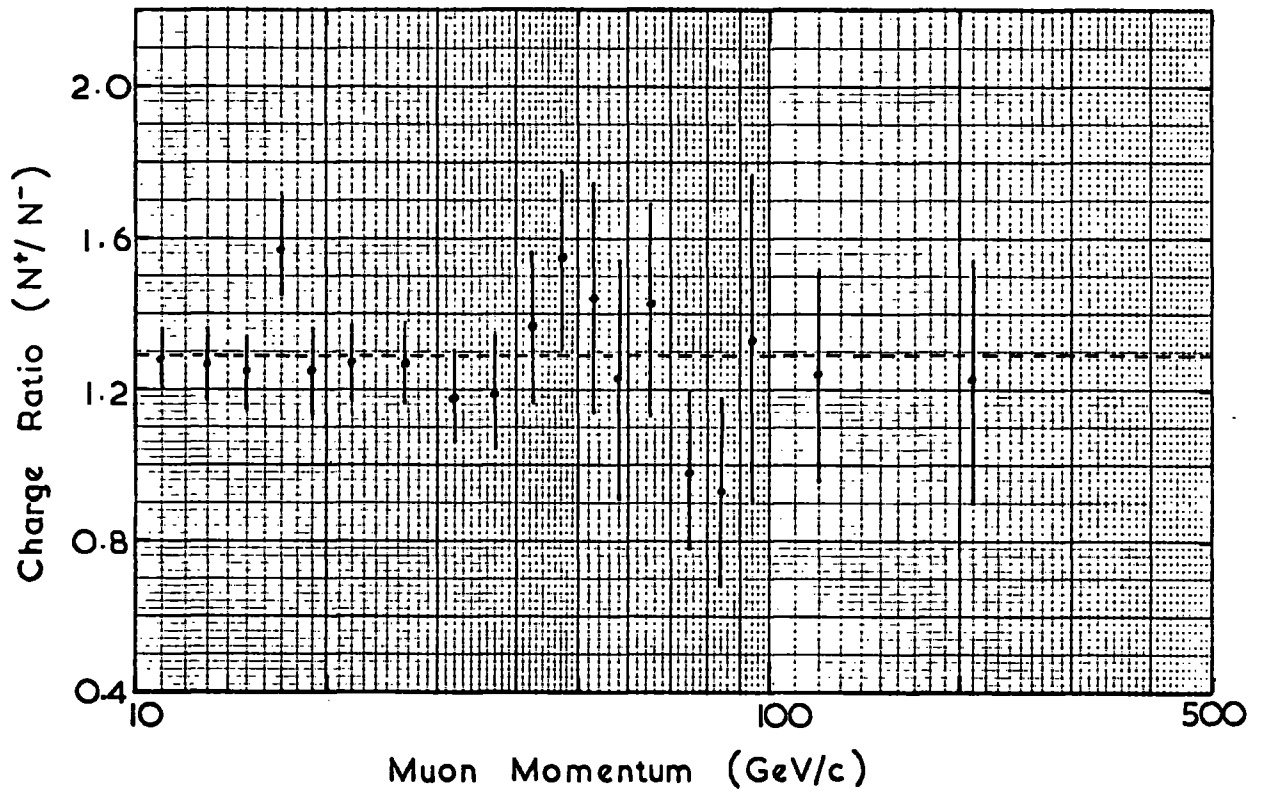
Figure 6.5 The Muon Charge Ratio.
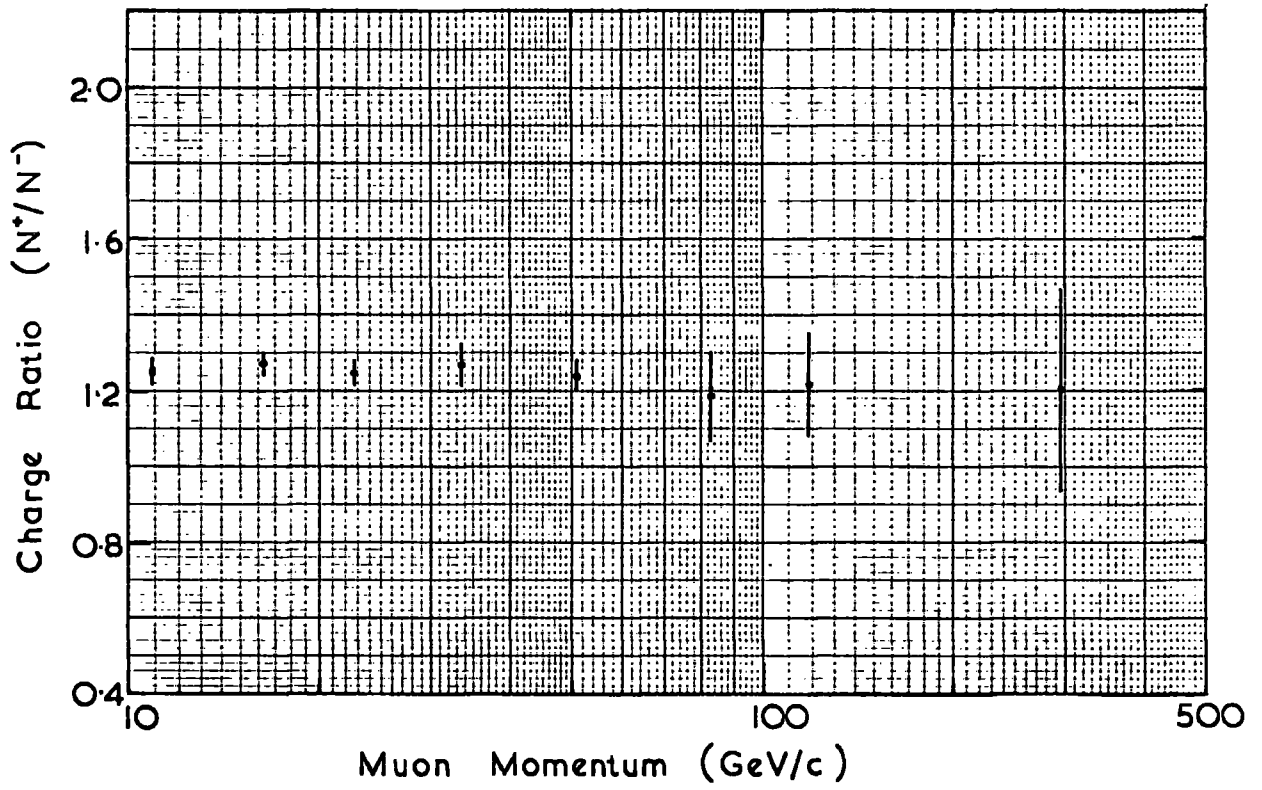
Figure 6.6 The Combined Charge Ratio of the World Data Survey.

CHAPTER 7

The Absolute Rate of Energy Loss of Muons in

Iron for the Momentum Range 5-40 GeV/c

7.1 Introduction

A reanalysis of the data presented in the previous chapter has enabled an absolute measurement to be made of the total rate of energy loss of cosmic ray muons for the momentum range 5-40 GeV/c in the iron of the magnet of the spectrograph. A study of the rate of energy loss is of importance because it serves as a check of conventional energy loss theory. This is not a trivial point because an exact treatment has never been given (see the review of Crispin and Fowler, 1970), and as far as it is known, this work is the first absolute measurement of the total rate of energy loss above values of p/mc of 100 (where p is the momentum of a particle of mass m).

7.2 The Theoretical Rate of Energy Loss

7.2.1 Ionisation

The average rate of energy loss by ionisation, $-(1/\rho_e) \, dE/dx$, was given by Bethe (1932, 1933) and Bloch (1933) and, modified for the existence of the density effect, is

$$- \frac{1}{\rho_e} \frac{dE}{dx} = \frac{A}{\beta^2} \left(B + 0.69 + 2\ln (p/mc) + \ln (T) - 2\beta^2 - \delta \right)$$

$$\text{MeV.gm}^{-1}. \text{ cm}^{-2}. \quad (7.1)$$

where $A = 0.1536 \, (Z/A_0)$ and $B = \ln (m_e c^2 (10^6 eV)/I^2)$ and where ρ_0 is the density of the medium whose mean ionisation potential is I, atomic number is Z and atomic weight is A_0; p is the momentum of the incident particle whose mass, m, is larger than that of the electron, m_e. T is the maximum transferable energy (in MeV) defined by

$$T = \frac{p^2}{m\left(\frac{m}{2m_e} + \frac{m_e}{2m} + \frac{E}{mc^2} \right)}$$

where E is the total energy of the incident particle. δ is a correction due to the density effect arising from the polarisation of the medium which reduces the effect of distant collisions.

An expression for the density correction was given by Sternheimer in 1956 but, more recently, Sternheimer and Peierls (1971) have reformulated the equations to give

$$\delta = 4.606X + C + a(X_1 - X)^m \qquad (X_0 < X < X_1) \qquad (7.2)$$

$$\delta = 4.606X + C \qquad (X > X_1) \qquad (7.3)$$

Here X_0 and X_1 are particular values of $X = \log_{10}(p/mc)$ such that $\delta = 0$ for $X < X_0$ and for $X > X_1$ the assymptotic value of equation 7.3 is reached; C, a and m are constants dependant on the properties of the medium. Substitution into the equations of Sternheimer and Peierls for the values of Z, A_0 and ρ_0 for iron of 26, 55.85 and 7.90gm. cm^{-2} respectively, gives I = 285.4eV and C = -4.285. For materials having these values of I and C, Sternheimer and Peierls give $X_0 = 0.2$, $X_1 = 3.0$, m = 3.0 and a = 0.1532 for the other constants. Hence for muons with momenta less than 100GeV/c (for which equation 7.2 applies),

$$\delta = 4.606X - 4.285 + 0.1532 (3.0 - X)^3 \qquad (p > 0.167GeV/c)$$
$$\delta = 0.0 \qquad (p < 0.167GeV/c) \qquad (7.4)$$

Hence with the values of A and B as given by Sternheimer for iron of 0.0715 and 15.65 respectively, the average rate of energy loss of muons in iron due to ionisation is given by

$$-\frac{1}{\rho_0} \frac{dE}{dx} = \frac{0.0715}{\beta^2} (16.34 + 2\ln(p/mc) + \ln T - 2\beta^2 - \delta)$$

$$MeV.gm^{-1}. cm^{-2}. \qquad (7.5)$$

This function has been calculated for the momentum range 0.1 - 100GeV/c and the results are shown in figure 7.1.
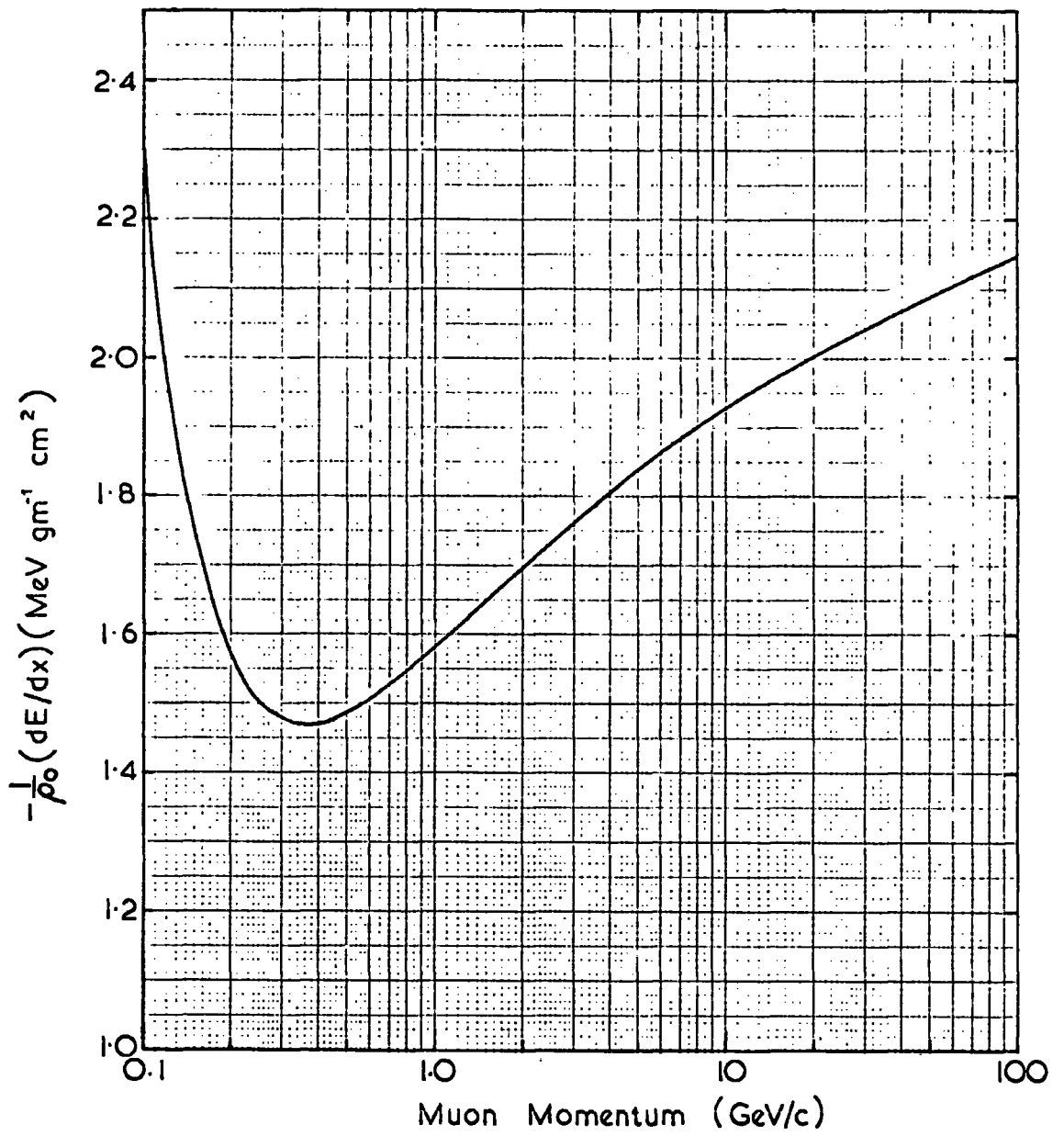
Figure 7.1   The Theoretical Rate of Energy Loss by Ionisation
for Muons in Iron.

7.2.2 Bremsstrahlung, Pair Production and Nuclear Interactions

The measured rate of energy loss of muons in MARS is not restricted to ionisation loss alone but includes that due to pair production, bremsstrahlung and nuclear interactions. Hayman et al· (1963) have calculated the contribution to the total rate of energy loss by the three processes for standard rock and these values with the appropriate correction to Z and A for iron have been used in the present calculations.

The theoretical rate of energy loss due to pair production has been given by Mando and Ronchi (1952) and that due to bremsstrahlung by Christy and Kusaka (1941). Both theories reduce to the approximate relation that

$$-\frac{dE}{dx} = \frac{CZ^2}{A} . E$$

where C is a constant and has different values for the two processes. Hence, the rate of energy loss for the two processes in iron can be calculated from the values for rock given by Hayman et al by correcting for the difference in Z^2/A. The rate of energy loss due to nuclear interactions according to the theory of George and Evans (1950) and Marshak (1952) is independent of Z and A and hence, the values given by Hayman et al· do not need correction.

Standard rock was defined as having Z = 11 and A = 22 and ρ = 2.65 gm.cm^{-3} and the iron of MARS has Z = 26, A = 55.85 and ρ = 7.90 gm.cm^{-3}. The values for the rate of energy loss due to the three processes for standard rock and iron are summarized in Table 7.1.

Table 7.1

The Contribution to the Total Rate of Energy Loss by Pair Production (p.p.), Bremsstrahlung (b.) and Nuclear Interactions (n.i.), after Hayman et al. (1963)

Muon Momentum (GeV/c)	Process	$-dE/dx$ (Mev.gm.$^{-1}$cm^2)	
		Rock	Iron
10	p.p.	0.0074	0.0163
	b.	0.0077	0.0169
	n.i.	0.0073	0.0073
100	p.p.	0.132	0.290
	b.	0.118	0.260
	n.i.	0.073	0.073

7.3 Review of Previous Experiments to Measure the Rate of Energy Loss of Charged Particles in Matter

Many experiments have been performed to measure the rate of energy loss of charged particles in matter but very few have measured this rate directly. Those experiments which have made a direct measurement have been confined, as far as it is known, to values of $\beta\gamma$ (= p/m_0) less than 100. Bulher et al. (1964) measured the range of muons in lead for momenta up to 2.48 GeV/c ($\beta\gamma$ = 23.5) and they found agreement with the theory of Sternheimer to within 2%. Backenstoss et al. (1963) studied the passage of 8 GeV/c muons through iron with particular reference to bremsstrahlung and knock-on electrons and found agreement with theory to within their experimental error of $\pm$ 7%. More recently, Bellamy et al. (1967) made absolute measurements of the most probable energy loss of muons in NaI (Tl) for the momentum range 0.5 to 10.5 GeV/c ($\beta\gamma$ = 5 to 100). Their results agree to within the 1% experimental uncertainty with the theoretical values. Other experiments include that of Bowen (1954), who made absolute measurements with accelerator produced pions and muons and cosmic ray muons up to momenta of 5 GeV/c in NaI (Tl) crystals, and that of Millar et al. (1958) who used a large liquid scintillator to study cosmic ray muons with energies of 0.3 and 2.2 GeV. These authors found essential agreement with the theoretical predictions.

The characteristic property of indirect experiments to measure the rate of energy loss is that the results have to be normalised to the theoretical values. Consequently, these experiments have only been able to confirm the basic shape of the energy loss curve and not its absolute magnitude. Crispin and Fowler (1970) give an extensive review of many indirect experiments using techniques such as drop density determination in cloud chambers and blob density determination in photographic emulsions. In all experiments agreement is found between the theory of Sternheimer and the normalised experimental results. Another widely used, indirect technique has been to compare the cosmic ray muon momentum spectrum or intensity at sea level with that underground. (See Ashton,

1961, and Pine et al., 1959). However, these experiments suffer from
uncertainties in the precise shape of the sea level momentum spectrum and the
density of the overlying strata through which the muons pass. These indirect
measurements have confirmed the shape of the energy loss - βy relation up to
values of βy greater than 1000.

It is concluded from this review that as far as it is known, the rate of
energy loss of charged particles in matter has not been measured directly
beyond values of βy of 100 and only the shape of the energy loss - βy relation
has been confirmed beyond this value. Consequently, the work presented in
this chapter constitutes a new measurement of the absolute rate of energy loss
over the range of βy from 100 to 400.

7.4 The Theory of the Experimental Method

7.4.1 The Equation of Motion of a Charged Particle Suffering Energy Loss in a Magnetic Field

As muons pass through the magnet blocks and other absorber of MARS, they
continually lose energy and consequently the radius of curvature of their
trajectories continually decreases. The rate of change of this curvature is
related to the rate of energy loss. For a charged, relativistic particle with
energy E and momentum p ($\sim E/c$) the radius of curvature, r, of its trajectory
in a magnetic field is given by

$$r = mpc = mE$$

where m is a constant defined by the properties of the particle and the magentic
field. The average rate of energy loss, k, is defined by $k = -dE/dS$ where dS
is the incremental path length of the particle in the absorber. In an (S, ψ)
co-ordinate system, the radius of curvature is given by $r = dS/d\psi$ and hence
$dS = -dE/k = mEd\psi$ or

$$d\psi = \frac{-1}{mk} \cdot \frac{dE}{E} . \tag{7.6}$$

$d\psi$ represents the change in the angle of the trajectory relative to a fixed line.
Integrating equation 7.6 over the energy range E_o to E and the angular range ψ_o

to ψ we obtain

$$\psi = \psi_0 + \frac{1}{mk} \ln \left(\frac{E_0}{E_0 - kS} \right)$$

where kS is the total energy loss. If $kS \ll E_0$ then

$$\psi = \psi_0 + \frac{S}{mE_0} + \frac{kS^2}{2mE_0^2} \qquad (7.7)$$

Before this equation can be applied to MARS it is necessary to convert from the (S,ψ) co-ordinate system to a cartesian one. To a first approximation, the arc length, S, of a circle which passes through the origin and whose centre lies on the y axis of a cartesian system, is given as a function of x and the radius, r, by $S = x (1 + x^2/2r^2)$. In general, if the centre of the circle does not lie on the y axis then it can be made to do so by rotating the co-ordinate system through ψ_0, and hence

$$S = x \sec \psi_0 . (1 + (x \sec \psi_0)^2/2r^2) \qquad (7.8)$$

In a cartesian co-ordinate system $dy = \sin \psi \, dS$, and hence, with the condition that $S/mE_0 + kS^2/2mE_0^2$ is small,

$$dy = (\sin \psi_0 + \cos \psi_0 (S/mE_0 + kS^2/2mE_0^2)) \, dS \qquad (7.9)$$

Integrating equation 7.9 over y, between y_0 and y, and over S between S_0 and S we obtain

$$y = A + x \tan \psi_0 + x^2 \frac{\sec \psi_0}{2mE_0} + x^3 \left(\frac{k}{6mE_0^2} + \frac{\tan \psi_0}{2m^2E_0^2} \right) \sec^2 \psi_0 + \cdots \qquad (7.10)$$

where A is a constant.

It is concluded that the equation of the trajectory of a charged particle undergoing energy loss in a magnetic field can be approximated to the equation of a cubic and that the average rate of energy loss can be extracted from the coefficient of the x^3 term of a cubic fitted to the co-ordinates of the trajectory of such a particle.

7.4.2. A 'Least-Squares' Cubic Fit

The general cartesian equation of a cubic is $y = a_o + a_1 x + a_2 x^2 + a_3 x^3$.

In a similar manner to the derivation of the least-squares parabola fit given

in chapter 3, it can be shown that the coefficients of a 'least-squares' cubic

fit to n points (x_i, y_i), where $n > 4$, can be found by solving the linear

equations

$$\begin{pmatrix} \Sigma x^6 & \Sigma x^5 & \Sigma x^4 & \Sigma x^3 \\ \Sigma x^5 & \Sigma x^4 & \Sigma x^3 & \Sigma x^2 \\ \Sigma x^4 & \Sigma x^3 & \Sigma x^2 & \Sigma x \\ \Sigma x^3 & \Sigma x^2 & \Sigma x & n \end{pmatrix} \cdot \begin{pmatrix} a_3 \\ a_2 \\ a_1 \\ a_0 \end{pmatrix} = \begin{pmatrix} \Sigma yx^3 \\ \Sigma yx^2 \\ \Sigma yx \\ \Sigma y \end{pmatrix} \qquad (7.11)$$

where $\Sigma x^m \equiv \sum\limits_{i=1}^{n} x_i^m$.

7.5 The Accuracy of the Energy Loss Determination

In theory, the rate of energy loss can be uniquely defined for each particle

but because of Coulomb scattering in the iron and uncertainties in track location

it is necessary to find the mean loss for groups of particles rather than

individuals.

The dependence of the calculated energy loss upon the accuracy of track

location can be found by the same method as that used to calculate the m.d.m.

in chapter 5. From equation 7.10 with $\psi_o = 0$, $a_3 = k/6mE_o^2$ or $k = 6mE_o^2 a_3$. Hence

$$\frac{dk}{dy} = 6mE_o^2 \cdot \frac{da_3}{dy} . \qquad (7.12)$$

da_3/dy can be determined by differentiating the determinates used to calculate

a_3 from equations 7.11. With the approximation that $\Sigma x = \Sigma x^3 = \Sigma x^5 = 0$,

$$\frac{da_3}{dy} = \frac{(f_1^2 \Sigma x^2 + f_2^2 \Sigma x^6 + 2f_1 f_2 \Sigma x^4)^{\frac{1}{2}}}{f_1 \Sigma x^4 + f_2 \Sigma x^6}$$

where $f_1 = \Sigma x^4 (\Sigma x^2)^2 - N (\Sigma x^4)^2$ and $f_2 = N \Sigma x^2 \Sigma x^4 - (\Sigma x^2)^3$, and, for the

tray co-ordinates of the film data, $da_3/dy = 0.0555 \text{ m}^{-3}$. Hence from equation

7.12 and with m = 2.046 m. GeV^{-1}

$$\Delta k = 0.68 \, E_o^{\,2}. \, \Delta y \quad \text{GeV/m.}$$

The average track location uncertainty for the film data was 0.82mm and hence the uncertainty in the rate of energy loss at 10 GeV/c in the absence of scattering is $\pm$ 0.056 GeV/m and at 100 GeV is $\pm$ 5.6 GeV/m compared to a theoretical mean value of about 1.6 GeV/m. These uncertainties will be further increased by scattering, especially at the low energies.

7.6 Experimental Details

The data with which the average rate of energy loss was calculated were the same as those presented in the previous chapter. A minimum of four points are required by the 'least-squares' fit before the cubic is uniquely defined, but a fit to four points is absolute and would include any discontinuities in the trajectory due to Coulomb scattering or large energy transfers. To ensure that the average rate of energy loss was calculated for each muon, only those muons whose trajectories were unambiguously defined at all five measuring levels were selected. In practice, this meant that those muons, for whom large energy transfers near the bottom of a magnet block resulted in them being accompanied by an electron shower through a measuring level, were rejected. A correction has been made to the theory for this rejection and is described below.

The total thickness of absorber in the spectrograph was measured and the contributions from the various spectrograph elements are given in Table 7.2. The total absorber thickness was found to be (3970 $\pm$ 20) gm. cm^{-2}, of which the magnet blocks contribute 97.5%.

7.7 The Experimental Results

The data were collected into momentum cells whose widths and mean momenta are given in table 7.3. Data were also available for muon energies above 45 GeV/c but because of the paucity of data in this energy region and the rapid increase in the uncertainty in the rate of energy loss with energy, these data

were ignored. The distributions of the value of k for each momentum cell are given in figure 7.2. The mean values of these histograms do not represent the true rate of energy loss (in GeV/m) because they need correction for the effect of the gaps between the magnet blocks. These correction factors are calculated in the next section.

Table 7.2

The Absorber Thickness of the Elements of MARS

Element	Material	Thickness (cm)	Density (gm.cm^{-3})	Thickness (gm. cm^{-2})
Magnet	Iron	491.3	7.90	3876.1 $\pm$ 20.0
Scintillators	Ne102a	15.0	1.032	15.5 $\pm$ 0.3
Measuring Trays	(Aluminium	5.5	2.7	14.9 $\pm$ 0.6
	(Glass	8.4	2.7	22.7 $\pm$ 0.9
Momentum Trays	(Aluminium	2.3	2.7	6.2 $\pm$ 0.3
	(Glass	3.9	2.7	10.4 $\pm$ 0.5
Miscellaneous	-	-	-	24.5 $\pm$ 1.0
TOTAL				3970.0 $\pm$ 20.1

In an attempt to minimise the effect of noise in the data, the distributions of the standard deviations of the cubic fits for each momentum cell were studied. It was finally decided to reject the 10% of events which had the largest standard deviations. This selection criterion was adopted in preference to that of chopping the standard deviation distributions at three times their mean value, as was described for the momentum cells in chapter 6, because of the

Table 7.3

Incident Momentum Range (GeV/c)	Mean Incident Momentum (GeV/c)	Mean Momentum at Centre of Spectrograph (GeV/c)	Mean Rate of Energy Loss (GeV/m, uncorrected)	Correction Factor	Mean Absolute Rate of Energy Loss (Mev.gm.$^{-1}$cm^2)
7.8-12.0	10.2	6.3	1.468 ± 0.051	1.278	1.876 ± 0.065
12.0-14.1	12.5	8.6	1.562 ± 0.059	1.274	1.990 ± 0.075
14.1-24.5	18.5	14.4	1.571 ± 0.049	1.271	1.997 ± 0.062
24.5-45.0	32.0	27.7	1.70 ± 0.10	1.291	2.191 ± 0.130

Mean incident momentum,
P = 10.2 GeV/c

Mean value, M = 1.468 ± 0.051 GeV/m

Number of muons,
N = 653

P = 12.5 GeV/c

M = 1.562 ± 0.059 GeV/m

N = 624

P = 18.5 GeV/c

M = 1.571 ± 0.049 GeV/m

N = 1623

P = 32.5 GeV/c

M = 1.70 ± 0.10 GeV/m

N = 933

Average rate of energy loss, dE/dx (GeV/m, uncorrected for gaps between magnet blocks.)
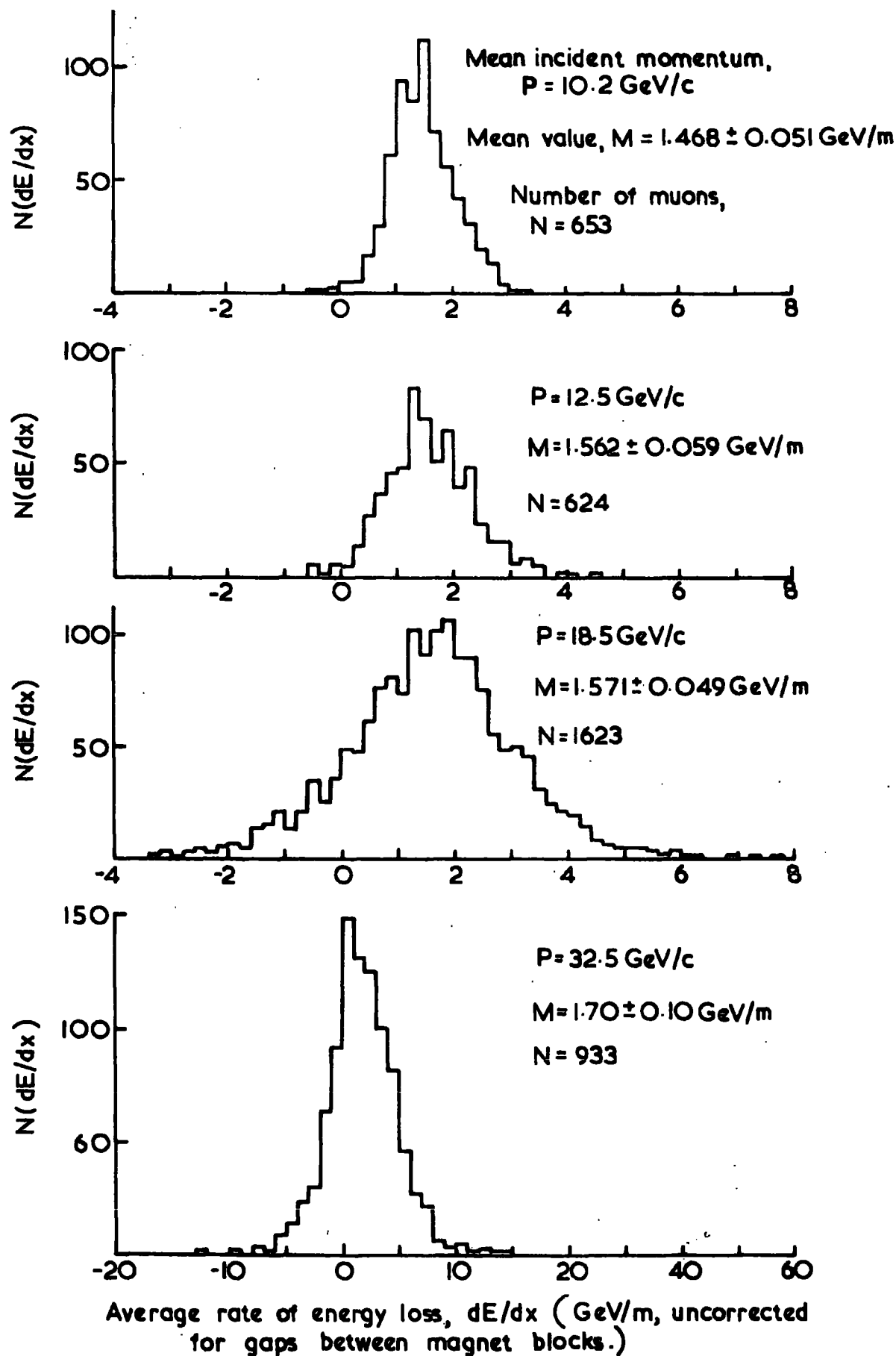
Figure 7.2   The Rate of Energy Loss Distributions for the Momentum Cells (Uncorrected).

uncertainties in the quality of the cubic fit at the lowest energies and its influence on the shape of the standard deviation distributions. However, as can be seen from table 7.4, where a comparison is made between the mean values of the original histograms and those with 10% of the events removed, the rejection of these events had negligible effect on the mean values of the histograms.

The mean values of the histograms and their associated uncertainties are given in table 7.3. The mean value of the momentum of the muons at the centre of the spectrograph have also been calculated for each cell and they too are given in the table.

Table 7.4

A Comparison between the Mean Rates of Energy Loss
for the Data with and without the 10% Event Rejection

Momentum Cell (GeV/c)	Mean Rate of Energy Loss (GeV/m, uncorrected)	
	All data	10% rejection
7.8 - 12.0	1.47 ± 0.05	1.47 ± 0.05
12.0 - 14.1	1.58 ± 0.06	1.56 ± 0.06
14.1 - 24.5	1.58 ± 0.05	1.57 ± 0.05
24.5 - 45.0	1.71 ± 0.12	1.70 ± 0.10

7.8 The Corrections to the Data

The coefficient of the x^3 term of the cubic gives the average rate of energy loss through the spectrograph, in GeV/m, assuming that the spectrograph is a continuum of magnetised absorber. Consequently, the experimental results have to be corrected for the effect of the gaps between the magnet blocks. The correction factors were calculated by simulating muon tracks through the spectrograph with fixed rates of energy loss and for various momenta.

The ratio of the true to the observed rate of energy loss was calculated and this ratio is plotted as a function of the true rate of energy loss for incident muon momenta of 10.2, 12.5, 18.5 and 32.0 GeV/c at their mean incident zenith angles of 10°, 7.5°, 4.4° and 2.5° respectively, in figure 7.3. From these curves it is possible to extract iteratively the true average rate of energy loss for the momentum cells by successive approximation of their correction factors. The final correction factors used and the average absolute rate of energy loss for the momentum cells are given in table 7.3.

7.9 Corrections to the Theory for the Rejection of Bursts

It was demanded of the data that the track of the muon be unambiguously resolvable at each measuring level. It was considered that this meant in practice that if the muon was accompanied by three or more electrons into any measuring level, the event was rejected. Consequently, the theoretical rate of energy loss has to be corrected for the exclusion of these events.

Messel and Crawford (1970) have computed tables of electron-photon shower distribution functions for lead, copper and air absorbers for a variety of primary and secondary electron energies. Their results for copper and for secondary electron energies above 10 MeV have been utilised in what follows because it is considered that these conditions most closely resemble those of MARS. Figure 7.4 shows the mean electron density as a function of the thickness of absorber in radiation lengths, for primary electron energies of 200, 500 and 1000 MeV. It is apparent that only primary electrons with energies in excess of ~ 800 MeV produce electron showers containing three or more electrons. The theorectical rate of energy loss has to be corrected for those energy transfers in excess of 800 MeV which are sufficiently near to the bottom of a magnet block as to produce an electron shower containing three or more electrons at a measuring level.
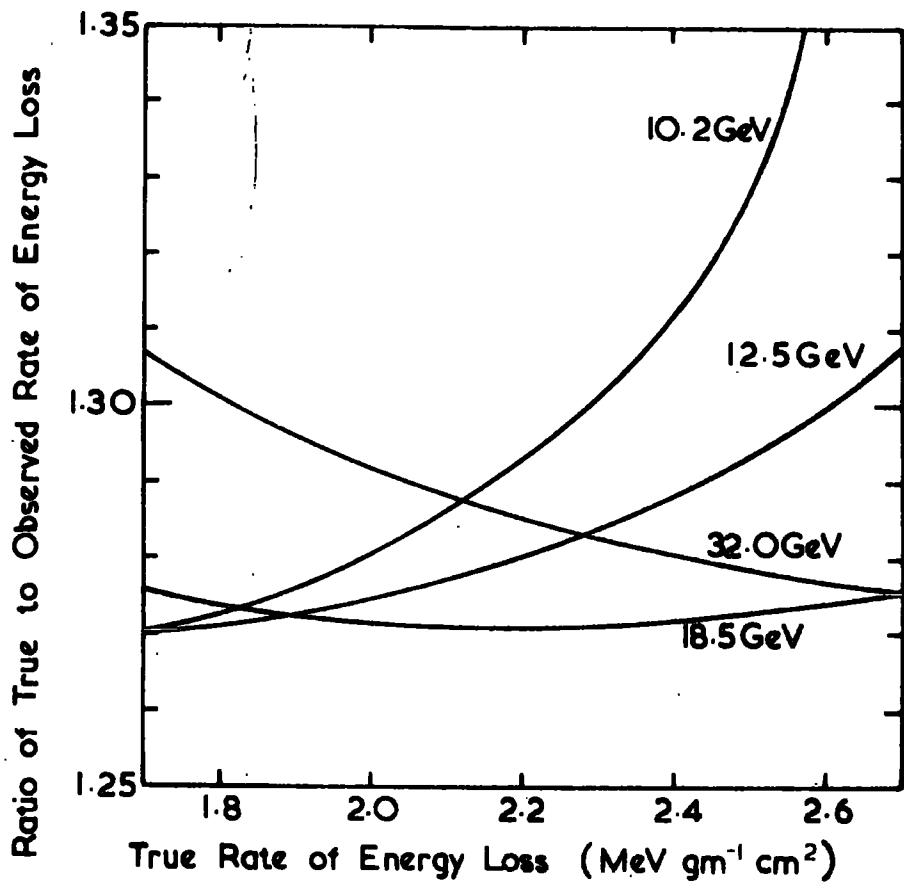
Figure 7.3   The Rate of Energy Loss Correction Curves.
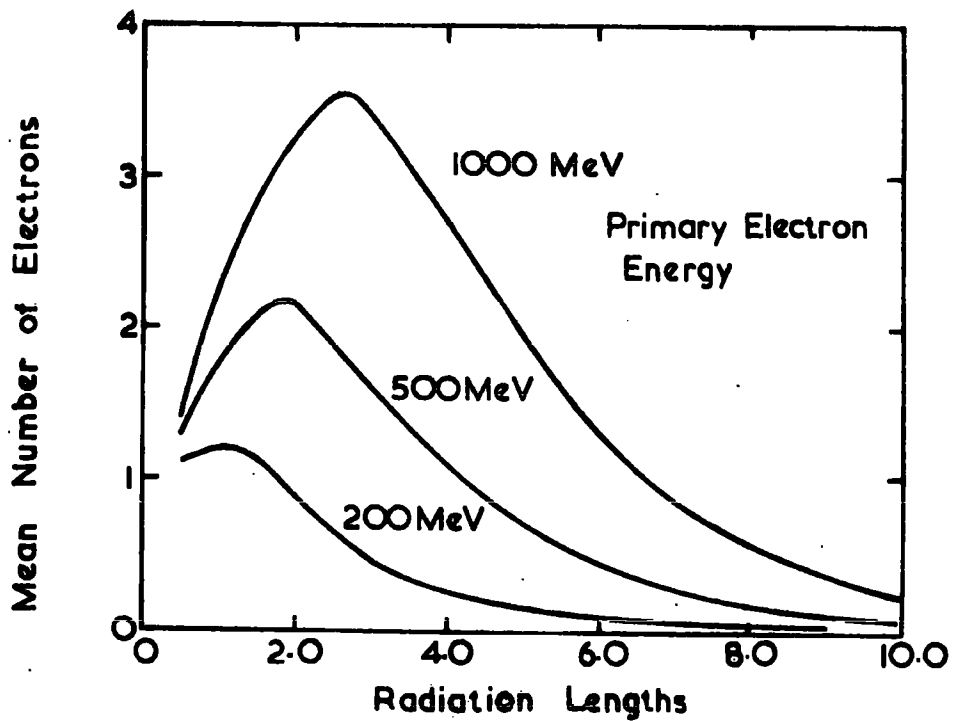
Figure 7.4   The Electron Photon Shower Distribution Functions.

Rogers (1965) has calculated the probability of energy transfers in iron for the knock-on, pair production and bremsstrahlung processes and his results for muon energies of 10 GeV and 100 GeV in iron are shown in figures 7.5 (a) and (b). It can be seen that at 10 GeV the knock-on process predominates but at 100 GeV the pair production and knock-on processes contribute almost equally to the energy loss in the region of interest (i.e. energy transfers in excess of 800 MeV). Equation 5.1 gives the probability of an energy transfer of E' for the knock-on process and hence, the contribution to the total rate of energy loss by energy transfers above 800 MeV in iron is given by

$$\int_{800}^{T_{max}} 0.0714 \; \frac{1}{(E')^2} \; E'. \, dE' \quad MeV. \; gm.^{-1} \; cm^2 \qquad (7.13)$$

where T_{max} is the maximum transferable energy. At 10 GeV, $T_{max} = 4.8$ GeV and equation 7.13 gives 0.128 MeV. gm.$^{-1}$ cm^2 as the contribution above 800 MeV. At 100 GeV, the maximum transferable energy is 90 GeV and, if it is assumed that equation 7.13 also applies to pair production, then the total rate of energy lost by energy transfers above 800 MeV is 0.674 MeV. gm.$^{-1}$ cm^2.

Grupen et al. (1972) in a further experiment using MARS have studied the spectrum of burst sizes emanating from the magnet blocks. Their results are shown in figure 7.6 where the probability of observing a burst of a certain size is given as a function of the muon energy. The broken line on the diagram is the extrapolation of their results to give the probability of observing a burst with > 3 electrons. The probabilities at 10 GeV and 100 GeV are 0.012 and 0.037 respectively. Hence the probabilities of observing bursts in one or more of the measuring levels below magnet blocks are, from the binomial probability theorem, 0.047 and 0.14 at 10 and 100 GeV respectively. Hence the total unaccounted rate of energy loss at 10 and 100 GeV are 0.0065 and 0.094 MeV gm.$^{-1}$ cm^2 respectively and it is by these quantities that the theoretical values have been reduced.
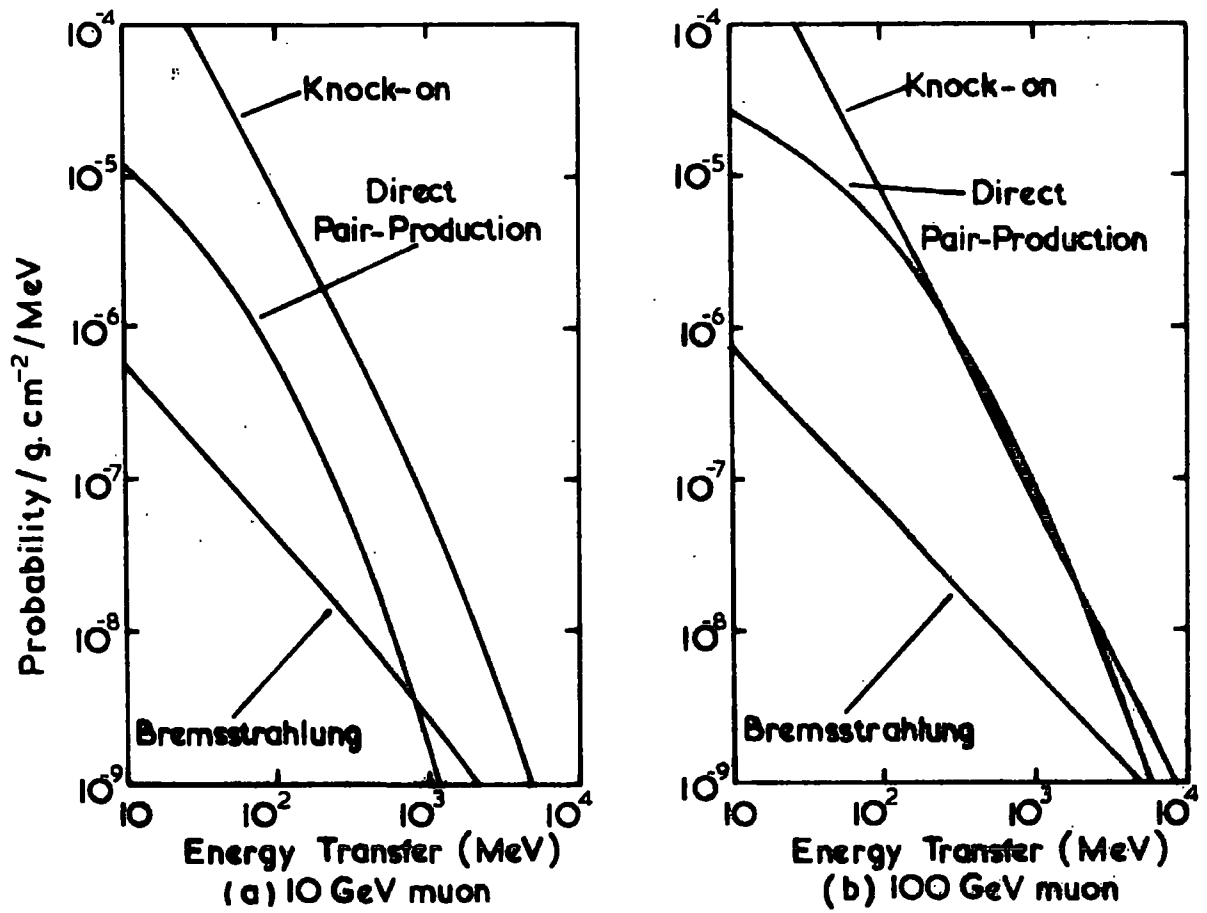
Figure 7.5. Differential Energy Transfer Curves for Muons in Iron.
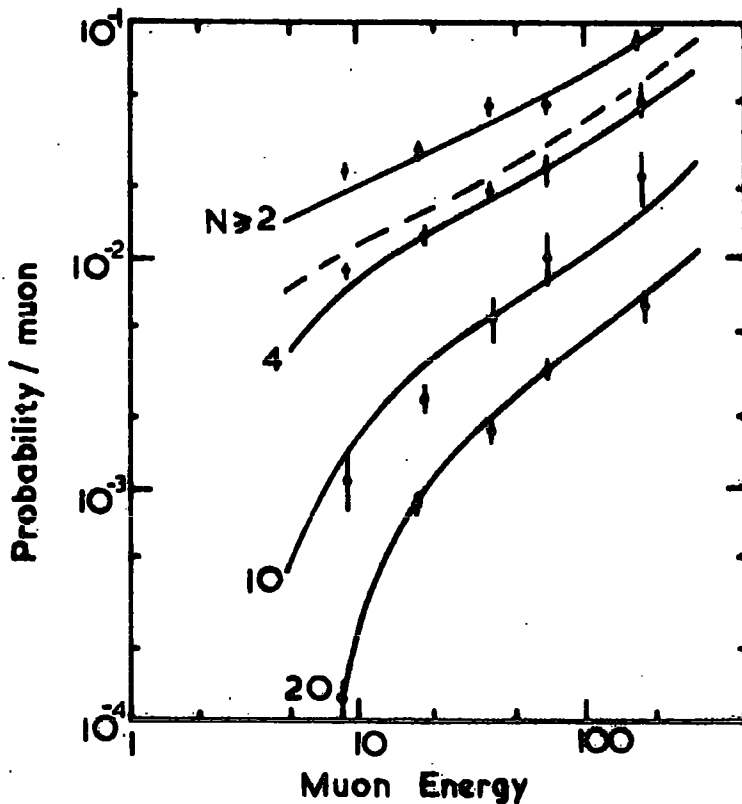
Figure 7.6 The Burst Size Probability for Muons in Iron.

7.10 Comparison between the Experimental Results and the Theoretical Values

The experimental results and theoretical values are shown in figure 7.7. The experimental points plotted refer to the mean muon momentum at the centre of the spectrograph. The theoretical curves for ionisation loss alone and for the total loss due to all processes are also given. As is evident from the figure, there is very good agreement between the theoretical predictions of Sternheimer and Peierls (1971) (together with values for the rate of energy loss due to pair production, bremsstrahlung and nuclear interactions as given by Hayman and Wolfendale, 1963) for the absolute magnitude of the total mean rate of energy loss of muons in iron.

7.11 Discussion and Conclusions

The agreement between experiment and theory to within the experimental errors (which only range from 3.5% at 6 GeV/c to 6% at 30 GeV/c) not only indicates that the theory of Sternheimer and Peierls for the absolute rate of energy loss of muons in iron is correct, but it also reflects the accuracy of the technique by which this absolute magnitude was measured.

It is worth-while considering the limitations of this technique with respect to the momentum range over which reliable results may be obtained. In deriving equation 7.7, it has been necessary to assume that the total energy lost was small compared to the initial energy of the muon. Also, in equation 7.9 a small angle approximation has been made. Hence equation 7.10 cannot be expected to be valid at muon energies of only a few GeV. However, the analysis of the simulated events, the results of which are summarised in figure 7.3, show that there is no marked divergence of the correction factors over the incident muon energy range 10-32 GeV and that the technique yields reliable results even at the lowest energies. The possible extension of the technique to energy loss measurements at higher muon energies is limited because of the statistics required to counteract the increased uncertainty in the measured energy loss
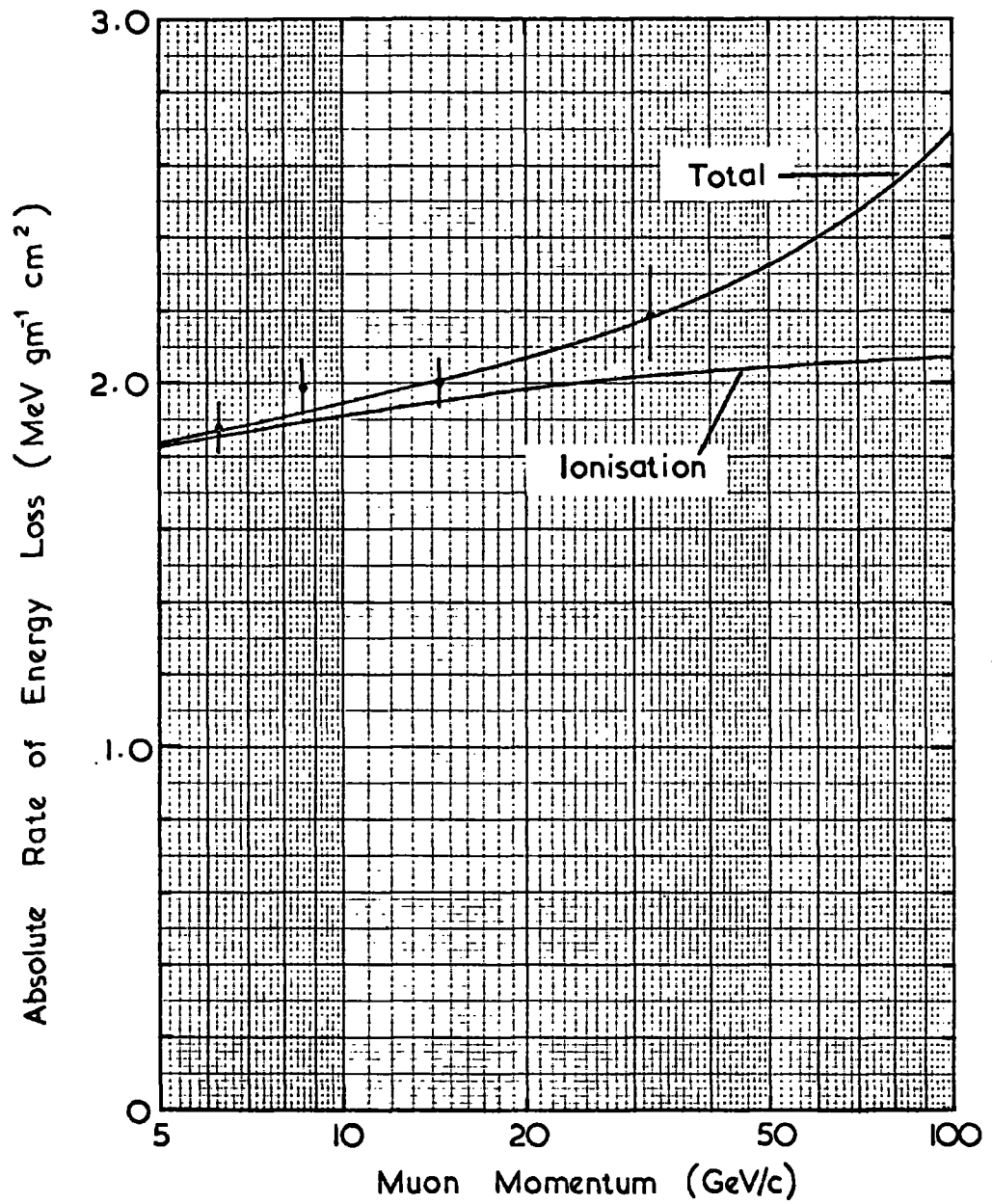
Figure 7.7   The Theoretical and Experimental Absolute Rates of Energy Loss for Muons in Iron.

(see equation 7.12). For example, even with a track location accuracy of 0.3mm, 10^4 muons are required to determine the absolute rate of energy loss for 100 GeV muons to within 1%.

In conclusion, it is reiterated that the results presented in this chapter represent an absolute determination of the total mean rate of energy loss of muons in iron in an energy region beyond all previous direct measurements and that excellent agreement is found between the theory of Sternheimer and Peierls (together with values for the rate of energy loss for other processes) and the experimental results.

APPENDIX A

The Core Store and Its Circuitry

A.1 Introduction

The operation of the core store in conjunction with the remainder of the MARS equipment has already been described in Chapter 3. This appendix contains a detailed description of the core store and the electronic circuitry which provides the control pulses, data and addresses for it.

The core store is a Mullard Core Memory System type MM1501. The control electronics were constructed from Mullard DTL integrated logic circuits, the basic logic function being the NAND function. A schematic diagram of the core store circuitry is shown in figure A.1. The numbers in parentheses refer to the number of interconnections between the units. It can be seen that the circuitry is divided up into eight distinct units. Three units are responsible for providing the core store with data, two are responsible for the core store addresses and one forms the data output lines to the computer. The remaining two units are the core store itself and a unit which is responsible for the timing and control of all the other units - the TCU (Timing and Control Unit).

Before each individual unit is described, it is instructive to outline the method of operation of the core store circuitry.

A.2 The Mode of Operation

The core store circuitry is initiallised each time the momentum selector (Section 2.7.2) detects a 'high momentum' event. The address scaler and all the other registers of the circuitry are immediately reset by the TCU ready for the loading of the data which is to be sent to the computer. There are two distinct classes of loading cycle: that of the event header and that of the measuring tray data, and after each individual cycle the address scaler of the core store circuitry is incremented by one.

The header information is loaded first and for this 18 load cycles are required. When this is complete, a pulse is sent to the control circuitry of
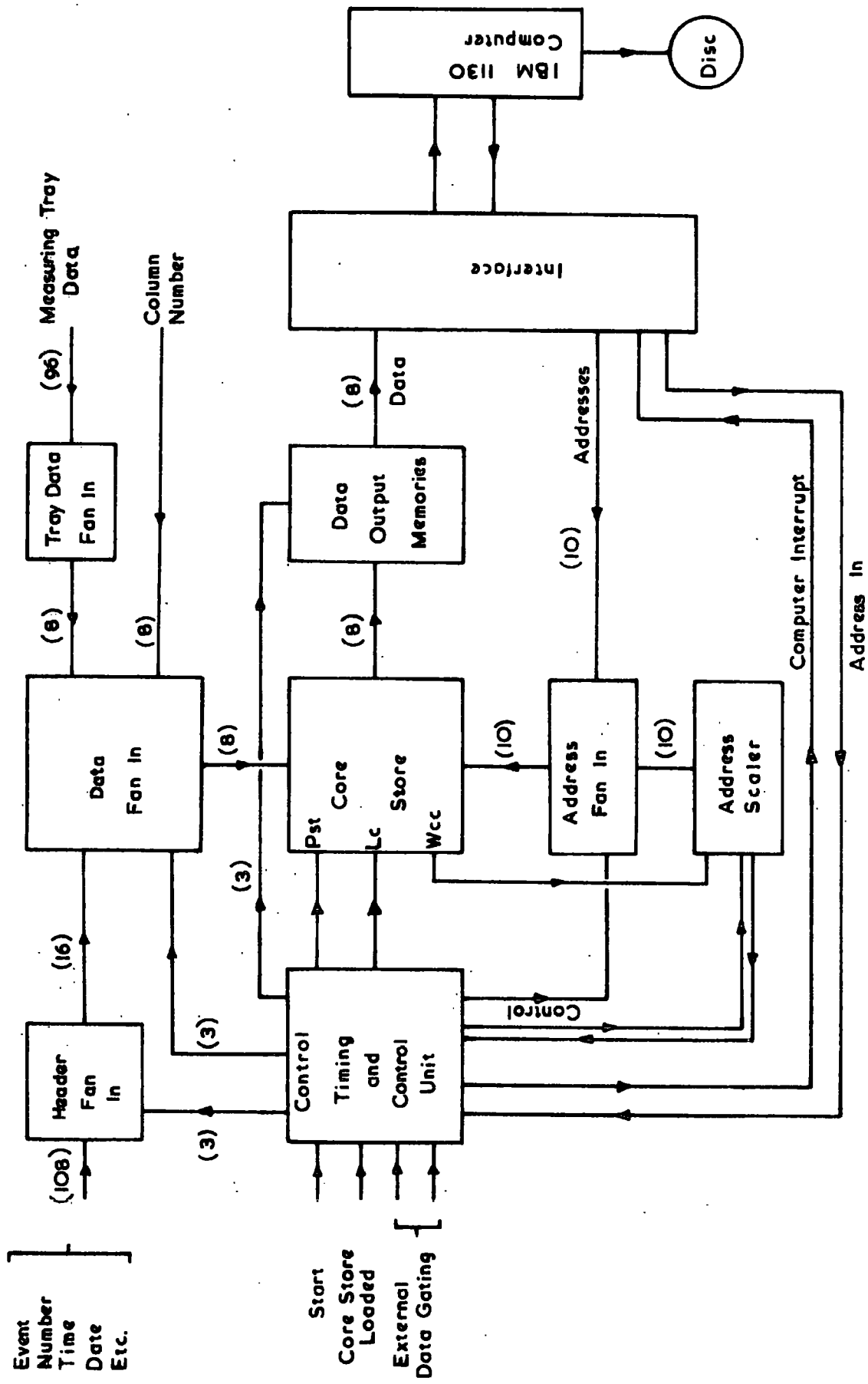
Figure A.1   Schematic Representation of the Core Store Circuitry

the measuring trays, which is external to the core store circuitry. The measuring trays are scanned and when a tube column is found which contains data a pulse is returned to the TCU. Two load cycles then follow, one to load the column number and the other to load the data from that column, both of which are residing on the input lines to the circuitry. A pulse is then again returned to the measuring tray circuitry. This process continues until all the trays have been scanned and a 'core store loaded' pulse is returned to the TCU. This pulse is used to interrupt the computer and to prepare the circuitry for the unloading of the core store into the computer.

The computer sends addresses to the core store in conjunction with a pulse known as the 'address in', which cyles the core store in the read-write mode. The addresses and the 'address in' are present for 25 μs, after which time the computer assumes that the data from the core store resides on the computer input lines from the interface. Addresses are generated in logical order and after each cycle the address scaler of the core store is decremented by one. When this scaler reaches zero the core store is empty and an extra data line known as the 9th bit is set. This signifies to the computer that the data transfer is complete.

A.3 The Core Store

The core store contains 1024 8-bit words which can be accessed in a random manner. As was described in section 2.7.5, it can operate in the clear-write or read-write modes. The former mode empties a word and then writes data into it and the latter places the contents of a word on the output lines and then writes new data back into the word. The cycle time for either operation is 4 μs and the timing diagram for the control pulses is shown in figure A.2. The logic levels of the various commands and of the data and address lines are of no importance where they are shown shaded on the diagram.

Each word in the core store is accessed by placing a 10-bit binary address and its compliment on the core store address lines and then applying the start command (Pst). The operation mode is determined by the state of the Clear
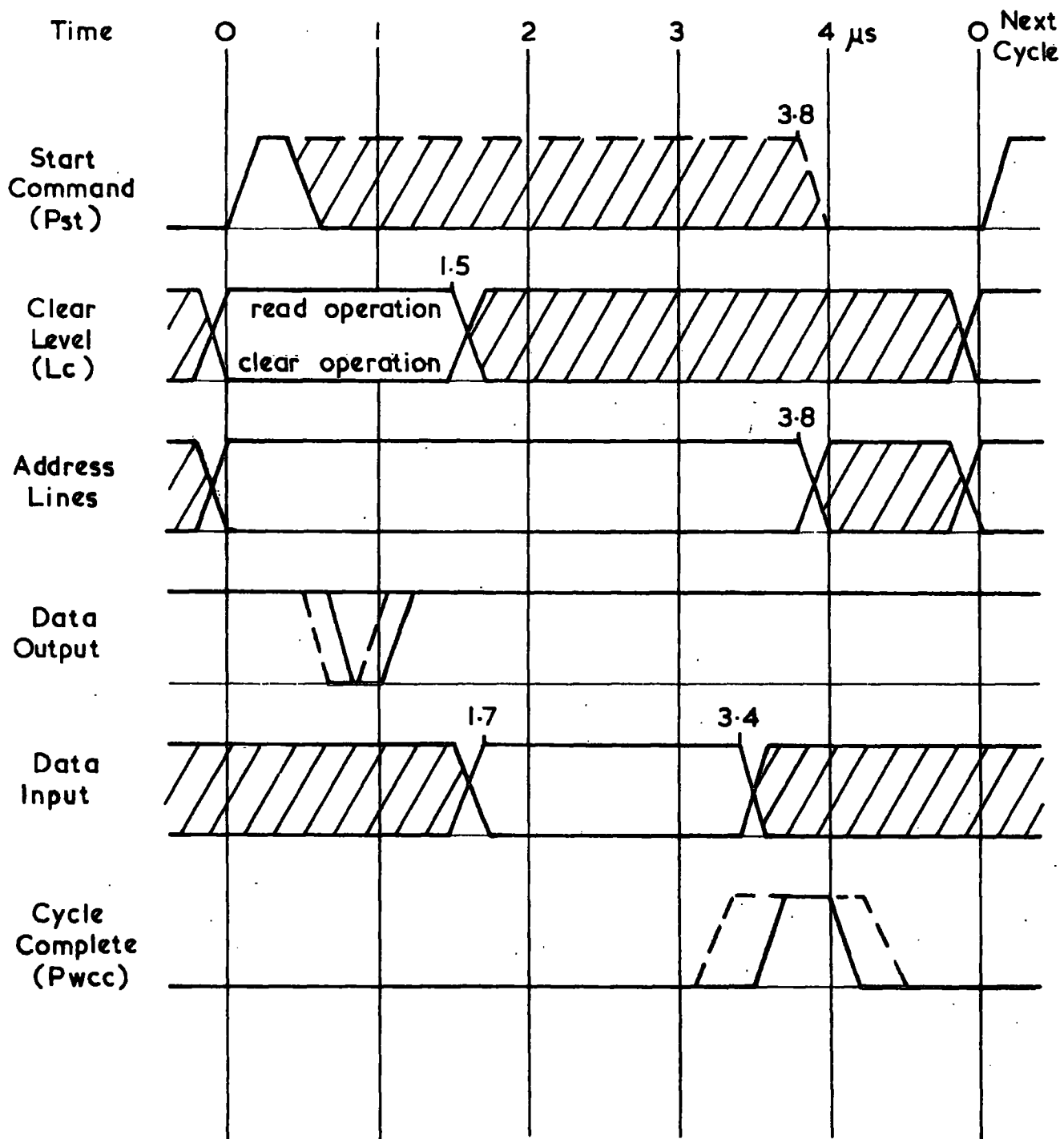
Figure A.2   Core Store Timing Diagram.

level, Lc. If a clear-write operation is required this level must be a logical 0 during the first 1.5 μs of a cycle,whereas a read-write operation is produced if it is a logical 1 during this time. The data contained in a word becomes available on the output lines after 0.5 μs of a read-write cycle. The data output lines are always at a logical 1 and only switch to a logical 0 for about 0.2 μs when the corresponding bit of the word being accessed contained zero. After 2 μs the data residing on the input lines are written into the word. At the end of each cycle a 'cycle complete' (Pwcc) pulse is returned from the core store.

A.4 The Header Information Circuitry

The data for the header information are provided by external circuits and they are supplied as d.c. logic levels. At the appropriate moment they are sampled by the core store circuitry shown in figure A.3. The header information is described in Appendix B; the contents of one 16-bit computer word being the combination of two 8-bit core store words. There are 18 8-bit header words and the circuit shown in figure A.3 is repeated (except for the first element) in the core store circuitry.

The circuit consists of a 9-bit shift register and an 8 x 8 matrix of dual input NAND gates. Each column of gates of the matrix are gated by the output of one of the latter eight elements of the shift register and the outputs of each row of gates are OR-ed together to form one of the 8 data output lines from the circuit. The header information is fed into the other inputs of the dual NAND gates and the data lying on the inputs of a particular column of gates appears on the outputs of the circuitry when the corresponding element of the shift register is set to a logical 1.

The circuit is controlled by the TCU described later. The shift register is initially reset such that the Q outputs of each element except the first are set to a logical 0. On the application of shift pulses, the logical 1
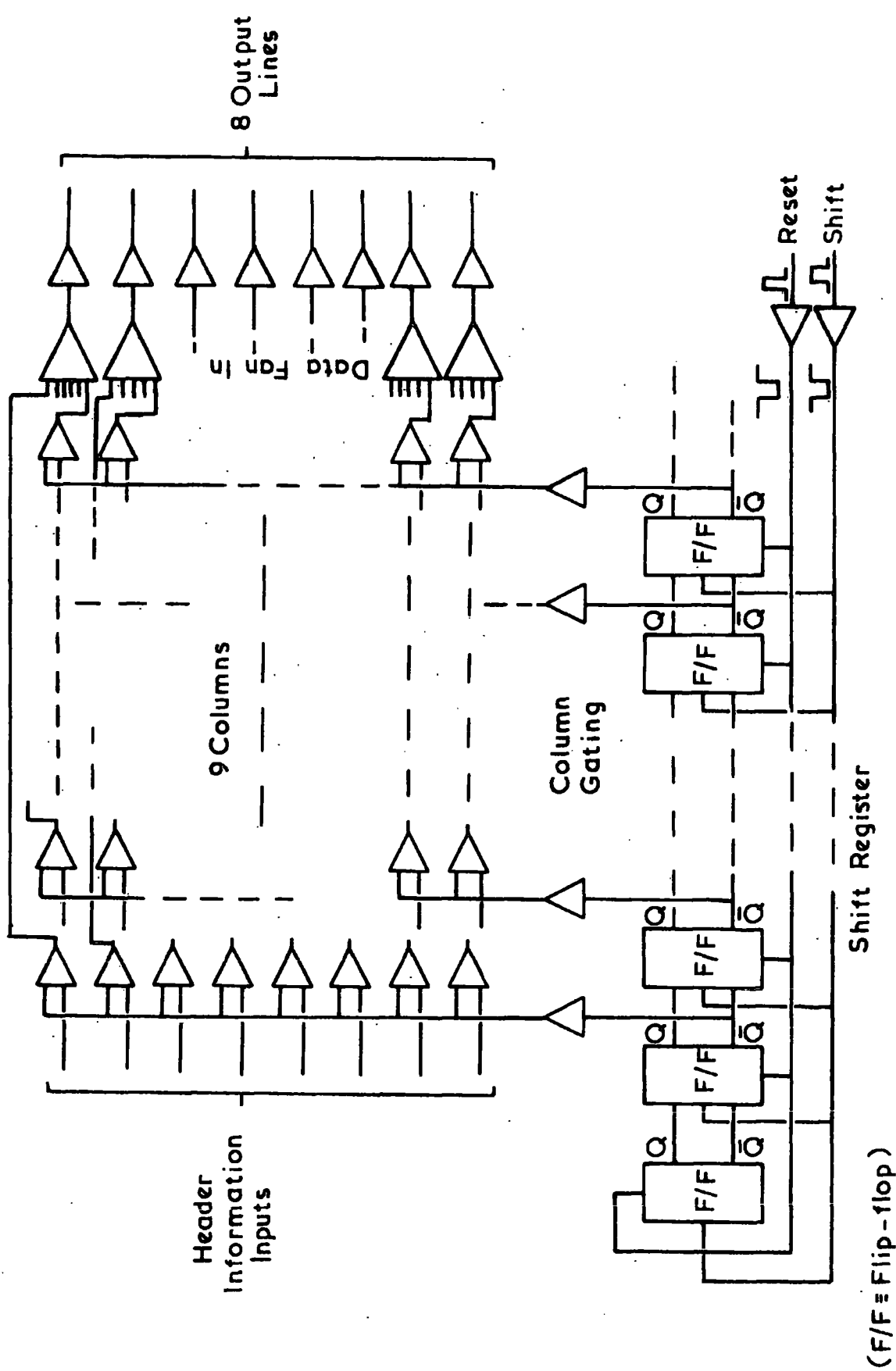
Figure A.3   The Header Information Fan In

(F/F = Flip-flop)

contained in the first element moves through the shift register and each column of gates is opened up in turn. Consequently, the header information contained in each column appears on the output lines in turn. The shift register of the second circuit is joined directly on to that of the first and hence a total of 18 shift pulses are required before the last column is opened up. The setting of this last element is used by the TCU to route the loading sequence to the measuring trays.

The data from these circuits pass into the final data fan-in circuit described in section A.6.

A.5 The Measuring Tray Data Fan-In

The eight data lines from each of the 12 trays (2 x 5 measuring trays + 2 azimuthal trays) are combined together to form one set of eight lines. A section of the circuit which accomplishes this data fan-in is shown in figure A.4. The data lines which correspond to the same tube layer in each of the twelve trays are OR-ed together. Normally all of the data lines are at a logical 0 but when one of the tube columns in one of the trays is opened up by external circuits, the discharged tube pattern in that column appears at the output of this circuitry. These data are then passed to the circuitry described in the next section.

A.6 The Data Fan-In to the Core Store

This section of the core store circuitry routes the tray data, the column numbers and the header information onto eight data lines for input to the core store and its circuit diagram is given in figure A.5. The header and tray data are supplied by the circuits described in sections A.4 and A.5 respectively but the column number is supplied externally.

The data are selected by the gating pulses J, K and M, which come from the TCU, and the data are placed in the output flip-flops for the core store to read. During the loading of the header information, gate pulses are only applied to M, but when the tray data are being loaded, the column numbers and tube configurations are entered by gate pulses applied to M and to K and J alternately.
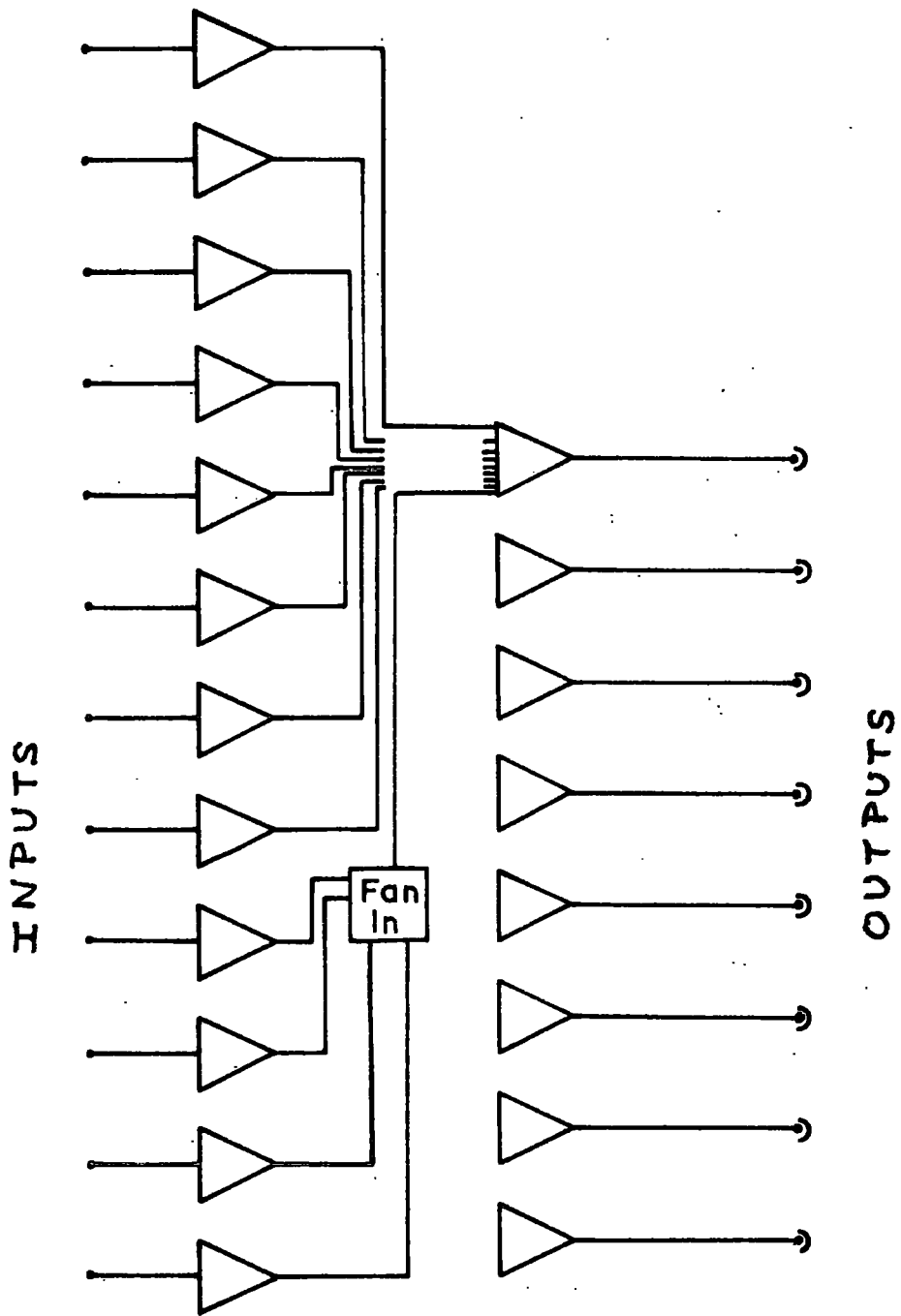
Figure A.4   The Measuring Tray Data Fan In.
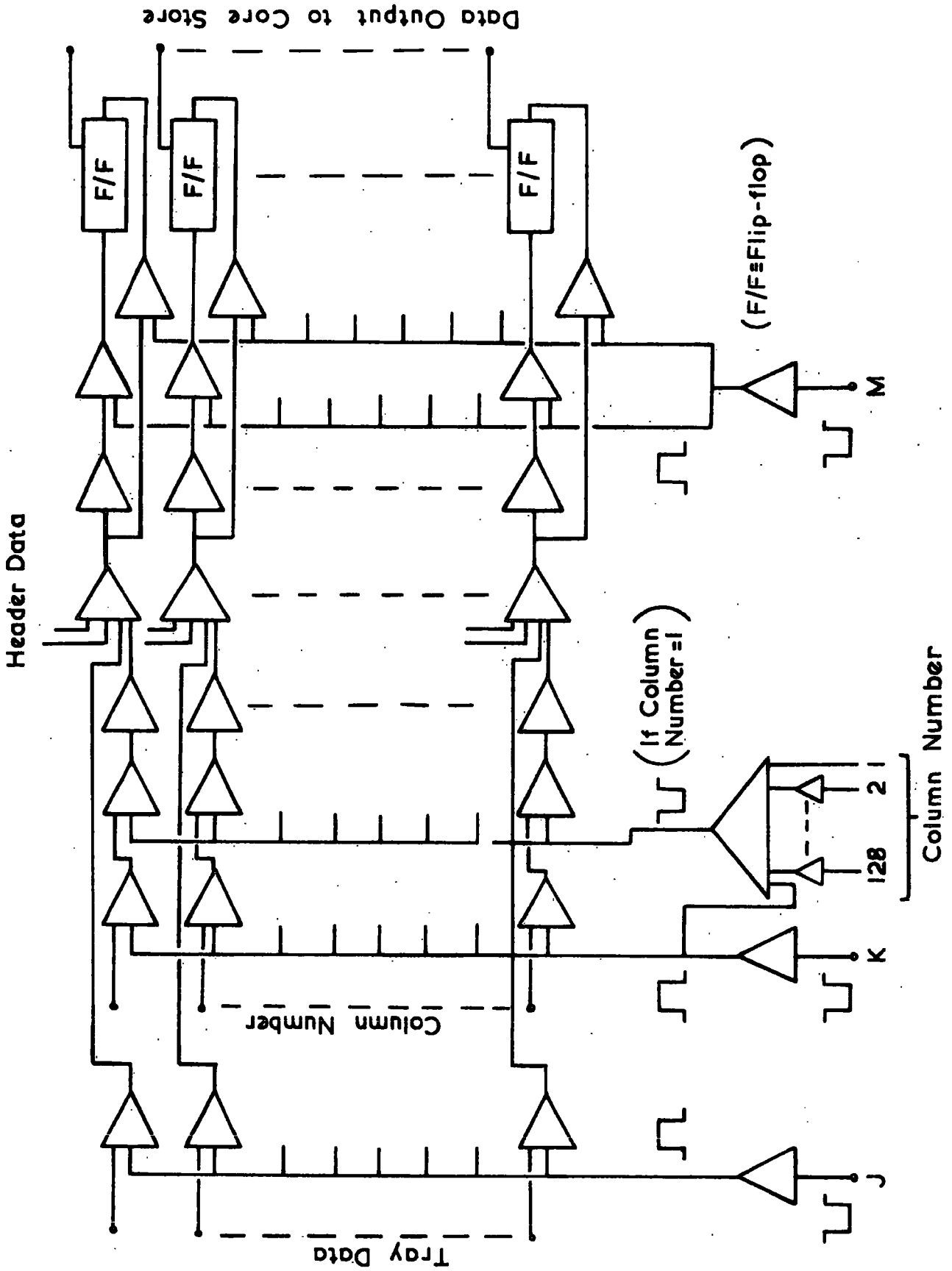
Figure A.5 The Final Data Fan In to the Core Store.

The tray identifiers (see Appendix B) are formed by this circuit. Column number 1 signifies the start of tray and the 'tube configuration' contains the tray number. When column 1 is detected, the data output lines are all gated to a logical 1 to form the tray identifier. The tray number is unaltered.

A.7 The Core Store Addresses

The addresses for the core store are either provided by the core store circuitry or by the computer. A diagram of the address scaler and address fan-in units of figure A.1 are shown in figure A.6. A 10-bit reversible synchronous binary scaler is used to generate the addresses used by the core store circuitry and a section of its circuit diagram is shown in figure A.7. The basic element of the scaler is the JK flip-flop. If both the J and K inputs are at a logical 1 then this flip-flop changes state every time a clock pulse is applied to it. The scaler counts one each time a clock pulse is applied and the direction of counting is determined by the logical state of the lines labelled 'forward' and 'backward'; these being the compliment of each other.

The scaler is reset at the beginning of each core load and the forward direction of counting is selected by the TCU. The TCU also routes the scaler addresses to the core store. After each core store cycle, the Wcc cycle complete pulse returned from the core store is used to increment the scaler by one. The Wcc' pulse is returned to the TCU to start the next cycle. The contents of the scaler are monitored and if they reach 1022 the core store is full. The Wcc' pulse is not returned to the TCU but instead the computer is interrupted by way of the pulse returned to the TCU by output 5A of this circuit.

When the core store has been loaded, the TCU routes the computer addresses to the core store and the backwards count direction is selected. The Wcc pulse received from the core store every read-write cycle decrements the scaler by one. The contents of the scaler are monitored by a 10 input gate and when the scaler counts down to zero the output of this gate goes to a logical 0. This logic level informs the TCU that the core store is empty and that data transmission is to be terminated.

Figure A.6 The Core Store Address Circuitry.
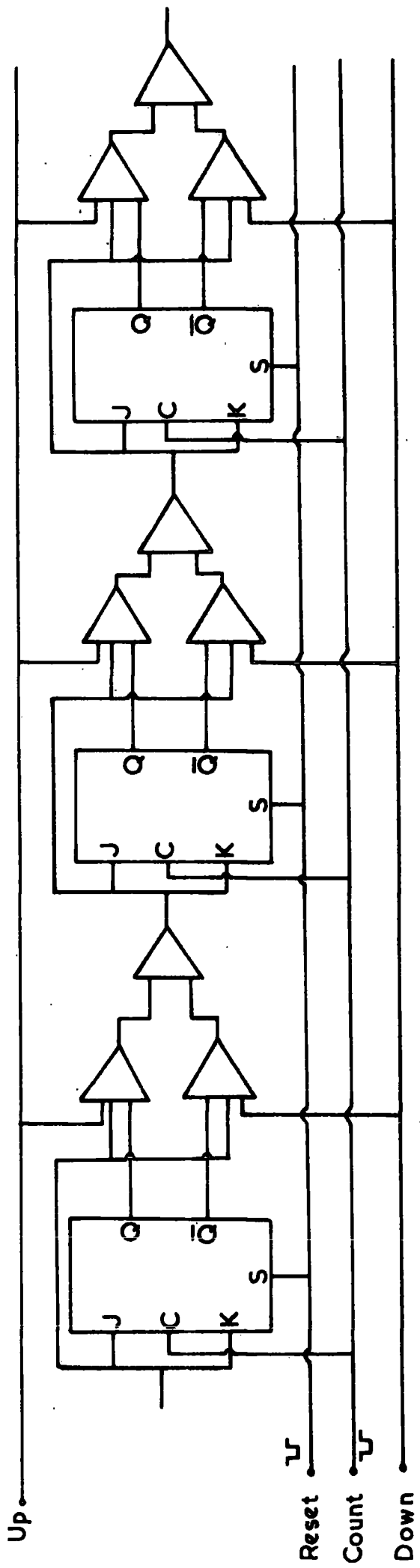
Figure A.7 A Section of the Reversible Synchronous Binary Scaler.

A.8   The Data Output to the Computer

There are nine data lines to the computer. Eight carry the data from the core store and one, the 9th bit, is used to inform the computer that the data transmission is to be terminated. The logic diagram of the data output unit to the computer is shown in figure A.8.

The 9th bit flip-flop is set to a logical 0 at the beginning of each event by the TCU and when the core store has been emptied, it is reset to a logical 1. It remains in this state until the next event. The transient nature of the data from the core store requires that these data be recorded in flip-flop memories for the computer to read. A few microseconds before a read-write cycle is started, these flip-flops are set such that the data lines to the computer are at a logical 1. Any zero data bits read out of the core store reset the corresponding flip-flops such that their data lines are at logical 0. Line drivers are used on the output of the flip-flops to enable a cable 25 yards long between the core store and the computer to be driven.

A.9   The Timing and Control Unit

The timing and control unit synchronizes the operations of the core store circuitry and determines the operation mode of the core store. A diagram of its logic circuitry is shown in figure A.9 and the numbers in the text refer to the numbered inputs and outputs shown on this diagram.

The circuitry is started by a 'High P_μ' pulse (6) and this immediately resets the entire circuitry ready for the loading of the core store. The 9th bit (see section A.8) is set to logical 0 by the HP'_μ pulse (7), the two flip-flops of circuit A.9 are set to the required conditions and the shift register of the header information (section A.4) and the address scaler (section A.7) are also reset (15). The forward counting mode of the address scaler is selected and these addresses are routed to the core store (5). The clear-write mode of the core store is also selected by the gating out of the pulses from Lc (17).
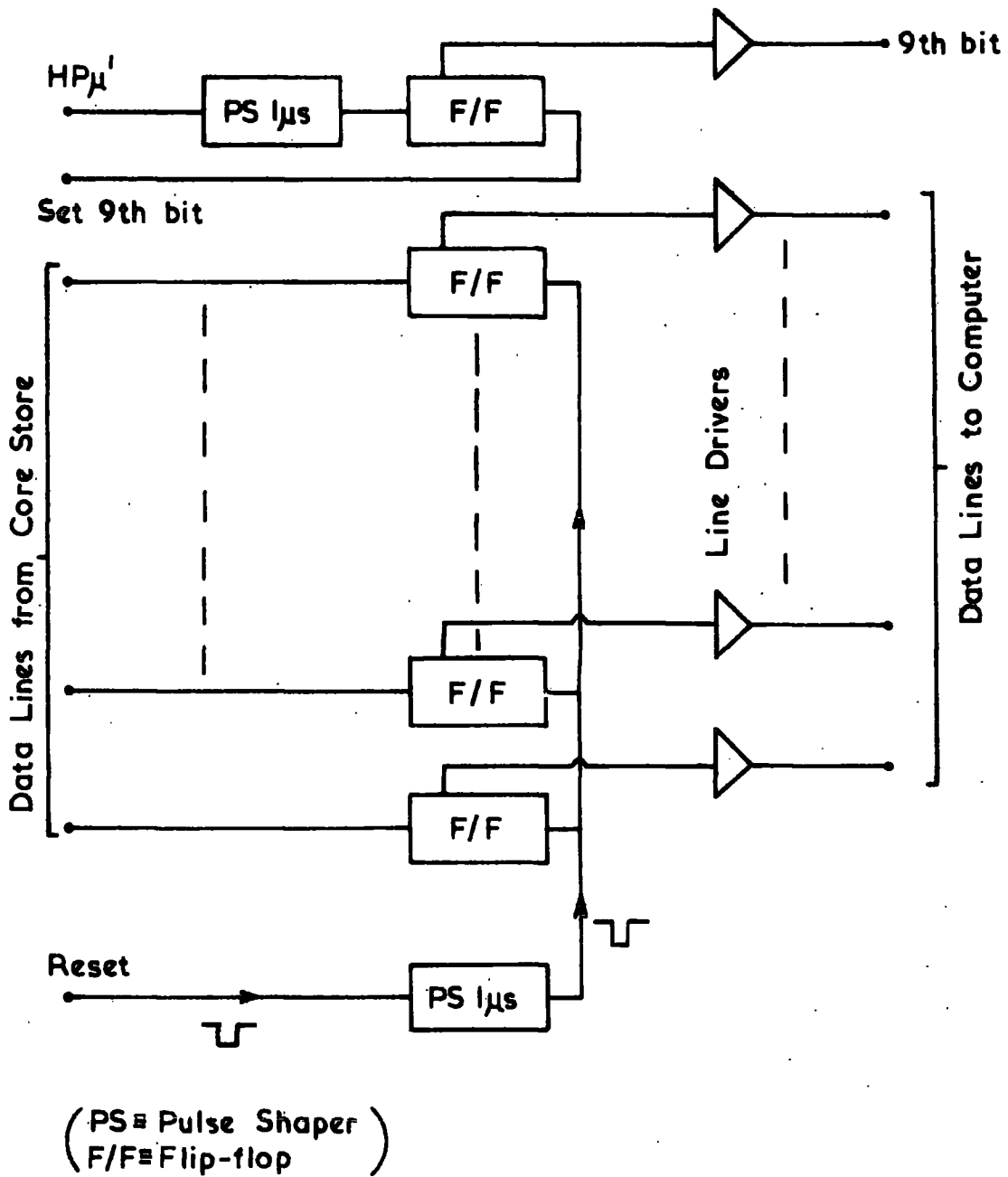
Figure A.8   The Data Output Circuitry

After a delay of $1\mu s$, the first shift pulse is applied to the shift register (4) and after a further 0.25 μs, the first word of the header information is strobed onto the core store data input lines (section A.6) by the gate pulse M (23). 2 μs later the start command, Pst (16), is given to the core store and a clear-write cycle proceeds.

Whilst the header information is being loaded into the core store, the Wcc' (18) pulse returned to this circuitry at the end of a core store cycle (see section A.7) produces another shift pulse and initiates another core store cycle by way of Route 1, as labelled on the diagram. This cycling continues until all of the header information has been loaded and line 8 goes to zero (see section A.4) effectively blocking Route 1. For every subsequent cycle, flip-flop 2 is caused to change state by the application of pulses to its clock input. The outputs of this flip-flop alternately gate the column number and the tube configuration into the core store. The state of the flip-flop after the end of the loading of the header causes the Wcc' (18) pulse to be routed to the 'Gate Out' (19, see section A.2). When a 'Gate-In' pulse is returned from the measuring trays, the column number is strobed onto the core store data lines by pulses on K and M (22,23). Another core store cycle is initiated, this time via Route 2, and the Wcc' pulse returned strobes the tube configuration into the core store with pulses on J and M (21, 23). These two cycles are then repeated until all the data has been loaded.

A store loaded pulse (9) from the measuring trays or a store full (10) from the address circuitry (see section A.7) sends an interrupt to the computer (12). Flip-flop 1 is reset and as a consequence, the backward counting direction of the address scaler is selected (5). The computer addresses are routed to the core store (5) and pulses on Lc (17) are permitted to accompany the Pst pulses (16) so that the core store operates in the read-write mode. The 'Address In' pulse (2) which accompanies the address from the computer is
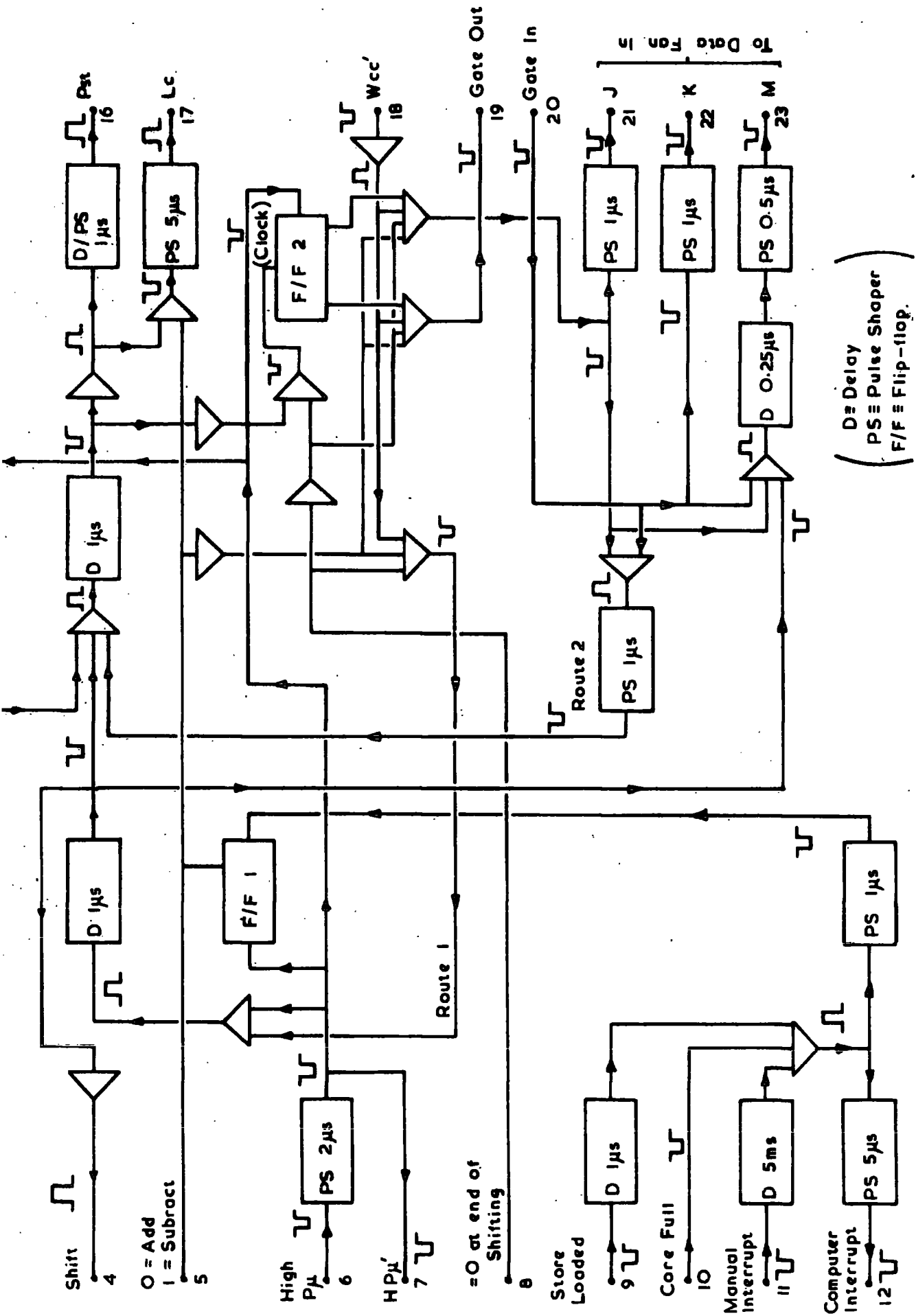
Figure A.9 The Timing and Control Circuitry.

immediately shaped by a 10μs pulse shaper to remove any reflections in the long cable from the computer. The data output flip-flops are reset by RDL (3, see section A.8). After a delay of 6μs, which allows time for the address lines to stabalise, Lc is applied to the core store (17) followed by Pst (16) 1μs later and the core store cycles in the read-write mode. The address scaler (see section A.7) is decremented by one at the end of the cycle. After the computer has received the data, the next address is sent and the cycle is repeated.

When the address scaler is decremented to zero (1), the next 'Address In' pulse is re-routed and the 9th bit is set (14) to tell the computer that data transfer is complete. The address scaler and shift register are reset and after 5 m s, a reset pulse is sent to the remainder of the MARS apparatus.

APPENDIX B

The Format of the Data from MARS

B.1 Introduction

This appendix describes the format of the data received by the computer from MARS. The data are composed of an event header followed by the data for each of the seven flash-tube trays in turn. Before these are described, a useful representation for binary data is outlined.

B.2 Hexadecimal Numbers

Each computer word is 16 binary bits (2 bytes) in length and a useful method by which the conditions of the individual binary bits can be described involves the use of hexadecimal or base 16 numbers. Each four binary bits are described by one hexadecimal character and hence one 16-bit word can be described by 4 such characters. Table B.1 contains the 16 hexadecimal characters and their binary and decimal equivalents. For an example of the use of hexadecimal numbers, consider the 16-bit binary configuration 0101 1001 1101 1000. The hexadecimal equivalent is 59D8 and the decimal equivalent is 23000.

Table B.1

Hexadecimal Numbers

Hexadecimal	Binary	Decimal
0	0000	0
1	0001	1
2	0010	2
3	0011	3
4	0100	4
5	0101	5
6	0110	6
7	0111	7
8	1000	8
9	1001	9
A	1010	10
B	1011	11
C	1100	12
D	1101	13
E	1110	14
F	1111	15

B.3 The Event Header

The event header is nine words long and it contains information relevant to each event. The majority of this information is in BCD format (Binary Coded Decimal). Each digit of a decimal number requires four binary bits and hence one 16-bit word can hold 4 BCD characters. The binary equivalents of these characters are given in Table B.1 (only digits 0 - 9 are used).

The first and last words of an event header are always zero and as described earlier, they are used to identify an event. The second and first half of the third word contain 6 BCD digits which together form the event number. The next 6 BCD digits contain the time of the event in hours, minutes and seconds, each quantity being represented by 2 BCD digits. The date and month are contained in the fifth word of the header. The date occupies 2 BCD digits but the month is an 8-bit binary number. The sixth word of a header contains the year (2 BCD digits) and the first two digits of the four digit magnet current. The first half of the seventh word of the header contains the remaining two digits of the magnet current and the second half contains binary information relating to the trigger-mode and the direction of the magnetic field. The trigger mode is reflected in the first three bits of the second half of word seven and the bits from left to right indicate that the side of the spectrograph which was triggered was the east, the west, and both east and west, respectively. The last four bits of the seventh word describe the magnetic field direction and refer to, from left to right, a positive field, a negative field, a zero field and a crossed field (i.e. the magnetic field in adjacent blocks is in opposite directions), respectively. The eighth word of the header contains a four digit number in BCD, which is twice the atmospheric pressure in millimetres of mercury. A summary of the contents of the header is given in Table B.2.

Table B.2

The Contents of the Event Header

Under the heading description, the number in parentheses is the number
of BCD digits allotted to the quantity.

	Description	Header word number
Event identifier	Blank	1
Event number	Decimal number (6)	2 and 3
Time	hr (2) mins (2) secs (2)	3 and 4
Date	day (2) month (2) year (2)	5 and 6
Magnet Current	Decimal number (4)	6 and 7
Trigger Mode	Binary (3 bits ≡ E,W, E and W)	7
Magnetic field Direction	Binary (4 bits ≡ +, -, 0, crossed)	7
Atmospheric Pressure	Decimal number (4)	8
Header termination	Blank	9

B.4 The Data from the Trays

The first word of data from each tray is the tray header. The first half of this word contains hexadecimal FF which identifies the word as a tray header, and the second half contains the tray number in binary. After this header follow the data from the columns of tubes. The left half of each word contains the column number (2 BCD digits) and the right half, the tube configuration for that column. The left most bit of this latter half corresponds to the bottom layer of tubes and the right most bit the top layer. If a bit is at a logical '1', then it indicates that the respective tube discharged. A typical tube pattern in a tray and the digital output from the tray for the pattern are shown in figure B.1. Only the columns which contain discharged tubes are transferred to the computer and hence the length of the data from each tray is variable. At the end of each tray come the dummy columns. These columns are numbers 91 - 96 and the left and right halves of these words are identical, the 'tube configurations' being wired into the electronics.

The trays follow the header in logical order and an example of an event is to be found in Table 4.1. The event depicted has an event number of 102749 and it occured at 23 : 15 : 27 on 15/05/70. The magnet current was 102 amps, the east side of the spectrograph was triggered, there was a negative magnetic field and the atmospheric pressure was 760mm. of Hg. Column 35 of tray 1 contains 4 discharged tubes, columns 29 and 30 of tray 2 contain 7, column 44 of tray 3 contains 5, columns 48 and 49 of tray 4 contain 4 and columns 49 and 50 of tray 5 contain 7 tubes. Both trays 6 and 7 contain bursts.
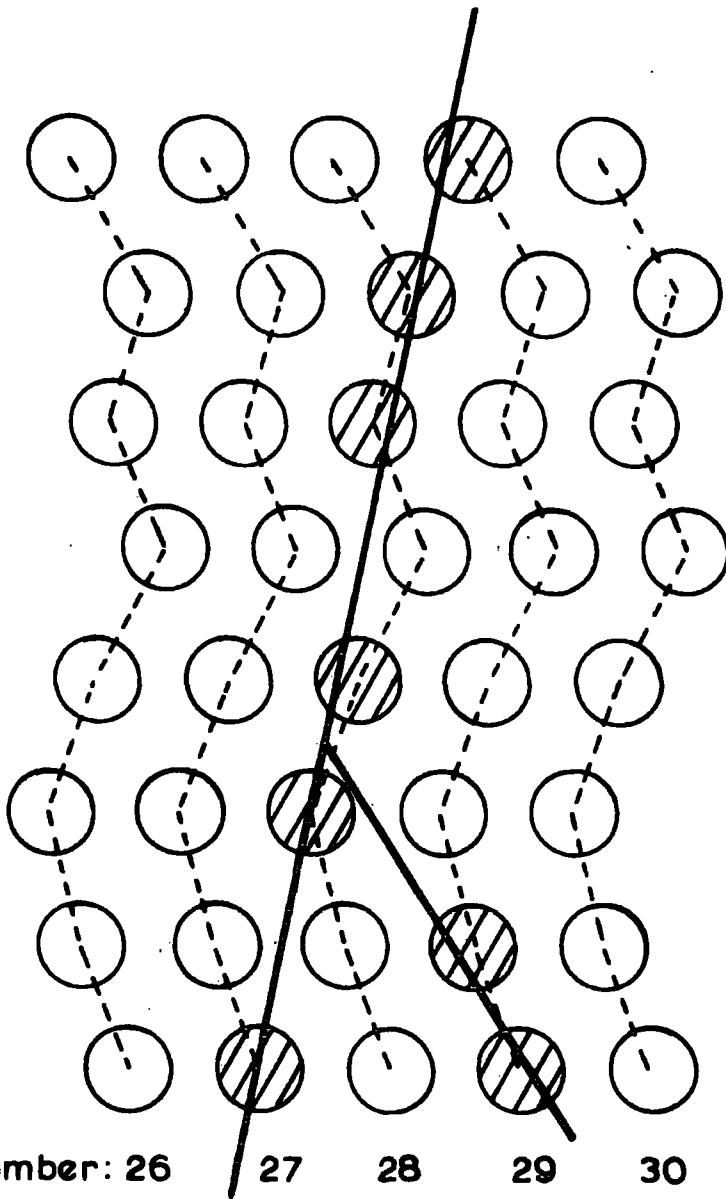
Column Number		Tube Configuration	Digital Output	
Decimal	Binary	Hexadecimal	Binary	Hexadecimal
27	00100111	80	1000 0000	2780
28	0010 1000	36	0011 0110	2836
29	0010 1001	C1	1100 0001	29C1

Figure B·1   The Digital Output from a Tray Associated with a
Tube Pattern.

APPENDIX C

The Parameters of the Track Fitting Technique

The flash-tube track fitting technique described in section 3.6 searches for tracks by drawing lines through the flash-tube configurations. It is important that these lines be sufficiently numerous and close enough together so that tracks do not fail a fitting option because of an inadequate line density.

The properties of the track fitting technique (section 3.6.2) were found by analysing a sample of data several times with different line densities. The region of the tray which was covered was the same as that shown in figure 3.3. Figure C.1 shows the proportion of tracks with option 0 fits as a function of the number of lines drawn through the configuration. Before a particular line density can be chosen, it is necessary to consider the execution time of the programme. This time is approximately proportional to the line density and hence the latter should be kept to a minimum. It can be seen from figure C.1 that the optimum line density is 36 and this is what is used by the programme.

The angle criterion described in section 3.6.4 also draws lines through the flash-tube configurations. It is essential that the spacing between these lines be smaller than the width of the narrowest channel in the measuring tray so that at least one line is placed in the channel. The distribution of the channel widths in the measuring trays has been found theoretically for tracks up to 7° and it is shown in figure C.2. It can be seen that there are no channels with widths less than 0.2mm and it is concluded that no loss of tracks will result as a consequence of the programme using a step size of ^{1}/80th of a tube spacing (0.1075mm).
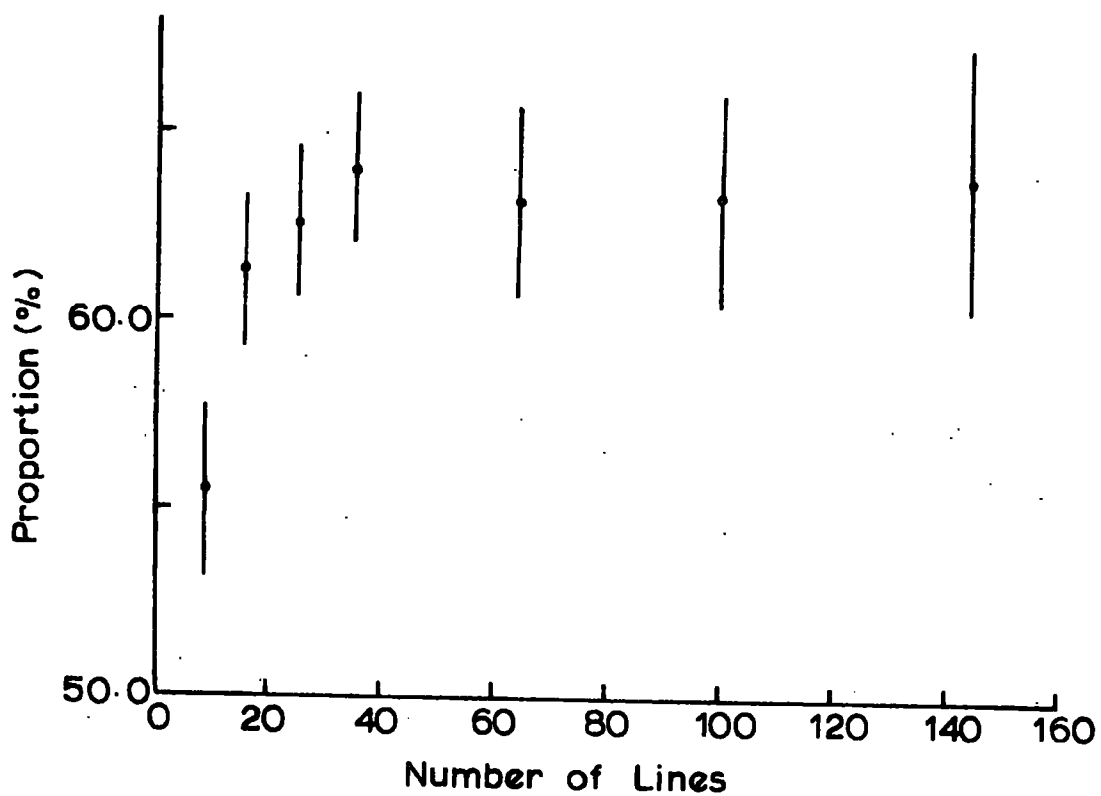
Figure C.1   The Proportion of Tracks with Option O Fits as a Function of the Line Density.
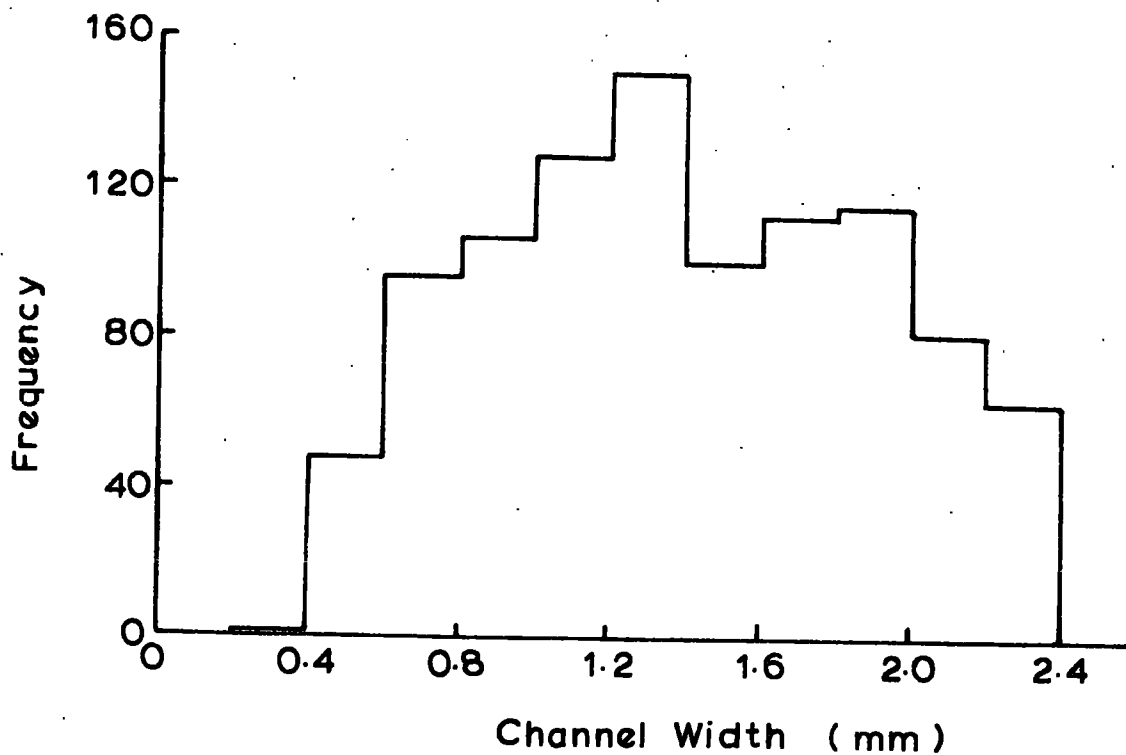
Figure C.2   The Channel Width Distribution of the Measuring Tray.

REFERENCES

(P.I.C.C.R. = Proc. Int. Conf. Cosmic Rays)

Adcock, C., 1970, Ph.D. Thesis, University of Durham.

Alexander, D., and Thompson, M.G., 1969, Acta Phys. Hung., 29, Supp. 4, 269.

Allkofer, O.C., Carstensen, K., Dau, W.D., Heinrich, E., Kraft, E., and Weinert, M., 1969, Acta Phys. Hung., 29, Supp 4, 13.

Allkofer, O.C., Carstensen, K., and Dau, W.D., 1971, P.I.C.C.R., Hobart, 4, 1314.

Allkofer, O.C., Carstensen, K., Dau, W.D., Fahnders, E., and Jokisch, H., 1971 a, P.I.C.C.R., Hobart, 4, 1319.

Allokfer, O.C., Carstensen, K., Dau, W.D., Jokisch, H., Frochlich, A., Seidman, A., and Yeiven, Y., 1971 b, P.I.C.C.R., Hobart, 4, 1596.

Ashton, F., 1961, Proc. Phys. Soc., Lond., 77, 587.

Ashton, F., Kisdnasamy, S., and Wolfendale, A.W., 1958, Nuovo Cim., 8, 615.

Ayre, C.A., and Thompson, M.G., 1969, Nucl. Inst. and Meth., 69, 106.

Ayre, C.A., and Thompson, M.G., 1970, Acta Phys. Hung., 29, Supp. 4, 541.

* Ayre, C.A., 1971, Private communication.

Backenstoss, G., Hyams, B.D., Knop, G., Marin, P.C., and Stierlin, U., 1963, Phys. Rev., 129, 2759.

Bellamy, E.H., Hofstadter, R., and Lakin, W.L., 1967, Phys. Rev., 164, 417.

Bergeson, A.E., Bolingbroke, G.L., Carlson, G., Groom, D.E., Keuffel, J.W., Morrison, J.L., and Osborne, J.L., 1971, P.I.C.C.R., Hobart, 4, 1418.

Bergeson, H.E., Keuffel, J.W., Larson, M.O., Martin, E.R., Masen, G.W., and Sternerson, R.D., 1968, Canad. J. Phys., 46, S399.

Bethe, H.A., 1932, Zeits. f. Physik, 76, 293.

Bethe, H.A., 1933, Handb. Phys., 24, 515.

Bhabha, H.J., 1938, Proc. Roy. Soc., A164, 257.

Bloch, F., 1933, Ann. Phys., Lpz., 16, 285.

Bowen, T., 1954, Phys. Rev., 96, 754.

Bulher, A., Massam, T., Muller, T.H., and Zichichi, A., 1964, CERN Rep., 64-31.

Bull, R.M., Coates, D.W., Nash, W.F., and Rastin, B.C., 1962, Supp. Nuovo Cim., 23, 39.

Carlson, G.W., Keuffel, J.W., and Morrison, J.L., 1971, P.I.C.C.R., Hobart, 4, 1412.

Caro, D.E., Parry, J.K., and Rathgeber, H., 1951, Aust. J. Sci. Res., A4, 16.

Christy, R.F., and Kusaka, S., 1941, Phys. Rev., 59, 414.

Conversi, M., and Gozzini, A., 1955, Nuovo Cim., 2, 189.

Cottrell, D.M., Piserchio, R.J., Thompson, R.L., and Lord, J.J., 1970, Proc. 6th Interamerican Sem. on Cosmic Rays, La Paz.

Crispin, A., and Fowler, G.N., 1970, Rev. Mod. Phys., 42, 290.

Filosofo, I., Pohl. E., and Pohl-Ruling, J., 1954, Nuovo Cim., 12, 809.

George, E.P., and Evans, J., 1950, Proc. Phys. Soc. A, 63, 1248.

Griesen, K., 1965, P.I.C.C.R., London, 2, 609.

Griesen, K., 1966, Phys. Rev. Letts., 16, 748.

Grupen C., Hamdam, M.A., Hansen, J.S., Thompson, M.G., Wolfendale, A.W., Young, E.C.M., (in the press).

Hayman, P.J., Palmer, N.S., and Wolfendale, A.W., 1963, Proc. Roy. Soc. A, 275, 391.

Hayman, P.J., and Wolfendale, A.W., 1962, Proc. Phys. Soc., 80, 710.

Heitler, W., 1948, Quantum Theory of Radiation. (Oxford Univ. Press).

Holmes, J.E.R., Owen, B.G., and Rogers, A.L., 1961, Proc. Phys. Soc. A, 78, 505.

Katz, L., and Penfold, A.S., 1952, Rev. Mod. Phys., 24, 28.

Krishnaswamy, M.R., Menon, M.G.K., Narasimham, V.S., Kawakami, S., Miyake, S., and Mizohata, A., 1969, Acta. Phys. Hung., 29, Supp. 4, 221.

Linsley, J., 1962, Phys. Rev. Letts., 9, 126.

Mando, M., and Ronchi, L., 1952, Nuovo Cim., 9, 517.

Marshak, R.E., 1952, Meson Physics (New York: Dover Publ. 1958).

Menon, K.G., and Ramana Murphy, P.V., 1967, Prog. in Elem. Part. and Cosmic Ray Phys., IX, 161.

Messel, H., and Crawford, D.F., 1970, Electron-Photon Shower Distribution Function, (Pergamon Press).

Millar, C.H., Hincks, E.P., and Hanna, G.C., 1958, Can. J. Phys., 36, 54.

Nandi, B.C., and Sinha, M.S., 1972, Nucl. Phys., B40, 289.

Osborne, J.L., Palmer, N.S., and Wolfendale, A.W., 1964, Proc. Phys. Soc., 84, 901.

Owen, B.G., and Wilson, J.G., 1951, Proc. Phys. Soc., 64, 417.

Pine, J., Davisson, R.J., and Greisen, K., 1959, Nuovo Cim., 14, 1181.

Rogers, I.W., 1965, Ph.D. Thesis, University of Durham.

Roll, P.G., and Wilkinson, D.T., 1967, Ann. Phys. (USA), 44, 289.

Rossi, B., 1948, Rev. Mod. Phys., 20, 537.

Rossi, B., 1961, High Energy Particles (Prentice-Hall, Inc.), 14.

Rossi, B., and Greisen, K., 1941, Rev. Mod. Phys. 13, 240.

Said, S.S., 1966, Ph.D. Thesis, University of Durham.

Sternheimer, R.M., 1956, Phys. Rev., 103, 511.

Sternheimer, R.M., and Peierls, R.F., 1971, Phys. Rev. B, 3, 3681.

Thompson, M.G., and Wells, S.C., 1972, Nuc. Inst. and Meth., 102, 35.

Wolfendale, A.W., 1971, Private communication.

Wolfendale, A.W., 1972, Proc. E.P.S. Meeting, Paris (in the press).

* Ayre, C.A., Hamdan, M.A., Hume, C.J., Thompson, M.G., Wells, S.C., Whalley, M.R., and Wolfendale, A.W., 1971a, P.I.C.C.R., Hobart, 4, 1364.

* Ayre, C.A., Hamdan, M.A., Hume, C.J., Thompson, M.G., Wells, S.C., Whalley, M.R., and Wolfendale, A.W., 1971b, P.I.C.C.R., Hobart, 4, 1458.

ACKNOWLEDGMENTS